MASTER

Emittance measurements of electron beams produced by the 100 kV Smart*Light photo electrongun

van Zwol, A.

Award date:
2021

Emittance measurements of electron beams produced by the 100 kV Smart*Light photo electrongun

Annemarie van Zwol - 0889893
June 16, 2021

A thesis for the degree of Master of Science (MSc.)

Master of Applied Physics:
Eindhoven University of Technology
Department of Applied Physics
Coherence and Quantum Technology (CQT)
Report number: CQT 2020-28

dr. ir. P.H.A. Mutsaers
dr. ir. X.F.D. Stragier

Abstract

The aim of the Smart*Light project is to develop a high quality x-ray source based on inverse Compton scattering. The quality of the produced x-ray beam depends on the quality of the electron beam and the quality of the laser beam at the interaction point. For this setup a 100 kV DC photo electron gun will be used. Before the gun is installed in the complete setup, the beam quality of electron beam produced by the gun is measured in a test setup. Waist-scans are used to determine the emittance before the linear accelerator structure. Measurements are performed for two types of UV beam profiles on the cathode, Gaussian and flat-top, and bunch charges ranging from 0.7 pC ± 15% to 47 pC ± 15%. The effects of these parameters on the validity of the waist-scan technique and the beam quality are studied. It was found that space-charge forces compromise the validity of the waist-scan technique. The aim is to operate the Smart*Light beamline with bunches of 10 pC. Although space-charge forces were already found to compromise the use of the waist-scan technique for 10 pC bunches, a rough estimate was still obtained. For 12 pC ± 15% bunches created with a Gaussian UV beam profile on the cathode and a gun solenoid current of 10.44 A an emittance 644 ± 31 nm·rad is measured.

An alternative method for emittance measurements is the use of a pepper-pot. The pepper-pot method is less sensitive to space charge effects, and allows information of the beam quality to be related to the spatial beam distribution. Due to time related issues, no actual measurements are performed. However, based on simulations of the beam in the Smart*Light setup and the spatial restrictions two potential measurement setups are proposed. For both options, the available drift length proves to be the limiting factor. A larger drift length would benefit the quality of the measurements in both setups. Furthermore it has to be kept in mind that the pepper-pot plates are designed for 10 pC bunches. An increase in bunch charge could require smaller holes and larger hole spacing.

Contents

Chapter 1

Introduction

In this chapter the topic and goal of this thesis are introduced. To get an understanding of the relevance of the Smart*Light project and the importance of technological advances for the feasibility of the project the basics of x-rays, current available x-ray sources and applications of x-rays are explained. Furthermore some important advances in electron beam physics are mentioned. The concept behind the Smart*Light project is explained, and at last the scope of this thesis is discussed.

1.1 X-rays

In 1985 Wilhelm Conrad Röntgen by accident discovered x-rays when he saw a nearby screen lighting up while investigating cathode rays [1]. It was quickly discovered that this new type of radiation could penetrate through low density materials like soft body tissue, but are absorbed by materials with higher density like bones or lead. The discovery was soon labeled to be of major significance for the medical world, since it allowed doctors to see inside a patients body.

The properties of electromagnetic waves vary over the entire range of wavelengths. The spectrum is divided in different bands or classes. In figure 1.1 the electromagnetic spectrum and its classes are displayed. The spectrum bands each contain a range of wavelengths with similar properties. X-rays are categorized as radiation with wavelengths between 12 nm and 1 pm which is equivalent to energies between 100 eV and 100 keV. Because of its high energy, x-rays can penetrate matter and potentially ionize atoms or disrupt molecular bonds. The x-ray category itself is divided into two subcategories: soft x-rays in the energy range of 100 eV and 10 keV and hard x-rays with higher energy [2].

After the initial discovery that x-rays can be used to visualize or photograph the bone structure within a body, more advanced imaging techniques have been developed. The use of x-rays is not only limited to medical diagnostics. X-rays are also used for for example security scans of items, art history research and material science.

1.2 X-ray sources

1.2.1 X-ray tube

The most common x-ray source that is used to generate x-rays is the x-ray tube. Different variations exist, but the main idea still descends from the Crooke tube with which x-rays were first discovered. In figure 1.2a a schematic drawing of a hot cathode tube, also called Coolidge tube, is displayed. The hot cathode tube is the most common x-ray tube. The cathode filament is heated by running an electric current. When the electrons inside the cathode

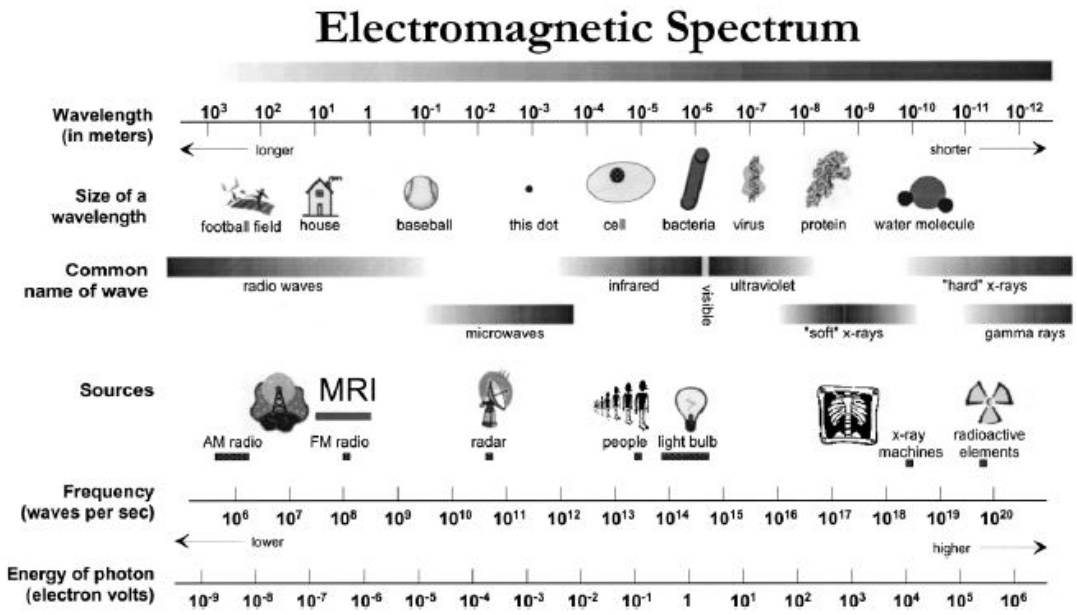

Figure 1.1: An overview of the electromagnetic spectrum [3].

have gained enough thermal energy to overcome the cathode work function, they are emitted from the cathode. Due to the electric field between cathode and anode, the free electrons are accelerated towards the anode. When the electrons hit the anode, they decelerate and Bremsstrahlung is emitted. The emitted Bremsstrahlung forms a broad continuous spectrum of relatively low intensity of photons per wavelength. As can be seen in figure 1.2b, the spectrum of produced x-rays not only consists of continuous Bremsstrahlung but also shows sharp characteristic peaks. The characteristic radiation profile is solely dependent on the type of anode material. The peaks are the result of so called K-radiation. When an electron is excited out of the inner electron shell it leaves a vacancy. An electron from a higher shell will decay to fill this vacancy and the energy difference between its original shell and its new shell can be emitted as a photon. The intensity of photons emitted as a function of photon energy for the characteristic peaks is much higher than this intensity for the continuous Bremsstrahlung spectrum. Therefore the characteristic K-radiation is the main form of output x-rays and this type of x-rays is used in most applications.

Over the years, variations on the hot cathode tube are developed. Examples are rotating anode x-ray tubes where the rotation reduces the power load on the anode, and liquid-metal anode x-ray tubes where the anode is already melted and allows for a higher electron beam power density [4].

1.2.2 Synchrotron

For some applications very high quality x-rays or x-rays with a specific energy that does not match the characteristic peaks of available anode materials are required. The alternative source of x-rays one can consider in these cases is synchrotron radiation. In basis a synchrotron is a circular accelerator in which charged particles circulate at relativistic speed. At the bends the charged particles experience acceleration, and because of this acceleration they emit radiation. Although all charged particles emit radiation upon acceleration, electrons emit most power due to the mass dependency. In synchrotron facilities build with the purpose of producing x-ray beams, the particles that are circulating are electrons. The design of the synchrotron itself can also be adjusted to produce x-ray beams more efficiently. The ring can be build from straight sections and bend sections to increase acceleration in the bends, and undulators and wigglers can be installed. This enables the production of x-rays of different energies. Each synchrotron facility can have multiple beam lines. However, there are only limited facilities across the world and beam time remains sparse and expensive.

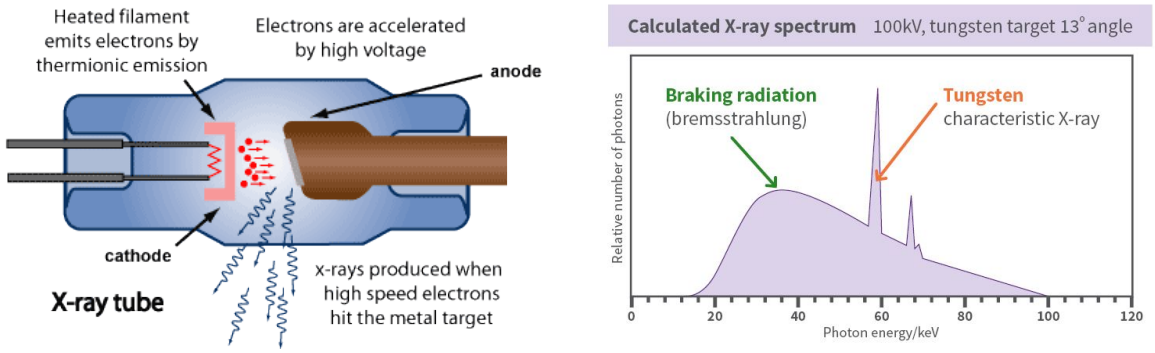

(a) (b)

Figure 1.2: a) Schematic drawing of a hot cathode x-ray tube [5], b) Example of an x-ray spectrum produced by a hot cathode x-ray tube with a Tungsten cathode. The Bremsstrahlung profile and characteristic peaks are indicated [5].

(a) (b)

Figure 1.3: a) Image of the synchrotron facility at Grenoble [6], b) schematic drawing of the production of synchrotron radiation [7].

1.3 X-ray diagnostics

The most common known application for x-rays is 2 dimensional projectional imaging. Samples are exposed to (hard) x-rays, and depending on the material properties and for example thickness x-rays are absorbed. The x-rays that are not absorbed by the sample reach the detector. On the detector, the shadows of the absorbing structures are visualized. This technique is for example used for medical imaging of bone structures, but also for security luggage scans at the airport. Over time, more advanced imaging techniques have been developed. Some of these techniques, like phase-contrast imaging and K-edge subtraction imaging, require x-rays with specific properties that can not always be produced by the conventional x-ray tubes.

Phase-contrast imaging is a technique that can be used to obtain a more detailed map of the "photographed" sample. Instead of only using the difference in absorbance of the x-rays by different materials, also the phase information of the detected x-rays is taken into account [8]. Differences of the refractive index between a detailed part of the sample and its surroundings cause a phase shift of the x-rays propagating through the detail with respect to the

x-rays propagating through the surrounding parts. The phase difference results in interference patterns that can be used to resolve the details not visible from the projected absorption shadows. Key to this imaging technique is the coherence of the electron beam. A high coherence is required in order to be able to observe the phase shifts. X-rays produced with x-ray tubes are typically not very coherent, therefore mainly synchrotron radiation is used for this type of imaging.

A second imaging technique that requires a very specific type of x-rays is K-edge subtraction imaging. This technique can be used to visualize specific (soft) structures that can not be studied clearly from conventional projectional imaging. For K-edge subtraction imaging, a contrast medium is used. The contrast medium shows a sharp increase in the absorption coefficient just above the K-edge energy level. After administering the contrast medium, two x-ray images are made. One of these images is made with an x-ray energy just below the K-edge level, the absorption by the contrast fluid in this image is low. The second image is made with an x-ray energy just above the K-edge level. Absorption of the x-rays by the contrast medium for this image is high. Subtraction of the first image from the second image leaves only the distribution of the contrast medium and therefore allows study of the region of interest [9, 10, 11]. K-edge subtraction imaging can not only improve the image quality compared to computed tomography scans (CT), but also substantially lowers the dose of radiation that is required. K-edge subtraction requires a very monochromatic beam with high brilliance. Furthermore x-ray beams with two different energies are needed, so a source where the x-ray energy is tunable would be a great advantage. Currently, synchrotron radiation can be used for this type of imaging [12].

1.4 Electron beam physics

Since the birth of electron optics in 1926 [13], the field of electron beam physics has quickly developed. The developments resulted in many applications like electron microscopes, electron lithography and high energy particle accelerators, but also more day to day items for example cathode ray tube televisions. Recent technological advances allow for the development of compact and powerful linear accelerators and high bunch charge high beam quality electron guns. Both of these developments are key to the feasibility of the Smart*Light project in the CQT group at TU/e.

1.4.1 Electron gun

The first electron emitters relied on thermionic electron emission from a hot cathode and acceleration by a static electric field. Over time, different type of electron guns are developed. Electron guns can be classified by the type of electric field generation and by the electron emission mechanism. The electric field in the gun can be static (DC) or alternating (RF). RF electron guns can generally accelerate electrons to high energies over short distances (order of MeV over few cm). Therefore RF electron guns are able to produce high bunch charges (order of nC). However, most RF electron guns can not operate with a high repetition rate. The electric fields in a DC gun are generally lower than in a RF gun. Due to the smaller acceleration, bunches suffer more from space charge effects. However, there are also advantages to the DC gun. It can be operated with a high repetition rate, and it allows for the use of cathode materials with low thermal emittance [14].

A 100 kV DC photo electron gun was developed at the TUe. The gun is described extensively in [15, 16]. This photo electron gun is able to produce femtosecond bunches with high bunch charges up to 50 pC. The electric field in the gun is static, and electrons are emitted from the cathode by photo emission.

1.4.2 Linear accelerator

Over the years, accelerators have become more powerful and more efficient. At CERN (*Conseil Européen pour la Recherche Nucléaire*) a new compact linear accelerator (CLIC) is being developed. The accelerator developed for CLIC will be able to produce an accelerating field of 100 MV/m [17].

1.5 Smart*Light

The two main x-ray sources as described in section 1.2 both have their limitations and difficulties. It would be useful to have a source that can fill the gap of need between x-ray tubes and synchrotrons. This is where the Smart*Light project aims for. The goal is to create a high quality x-ray source which can produce x-rays of better quality than available x-ray tubes and for which the energy of the produced x-rays is tunable. The source is designed to be of table-top size, and the costs should be considerably less than the costs of a synchrotron. Because of the smaller size and the lower costs, it should enable access to high-quality x-rays for all kind of projects.

1.5.1 Inverse Compton scattering

X-ray generation in the proposed Smart*Light source is based on inverse Compton scattering. In normal Compton scattering energy is transferred between a charged particle and a photon during a (partly) inelastic scattering event. This results in a change of wavelength of the scattered photon [18]. The Compton effect usually describes a scattering event where the photon loses energy to the electron. However the energy transfer can also work the other way around, from electron to photon. This phenomena is called inverse Compton scattering. Smart*Light proposes to scatter a laser beam with an original wavelength of 400 nm or 800 nm on a highly relativistic electron beam. In figure 1.4 the photon-electron interaction is illustrated in a schematic drawing. For a head on collision between electron and incoming photon the wavelength of the scattered photons is dependent on the Lorentz factor $\gamma = \frac{1}{\sqrt{1-\frac{v^2}{c^2}}}$ of the electron beam (where v is the velocity of the electron and c is the speed of light), the original wavelength of the photons λ_0 and the angle θ of the scattered photon with respect to the central axis. For a small angle approximation where $sin(\theta) \approx \theta$, the wavelength of the scattered photons is given by

$$\lambda_x = \frac{\lambda_0}{4\gamma^2}(1 + \gamma^2\theta^2) \tag{1.1}$$

The produced wavelength is quadratically dependent on the energy of the electron beam. This dependence offers an opportunity for inverse Compton scattering based x-ray sources. If the setup can be build in such a way that the electron beam energy is tunable, the output wavelength of the source can also be tuned.

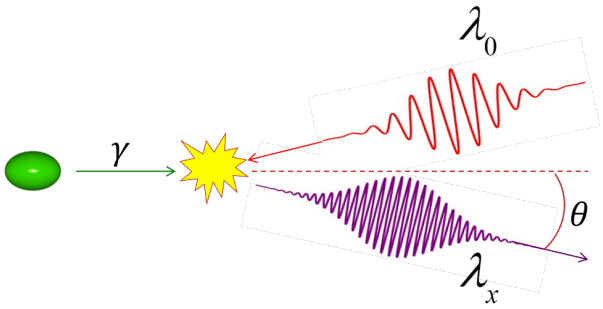

Figure 1.4: Schematic drawing of the inverse Compton scattering process [19].

1.5.2 X-ray beam quality

The quality of an x-ray beam depends on a number of factors. The quality term brilliance accounts for the intensity, angular spread, size of the beam and bandwidth. The higher the brilliance, the better the quality of the x-ray beam. For the Smart*Light source, the brilliance is given by

$$B_x = N_e N_0 \frac{12}{\pi} \frac{\gamma^2 \sigma_T}{(2\pi)^3 \varepsilon_n^2 (\sigma_0^2 + \sigma_e^2)} = N_x \frac{12}{\pi} \frac{\gamma^2}{(2\pi)^2 \varepsilon_n^2} \tag{1.2}$$

where N_e is the number of electrons, N_0 is the number of photons, γ is the Lorentz factor of the electron beam, σ_T is the Thomson cross section, σ_e is the cross section of the electron beam at the interaction point, σ_0 is the cross section of the laser beam at the interaction point and ε_n is the normalized root mean square emittance of the electron beam. The quality of the produced x-ray beam depends on both the laser beam properties and the electron beam properties. To maximize the scattering probability and therefore the number of produced x-ray photons N_x, both the number of photons in the laser beam and the number of electrons in the electron beam have to be high and the laser beam size and electron beam size at the interaction point have to be low.

1.5.3 Feasibility

To give an idea of the feasibility of the Smart*Light setup, the estimates of some of the key properties of the electron beam and laser beam at the interaction point are summarized in table 1.1. From these parameters it can be calculated that the expected number of x-ray photons is approximately $2.7{\cdot}10^5$ per bunch. The wavelength of the output x-rays is tunable by slightly changing the energy of the electron beam. In principle, the x-band accelerator should be able to accelerate the electrons to a gamma factor of 60. From equation 1.2 it can be seen that that the quality of the produced x-ray beam depends on the emittance of the electron beam. It is estimated that an emittance of 500 nm·rad should be achievable for 10 pC bunches produced with the 100 kV DC photogun of which the properties are discussed in section 5.2.

Table 1.1: Estimates of the properties of the electron beam and the laser system at the interaction point

	input
electron beam	
bunch charge	10 pC
spot size σ at interaction point	5 μm
laser system interaction point	
laser pulse energy	10 mJ
spot size σ at interaction point	5 μm
wavelength	400 or 800 nm

1.5.4 Proposed setup

The main setup of the Smart*Light project is designed to be of table top size. In figure 1.5 an artist impression of the setup is displayed. From left to right the electron gun, the buncher cavity, a cross which enables the use of some diagnostical tools, the linear accelerator, the focusing solenoids and the interaction chamber are drawn on top of an optical table. Although the actual beamline does fit on an optical table, there are other additional components that are not drawn into this image but are necessary for the setup to work. Examples are the laser used to excite electrons from the cathode, the laser that provides the laser beam for the interaction point, a klystron that can generate the power required to operate the accelerator, a pulse compressor and RF network that can manipulate and transport the power generated in the klystron. Apart from these major systems there is need for supporting items like a beam dump, a vacuum system, power supplies and many more. Furthermore part of the setup most be shielded because of the generated x-rays, γ-rays and neutrinos.

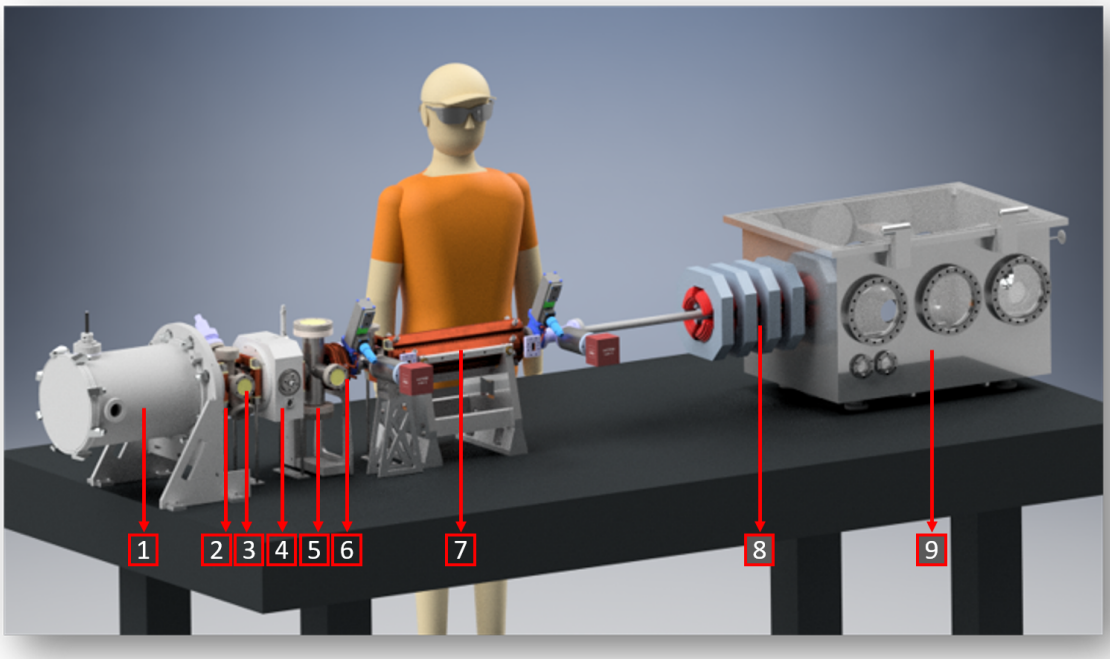

Figure 1.5: Artist impression of the Smart*Light beamline [20]. 1) electron gun, 2) gun solenoid, 3) UV in-coupling, 4) velocity buncher cavity, 5) diagnostic cross, 6) solenoid, 7) RF accelerator, 8) focusing quadrupole quadruplet, 9) interaction chamber.

1.6 Scope of this thesis

As already mentioned, the quality of the produced x-ray beam depends on the quality of the laser beam and on the quality of the electron beam at the interaction point. This thesis is focused on the quality of the electron beam in the low energy part of the setup before the accelerator. The goal is to determine the beam quality for beams with different bunch charges and initial beam profiles. A setup for a beam quality measurement with the pepper-pot method is designed and a set of beam quality measurements is performed with the waist-scan method. Because the waist-scan technique is used for a broad range of bunch charges, the measurements are used to study the validity of the waist-scan technique for space-charge dominated bunches. Before the design and measurement results are presented some theoretical basics of electron beam physics are explained in chapter 2. In chapter 2 the quality term for an electron beam, the emittance, is also introduced and potential sources of emittance are discussed. Furthermore magnetic fields created by solenoids and the focusing effect of solenoid magnetic lenses for charged particle beams are discussed. In chapter 3 two measurement techniques that can be used to measure the beam emittance are introduced: the waist-scan method and the pepper-pot method. After the introduction of both methods the pros and cons are discussed and compared. In chapter 4 a simulation of an electron beam in the Smart*Light setup is used to design two potential pepper-pot setups for the final Smart*Light beamline. In chapter 5 the different elements of the experimental setup that is used to perform waist-scan measurements are discussed. In chapter 6 the waist-scan procedure itself is explained and the results obtained for waist-scans performed for bunches created with two different UV beam profiles on the cathode and a range of different bunch charges are discussed. Finally in chapter 7 the conclusions of this thesis are presented.

Chapter 2

Theory

To be able to discuss the quality of high-quality electron beams (or other charged particle beams), it is important to have a general figure of merit which can be used to quantify the quality of the beams. The figure of merit which is generally used to describe beam quality is emittance. To grasp the meaning of the term emittance it is important to have some understanding of basic beam dynamics. In this chapter, first the phase space representation of a beam and the use of beam ellipses are introduced. Then the term emittance is explained. After this, the initial emittance for photo electron guns is introduced and last potential sources of emittance growth are discussed.

2.1 Electron beam

A particle is defined by its spatial position and its momentum. Every particle has 6 coordinates (x,y,z,p_x,p_y,p_z) which together form the so called phase space. It is customary to define the z-axis along the line of beam propagation, and the x- and y-axis perpendicular to the line of beam propagation. If for a set of particles the longitudinal momenta of all particles are comparable and much larger than their transverse momenta, the set of particles forms a beam.

2.1.1 Transverse trace space

Since the longitudinal momentum is much larger than the transverse momenta, it is possible to calculate the slope of each particle with respect to the longitudinal axis. The respective slopes are given by $x' = \frac{dx}{dz}$ and $y' = \frac{dy}{dz}$. These slopes can be used to describe the position of a particle in decoupled transverse trace space (x, x') and (y, y').

2.1.2 Beam ellipse

Projection of a beam with normal distribution of position and momentum coordinates to transverse trace space results in an ellipsoidal particle distribution. The equidensity contours of the beam also form ellipses. In figure 2.1 an image of a beam ellipse is shown. The general equation for such an ellipse is

$$\widehat{\gamma}x^2 + 2\widehat{\alpha}xx' + \widehat{\beta}x'^2 = \varepsilon \tag{2.1}$$

Where x and x' are the trace space coordinates, $\widehat{\alpha}$, $\widehat{\beta}$ and $\widehat{\gamma}$ are the Twiss or Courant-Schneider parameters and ε is related to the area of the ellipse with $A = \pi\varepsilon$ [21]. Note that $\widehat{\beta}$ and $\widehat{\gamma}$ are not the related to the relativistic beta factor $\beta = \frac{v}{c}$ where v is the beam velocity in longitudinal direction and c is the speed of light and the Lorentz factor $\gamma = \frac{1}{\sqrt{1-\beta^2}}$. The beam can be described by a beam matrix that contains the Twiss parameters

$$\sigma_{beam} = \varepsilon \begin{pmatrix} \widehat{\beta} & -\widehat{\alpha} \\ -\widehat{\alpha} & \widehat{\gamma} \end{pmatrix} \tag{2.2}$$

With $x = \begin{pmatrix} x \\ x' \end{pmatrix}$ the beam ellipse can be described as

$$x^T \sigma_{beam}^{-1} x = 1 \tag{2.3}$$

Since the ellipse area is $\pi\varepsilon$, calculation of the determinant of the beam ellipse results in the following relation between the Twiss parameters

$$\widehat{\beta}\widehat{\gamma} - \widehat{\alpha}^2 = 1 \tag{2.4}$$

In general it is very useful to describe the beam in matrix form since beam ellipse transformation can be used to transport the beam through a linear optical system. The Twiss parameters are related to the beam properties. In a beam waist, there is no correlation between the spatial coordinates and the momentum coordinates. Therefore the Twiss parameter $\widehat{\alpha} = 0$ in the waist. From equation 2.2 and relation 2.4 in the waist, the Twiss parameters are related to the spot size and each other as $\sigma_x = \sqrt{\varepsilon\widehat{\beta}} = \sqrt{\frac{\varepsilon}{\widehat{\gamma}}}$ and to the spot divergence $\sigma_{x'} = \sqrt{\varepsilon\widehat{\gamma}} = \sqrt{\frac{\varepsilon}{\widehat{\beta}}}$ [21].

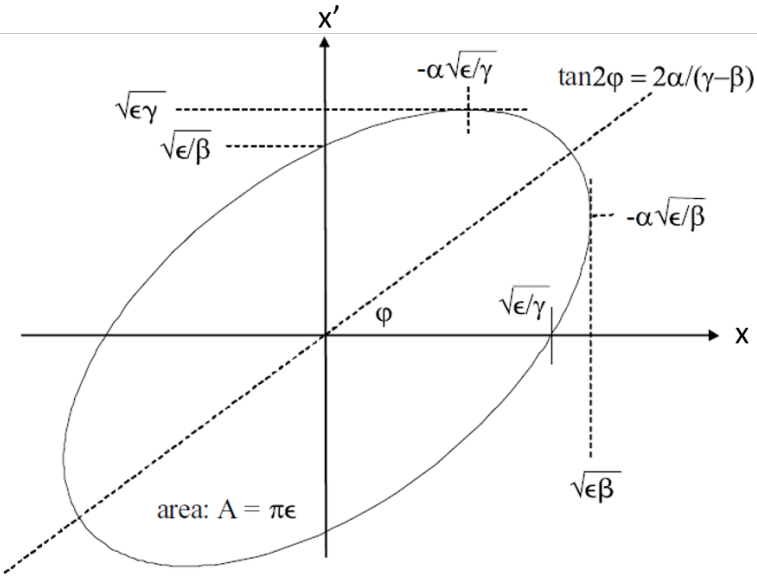

Figure 2.1: Trace space ellipse with indicated ellipse parameters [21]

If it is assumed that only conservative forces work in the system the continuity equations and conservation laws must hold. This means that no friction like forces or interaction between individual particles are allowed to take place and $\frac{\partial F_x}{\partial p_x}$ should be zero for all forces. Liouville's theorem states that in such a conservative system the phase-space particle density does not change over time and therefore the phase space area occupied by the beam is a constant [13, 21, 22]. This implies that the area of a beam ellipse in a conservative system is a constant.

2.2 Emittance

In the previous section it is shown that a beam can be represented in phase space or trace space, that the area covered by a beam in phase-space is conserved, and that it is convenient to use a beam ellipse to describe a beam. Emittance is the figure of merit generally used to describe the beam quality [13, 21, 22, 23]. It is a measure for the average spread of particle coordinates in 6D position-momentum phase space. The SI unit used for emittance is $m \cdot rad$. It is custom to calculate the emittance of the beam in the different projection planes. This means the beam has a transverse emittance ε_x and ε_y and a longitudinal emittance ε_z. For bunched beams with symmetry

planes in x- and y- direction all three emittances are required to describe the beam quality. In this chapter the projection in the (x, x') plane is used to explain and illustrate the different types of emittance. Although emittance is strongly related to the area of the beam in trace space, different types and definitions of emittance exist.

2.2.1 Geometric interpretation

The emittance that is most easy to understand intuitively is the geometric emittance. The geometric emittance is the area covered by the beam ellipse in trace-space [13, 24]. In section 2.1.2 the mathematical description of a beam ellipse in trace space is discussed and the Twiss parameters are introduced. In section 2.1.2 ε is used as a measure for the area covered by the ellipse. In the equations in section 2.1.2 the variable ε is actually the geometric emittance.

Although the geometric emittance is very intuitive, there are some practical issues when used for real beams. The ideal beams considered in theory have perfect Gaussian distributions, and are only subjected to conservative forces. These ideal beams form ellipsoids in trace space and it is therefore easy to consider the area covered by such an ellipse. In reality, the particle distributions are often not entirely Gaussian and can show distortions. These distortions affect the beam shape. In figure 2.2 an example of a more realistic beam in trace space is given. Since the area itself is not an ellipsoid, the ellipsoid that contains all particles gives a wrong indication of the emittance.

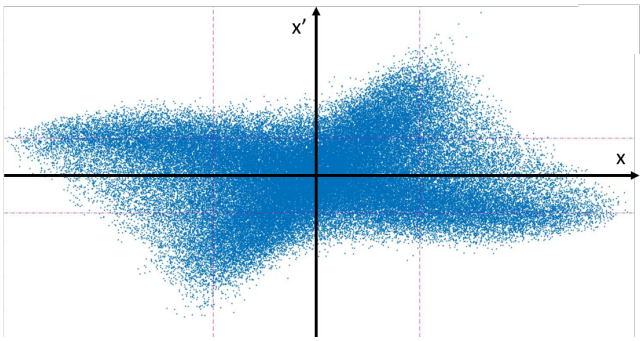

Figure 2.2: Example of a particle distribution in the x-x'trace space plane for a distorted beam

2.2.2 Root mean square emittance

An alternative, but commonly used form of emittance is the root mean square emittance. This form of emittance does not directly relate to the area a beam occupies in trace space, but is calculated from the distribution of spatial coordinates and divergence of the beam. It is a more statistical interpretation of the beam quality. The rms-emittance can be calculated with

$$\varepsilon_{x,rms} = \sqrt{< x^2 >< x'^2 > - < xx' >^2} \tag{2.5}$$

In this equation, $< x^2 >$ and $< x'^2 >$ are respectively the second moments of the position and the divergence of the electrons and $< xx' >$ is the mix term or correlation term [13, 23]. Note that the mix term is zero in a waist. In the calculation of the rms-emittance all particles are taken into account, however this does not mean that all particles are necessarily covered by an ellipse with area $\varepsilon_{x,rms}$.

2.2.3 Normalized emittance

The root mean square emittance in equation 2.5 is dependent on the divergence. When the energy of a beam is changed this normally doesn't happen with the same ratio in every direction, but is specifically directed to the main direction of propagation. During acceleration or deceleration, the divergence of the beam is changed. For an accelerating beam, the divergence decreases and therefore the emittance calculated with equation 2.5 also decreases.

However, it can be argued that the quality of the beam doesn't necessarily get better upon acceleration of the beam. When the beam would be decelerated to it's original energy without other influences, the emittance would be the same as the original emittance. To be able to track the quality of a beam throughout a beamline, the energy dependency of the emittance must be accounted for.

Instead of projecting the particles to trace-space, the particles can also be projected to momentum-space. Since the momentum in the directions perpendicular to the direction of beam propagation are independent of the momentum in the direction of beam propagation, the area covered by the particles in transverse momentum-space is independent of the beam energy in its direction of propagation. For the small angle approximation ($x' << 1$), the transverse momentum (p_x, p_y) and the divergence of the beam (x', y') are related to each other as

$$p_x = \gamma m v_x = \gamma m v_z \frac{v_x}{v_z} \approx \gamma \beta m c x' \tag{2.6}$$

where γ is the Lorentz factor and β is the relativistic beta factor, m is the particle mass and c is the speed of light. Calculation of the emittance using the momentum space results in the following relation between the normalized emittance ε_n and the energy dependent emittance ε where ε can be the geometrical emittance or the rms emittance [13, 23]

$$\varepsilon_n = \gamma \beta \varepsilon \tag{2.7}$$

2.3 Initial emittance

Electron emission from a metal or semiconductor is the initial particle source for the majority of electron accelerators. Different types of emission processes can take place, the most important ones being photo-emission, thermal emission and field emission. A finite region of the emitter is subjected to an emission process, which results in the ejection of electrons. Due to various effects, including surface imperfections, variations in initial momentum of the bound electrons and variations in photon energy (photo-emission) the electrons are emitted with a finite transverse momentum. As a result from the finite emission region and the finite transverse momentum, the initial beam already occupies a certain area in phase-space. Since the mix term $< xx' >^2$ is assumed to be zero at emission, the initial emittance the product of the initial root mean square beam size ($\sigma_x = \sqrt{< x^2 >}$) and initial root mean square divergence ($\sigma_{x'} = \sqrt{< x'^2 >}$). From Liouville's theorem follows, in absence of energy dissipation and non-conservative forces, that the initial normalized emittance is also the minimum normalized emittance that can be reached along the beamline [25]. The initial emittance is often called thermal emittance. However this can be confusing since heating of the cathode is not the sole reason for the occupied phase space area.

2.3.1 Photo-electric emittance and Schottky effect

In the 100 kV DC photo electron gun used in this project (for more specifications regarding the setup see section 5.2), electrons are emitted from the copper cathode surface through the process of photo-emittance. In order to remove an electron from the cathode's surface, the electron has to gain enough energy to overcome the (surface) work function ϕ_0. The work function is the minimum energy required to remove an electron from the Fermi level in a solid and let it escape to vacuum. Using a simplistic shell atomic model, the amount of energy is an intrinsic property of the material, although it is also affected by surface properties like lattice orientation, surface roughness and cleanliness. Consequently when measuring the work function of copper the results vary between 4.31 - 4.98 eV [26, 27, 28].

Electric fields present at the cathode surface lower the surface barrier and thereby lower the energy required for an electron to escape to the vacuum. This effect is called the Schottky effect and necessitates the introduction of an effective workfunction (ϕ_{eff})

$$\phi_{eff} = \phi_0 - \phi_{Schottky} = \phi_0 - \sqrt{\frac{e^3 \beta^* G_a}{4\pi\varepsilon_0}} \tag{2.8}$$

where G_a is the electric field, e is the electron charge and ε_0 is the vacuum permittivity. The surface enhancement factor β^* (note that this is not the relativistic $\beta = \frac{v}{c}$ factor) accounts for local stronger fields due to surface roughness, its value is often set to 1 (perfectly flat surface). Values between 1 and 500 are reported [16, 29, 30].

Directly at the source, it is assumed that the position of the electrons and their divergence are uncorrelated. With this assumption, the normalized rms emittance can be simplified to $\varepsilon_{n,rms} = \sigma_x \sigma_{x'}$. The energy imparted on electrons by incoming photons will lead to a transverse momentum distribution. This transverse momentum distribution can be expressed as a temperature of the electrons $k_B T_b \simeq (h\nu - \phi_{eff})/3$ where k_B is the Boltzmann constant and T_b is the electron temperature [16]. For this transverse momentum distribution the photo-electric normalized divergence is $\sigma_{x'} = \sqrt{\frac{k_b T_b}{m_e c^2}}$ where $m_e c^2$ is the rest mass of an electron [31, 32]. Multiplication with the rms laser spot size results in the initial photo-electric normalized root mean square emittance

$$\varepsilon_{x,photo} = \sigma_x \sqrt{\frac{k_B T_b}{m_e c^2}} \tag{2.9}$$

2.3.2 Magnetic emittance

Along with the photo-emission process, there are other factors that can contribute to the initial emittance. One of them is the presence of a magnetic field at the cathode [33]. A solenoid is placed at the exit of the electron gun in order to counteract the rapid expansion of the electron beam due to space-charge forces. However, the solenoid not only provides a focusing magnetic field for the off-axis particles, but also has a longitudinal field component. In principle a solenoid will provide symmetric kicks to the input and output beam and emittance is conserved. However, since the cathode is positioned in the solenoid field, the symmetry between input and output kick is broken and as a result the magnetic normalized root mean square emittance ($\varepsilon_{n,mag}$) contributes to the total emittance [34, 35]

$$\varepsilon_{x,mag} = \frac{e\sigma_x^2 |B_z|}{2 m_e c} \tag{2.10}$$

In this equation σ_x is the rms size of the electron beam on the cathode, and B_z is the magnetic field in z-direction (along the line of beam propagation).

2.3.3 Space-charge effects

All electrons have a negative electron charge e, and are therefore repulsive to each other. The forces the beam exerts to itself are called self-fields. In the the collisional regime, neighboring particles interact with each other and particles can be scattered by immediate neighbors. The interactions are not a smooth force, but instead cause small random displacements. When the effect of a single charge is shielded by other particles the space charge forces are smoothed and collective effects are dominant for the beam dynamics [36], this is the space charge regime. The smoothed space charge forces can be treated as external forces applied to the beam. The smoothed space-charge force consists of a linear and a non-linear component which depends on the position of the particle in the beam. The non-linear component distorts, the phase-space distribution, thereby causing emittance growth [37]. For bunched beams created with a photo cathode, the main initial space-induced emittance growth mechanism is found to be the variation of the transverse space-charge force along the bunches axial position during the initial expansion of the bunch. This type of emittance growth can partly be counteracted by refocusing the expanding beam with a solenoid directly after the cathode [37]. There are other emittance growth mechanisms induced by the non-linear component of the space-charge forces, the dominant mechanism is dependent on the beam properties and beamline layout [37].

2.3.4 Total initial emittance

The total normalized root mean square initial emittance (for the x-x' plane $\varepsilon_{x,tot}$) can be calculated from all separate contributions [33]

$$\varepsilon_{x,tot} = \sqrt{\varepsilon_{x,photo}^2 + \varepsilon_{x,mag}^2 + \varepsilon_{x,other}^2} \tag{2.11}$$

The contributions of $\varepsilon_{x,photo}$ and $\varepsilon_{x,mag}$ are already explained in the sections above. Other contributions, for example due to thermal effects and fringe fields, are included in the term $\varepsilon_{x,other}$.

2.3.5 Beam initialization

For the 100 kV DC photogun described in section 5.2, $h\nu = 4.65$ eV (UV wavelength of 266 nm), $G_a = 12.5$ MV/m [15], $\phi_0 = 4.31$ eV (Copper workfunction), $\beta^* = 1$ (surface enhancement factor). The electron temperature is calculated to be $k_B T_b \simeq 0.16$ eV. With a laser spot size $\sigma_x = 200$ μm this results in an initial photo emittance of $\varepsilon_{x,photo} = 110$ nm·rad. In this calculation the surface enhancement factor is assumed to be 1 for simplicity, in reality the value can vary over a large range due to surface roughness [16, 29, 30]. The magnetic field $B_z = 15.8$ mT at the cathode causes an initial magnetic emittance of $\varepsilon_{x,mag} = 46$ nm·rad The total initial emittance is calculated to be $\varepsilon_{x,tot} = 119$ nm·rad. In this theoretical calculation the electron temperature was calculated based on the photon energy, the surface work function and the decrease in work function due to the present electric field. Many experimental studies have looked into the initial emittance of copper cathodes. Although the theoretical value of electron temperature is calculated from the photon energy and the effective surface workfunction, measurements have shown that in reality the electron temperature is typically a factor 3-4 higher. Therefore it is more realistic to set the electron temperature to $k_B T_b = 0.5$ eV [16]. It seems that for photo-emission, the surface properties of the cathode significantly affect the electron temperature. The initial direction of emission is affected by fluctuations in surface direction, and on top of that the electric field can be increased by geometrical irregularities. Furthermore, the spectral width of the laser pulses can induce energy differences in the escape energy of the electrons. When the electron temperature in equation 2.9 is set to $k_B T_b = 0.5$ eV, the initial photo emittance is $\varepsilon_{x,photo} = 198$ nm·rad. Together with the magnetic emittance this results in a total initial emittance $\varepsilon_{x,tot} = 203$ nm·rad.

In GPT (General Particle Tracer), the initial particle distribution has to be defined by the user. In appendix C, the code used to initialize the beam is displayed.The input values for the initial momentum distribution are set to match an empirically determined initial emittance. Although the simulated emission process is not a realistic representation of the emission process, the results are generally in good agreement with experimental results [38]. In GPT two emittance routines are available. One of the emittance routines calculates the normalized root mean square emittance for a 2D phase space projection (ε_x and ε_y). In a solenoid field, the coupling between the x-x' plane and y-y' plane results in a temporarily increased value for the emittance. Instead of calculating the emittance for a 2D projection of the beam, the emittance (ε_r) for hypervolume x-x'-y-y' can be calculated. This routine accounts for the coupling between the x-x' plane and the y-y' plane. In table 2.1 the emittances calculated with both routines are displayed.

First, simulations are performed for electron beams without space-charge effects. Initially the gun solenoid in the simulation code is switched off, and the emittance is evaluated at 1 mm from the cathode. The beam is rotation symmetric and there is no coupling between the x-x' plane and the y-y' plane. The emittance routines for ε_x and ε_r give the same results. Since there is no magnetic field at the cathode, the result can be compared to the theoretical photo-electric emittance. The simulation is repeated with the gun solenoid switched on. Since the emittance in x-x' plane and y-y' plane are correlated within the solenoid field, the emittance should be evaluated outside of the solenoid field. At z=0.40m, both theory and simulations confirm that the magnetic field is negligible. Comparison of the results of ε_x and ε_r shows that the routines give a different outcome at the same position. This indicates that the x-x' plane and the y-y' plane are still correlated and therefore ε_r should be used. In the x-x'-y-y' subspace the emittance has not increased with respect to the emittance simulated in the situation without gun solenoid. This is not what was expected from the theoretical calculation.

Both the situations with and without solenoid are also simulated with space-charge taken into account. It is difficult to compare the results of these simulations to the theoretical values since space-charge effects are not accounted for in the theoretical photo-electric emittance and magnetic emittance. To check whether the simulation results are as expected, simulation results of low charge 10 fC bunches are compared to the simulation results without space charge effects. The outcomes of both simulations are in agreement. As expected the emittance simulated for 10 pC bunches is significantly higher than observed for simulations without space charge. In experiments, space-charge effects will affect the beam dynamics and emittance. Therefore simulations which include space-charge effects are more likely to be in agreement with experimental results.

Comparison of the theoretical emittance, the emittance calculated for an electron temperature of $k_B T_b = 0.5$ eV and the simulated values of the normalized rms emittance without space charge effects shows that all are of the same order. Since the input of the GPT code is based on previous experimental results, it is not too worrisome that the simulated value lies between the theoretical value based on the cathode workfunction and the empirical electron temperature of $k_B T_b = 0.5$ eV. It is however noteworthy that, although it would only be of small effect, the presence of a magnetic field at the cathode does not seem to affect the simulated value of $\varepsilon_{n,rrms}$. Measurements on the gun used in this project may give a more concrete result, but the numbers mentioned in this section do give a good indication of what initial emittance should be expected.

Table 2.1: Theoretical and GPT simulated values of initial emittance

	Normalized rms emittance $[nm \cdot rad]$
Theory: workfunction	
initial spot size: σ=200 μm	
Photo-electric emittance	110
Magnetic emittance magnetic field B_z at cathode 15.8 mT,	46
Total	119
Theory: empirical electron temperature	
initial spot size: σ=200 μm	
Photo-electric emittance	198
Magnetic emittance, magnetic field B_z at cathode 15.8 mT	46
Total	203
GPT simulation without space charge	
initial beam profile Gaussian: σ=200 μm	
No solenoid field: ε_x, ε_r	184
Magnetic field B_z at cathode 15.8 mT: ε_x	253
Magnetic field B_z at cathode 15.8 mT: ε_r	183
GPT simulation with space charge, 10 fC bunches	
initial beam profile Gaussian: σ=200 μm	
No solenoid field: ε_x, ε_r	184
Magnetic field B_z at cathode 15.8 mT: ε_x	252
Magnetic field B_z at cathode 15.8 mT: ε_r	182
GPT simulation with space charge, 10 pC bunches	
initial beam profile Gaussian: σ=200 μm	
No solenoid field: ε_x, ε_r	514
Magnetic field B_z at cathode 15.8 mT: ε_x	665
Magnetic field B_z at cathode 15.8 mT: ε_r	664

2.4 Solenoid magnetic lenses

To build properly working charged particle beamlines and manipulate and control the beam such that experiments can be done, charged particle optical devices are needed. Charged particle motion can be controlled by electric and magnetic fields. Solenoid magnetic lenses are frequently used to focus low energy electron beams [39].

2.4.1 Solenoid fields

The magnetic fields produced by an infinitely long and thin solenoid can be calculated by Ampère's law. An infinitely long and thin solenoid only has a uniform longitudinal component inside the solenoid

$$B_z = \begin{cases} \mu_0 nI & \text{inside the solenoid} \\ 0 & \text{outside the solenoid} \end{cases} \tag{2.12}$$

where n is the number of windings per meter, I is the solenoid current and μ_0 is the vacuum permeability [40]. In reality, solenoids are neither infinitely thin nor infinitely long. The first generalization is to give the solenoids a finite length. Because of the finite length, the symmetry is partially broken. Biot-Savart's law can be used to calculate the contribution of each wire section. For a solenoid with length L, radius r, n windings per meter and a current I, the on-axis longitudinal magnetic field B_z at position z w.r.t. the center of the solenoid is

$$B_z(z) = \frac{\mu_0 nI}{2}\left(\frac{z + L/2}{\sqrt{(z + L/2)^2 + r^2}} - \frac{z - L/2}{\sqrt{(z - L/2)^2 + r^2}}\right) \tag{2.13}$$

Often multiple layers of windings are stacked on top of each other. The radius for each layer of windings is slightly different, and the contribution to the magnetic field of the windings of the outer stack is slightly less than the contribution of the windings of the inner stack. To account for this effect, the solenoid is modelled to be a stacking of finite thin solenoids each different radius. The total solenoid field is calculated by summation of the contributions of the thin finite solenoids. For a solenoid with m layers of windings, an inner radius r_{min}, an outer radius r_{max} the on-axis magnetic field B_z at position z w.r.t. the end of the solenoid is

$$B_z(z) = \frac{\mu_0 nI}{2m}\sum_{i=1}^{m}\left(\frac{z + L/2}{\sqrt{(z + L/2)^2 + (r_{min} + (i - \frac{1}{2}) \cdot \frac{r_{max} - r_{min}}{k})^2}} - \frac{z - L/2}{\sqrt{(z - L/2)^2 + (r_{min} + (i - \frac{1}{2}) \cdot \frac{r_{max} - r_{min}}{k})^2}}\right) \tag{2.14}$$

For infinite thin solenoids, the magnetic field inside the solenoid is uniform. The magnetic field lines of a finite solenoid form closed loops ($\nabla \cdot \mathbf{B} = 0$). Therefore the magnetic field at the edges of the solenoid has an off axis radial component and the longitudinal field is dependent on radial position r. The off-axis field components $B_r(r, z)$ and $B_z(r, z)$ relate to the on-axis magnetic field $B(z) = B_z(z)$ as [13]

$$B_r(r, z) = -\frac{r}{2}B'(z) + \frac{r^3}{16}B'''(z) + \textit{higher order terms} \tag{2.15}$$

$$B_z(r, z) = B(z) - \frac{r^2}{4}B''(z) + \textit{higher order terms} \tag{2.16}$$

2.4.2 Magnetic lens

Due to conservation of canonical angular momentum (Busch's theorem [35]) the solenoid has a rotational symmetric focusing effect on passing charged particle beams. For the simplified situation, where the space-charge forces are ignored and the paraxial approximation ($v_x, v_y << v_z$) is valid, the beam dynamics for a cylindrical, uniform distributed beam in an axisymmetric magnetic solenoid field can be derived.

The magnetic field of the solenoid exists of a radial component (equation 2.15) and a longitudinal component (equation 2.16). In the absence of transverse momentum, only the first order terms are taken into account.

The focusing effect of a solenoid can most easily be explained with the hard-edge approximation. The solenoid magnetic field is splitted into three regions each with a constant on-axis component of the magnetic field. In figure 2.3 an overview of the situation is displayed. Particles propagate through field free region 1 to region two with magnetic field $B_z = B_0$. On the edge of the two regions the magnetic field has a radial component which gives the electrons an azimuthal kick and causes the electrons to propagate along a helical trajectory with radius of curvature half the initial radial displacement and a rotation frequency equal to the cyclotron frequency. At the same time the particles rotate around the central solenoid axis with the Larmour frequency ω_L. This results in a periodic radial velocity with respect to the central solenoid axis. On the edge between region 2 and 3 the electrons experience an azimuthal kick similar in magnitude but in opposite direction as the kick on the edge between region 1 and 2. This kick causes the azimuthal velocity that causes the helical motion to go back to zero. Only the radial and longitudinal velocity components remain. This causes focusing of the beam.

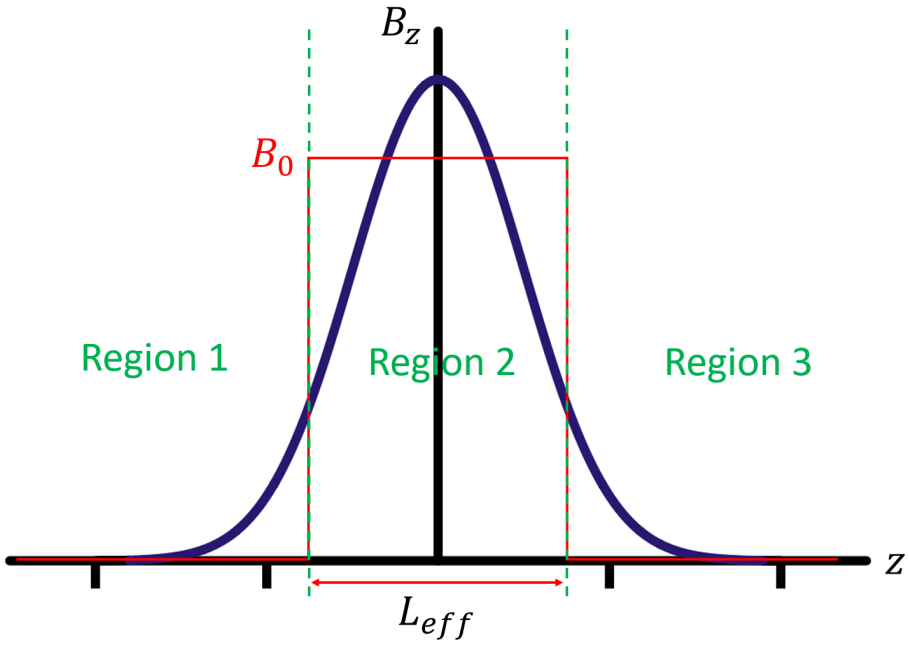

Figure 2.3: A sketch of the hard-edge approximation of a solenoid field. In the figure the blue line represents the actual on-axis component of the magnetic field. The red line represents the hard-edge approximation of the on-axis magnetic field with $B_z = 0$ in region 1 and 3 and $B_z = B_0$ in region 2. The region two has a width equal to the effective solenoid length L_{eff}.

The hard-edge approximation is a useful tool to discuss and understand the lens effect. However, it is not always necessary to use this approximation in calculations. If the thin lens approximation is valid ($L << v_z/\omega_L$) the focal length can be calculated for an arbitrary spatial variation of $B(z)$. To find the focal length f, the magnetic field profile must be integrated over the entire field region

$$\frac{1}{f} = -\frac{r'}{r} = \int_{-\infty}^{\infty} k^2 dz = \frac{e^2}{4\gamma^2 m^2 v_z^2} \int_{-\infty}^{\infty} B(z)^2 dz \tag{2.17}$$

[35]. In this equation $k^2 = \frac{e^2 B(z)^2}{4\gamma^2 m^2 v_z^2} = \frac{\omega_L^2}{\beta^2 c^2}$ is a strength parameter for the solenoid lens. This strength parameter

can also be used to calculate the angle of beam rotation caused by the solenoid field.

$$\phi = \int_{-\infty}^{\infty} k dz \tag{2.18}$$

[13, 21]. From equation 2.17, it can be seen that the focal length scales with $\gamma^2 v_z^2$. The focal length is different for particles with different energies. Solenoids have a less efficient focusing effect on high energy particles than they have on lower energy particles.

2.4.3 Lens action in phase-space

Electron beams are often represented in phase-space. The shape of the phase-space profile evolves during beam propagation. A matrix representation of the solenoid magnetic lens can be used to calculate the lens action on the phase-space position of the electrons. In the thin lens approximation ($L << v_z/\omega_L$), the radial position of the electrons is assumed to remain constant and only the projected slope is changed. The focusing effect of the solenoid can be described by matrix $M_{thinlens}$ and is only dependent on the focal length, which is given in equation 2.17

$$M_{thinlens} = \begin{pmatrix} 1 & 0 \\ -\frac{1}{f} & 1 \end{pmatrix} \tag{2.19}$$

The solenoid not only focuses the beam but also causes a rotation of the beam. In equation 2.18 the beam rotation is expressed as a function of strength parameter k. Since this rotation couples the $x - x'$ plane to the $y - y'$ plane a 4x4 matrix is required to describe the entire lens action [21]. Note that the strength parameter k is related to the focal length as stated in equation 2.17.

$$M_{solenoid} = \begin{pmatrix} \cos^2\phi & \frac{1}{2k}\sin 2\phi & \sin\phi\cos\phi & \frac{1}{k}\sin^2\phi \\ -2k\sin\phi\cos\phi & \cos 2\phi & k\cos 2\phi & \sin 2\phi \\ -\sin\phi\cos\phi & -\frac{1}{k}\sin^2\phi & \cos^2\phi & \frac{1}{2k}\sin 2\phi \\ -k\cos 2\phi & -\sin 2\phi & -2k\sin\phi\cos\phi & \cos 2\phi \end{pmatrix} \tag{2.20}$$

Chapter 3

Emittance measurement techniques

Different emittance measurement techniques like wire scanners [41], waist-scans [42], SEM grid measurements [43] and slit or pepper-pot measurements [44, 45] exist. Initially, the aim of this project was to use a pepper-pot to measure the emittance of the electron beam produced by the electron gun that will be used in the Smart*Light project. Due to time related issues, it was decided to start with the waist-scan measurement method instead of the pepper-pot measurement method. However, the pepper-pot technique was not completely put aside. Simulations are done to come to a design proposal of a pepper-pot in the final Smart*Light beamline. The results of these simulations are discussed in chapter 4. In this chapter, the waist-scan and pepper-pot measurement techniques are explained.

3.1 Waist-scan

Waist-scan measurements are often used to measure the transverse emittance of an electron beam [46, 47, 48]. The waist-scan method relies on the effect of a (magnetic) lens and drift section on the propagation of the beam through trace space. A solenoid is often used to focus the beam and the beam size is measured at a fixed distance from the solenoid. By changing the focal length of the solenoid, the beam size at the screen that is located at a fixed position also changes. The rms transverse emittance (see section 2.2 equation 2.5) can be calculated from the relation between spot size and focal length. Note that this emittance still needs to be normalized to the beam energy according to equation 2.7.

3.1.1 Derivation of the waist-scan fit function

Figure 3.1 is a schematic image of the setup used for a waist-scan. In this figure f represents an ideal thin solenoid with focal length f, l_2 is the distance between the ideal thin solenoid and the screen on which the beam size can be measured and l_1 is the distance between ideal thin solenoid and the virtual source with source size σ_v where the beam is in a waist. In a waist, there is no correlation between the spatial coordinates and the momentum coordinates. The beam ellipse is not tilted and the beam is said to be non-skewed.

The propagation of the beam through the linear optical system can be calculated when it is assumed that the beam is paraxial and all particles have the same longitudinal velocity. It is assumed that all optical elements of the linear optical system are ideal and infinitely thin. Furthermore it is assumed that the beam has a Gaussian trace space profile. Because of the ellipsoidal equidensity contours of a Gaussian beam this allows the representation in the form of a beam matrix or Twiss parameters (see section 2.1.2). In the following derivation it is assumed that space-charge forces and other inter-particle interactions are negligible.

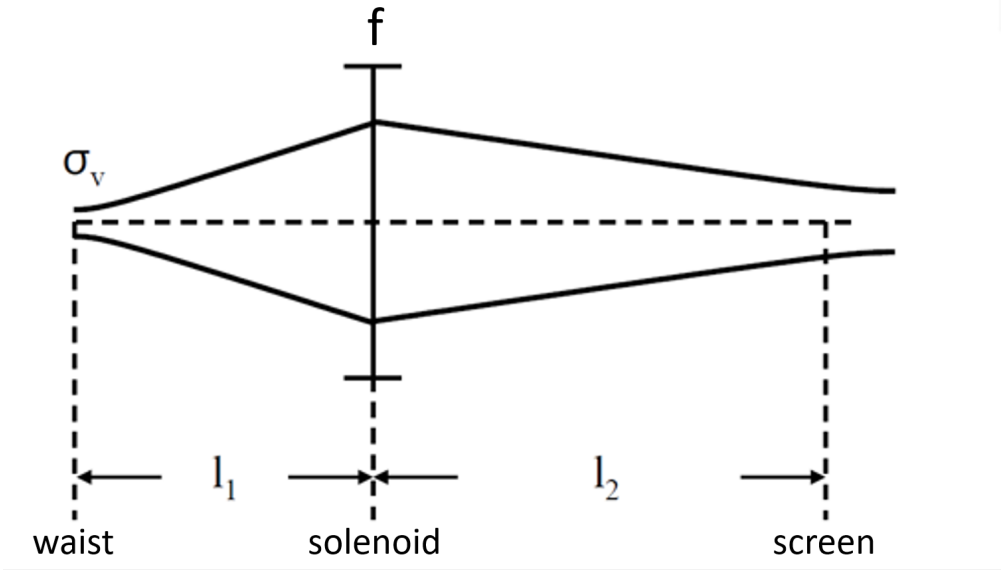

Figure 3.1: Schematic drawing of the waist-scan setup used to derive the waist-scan fitfunction [46]

A single transformation matrix that represents the linear optical system of figure 3.1 can be created by multiplying the transformation matrices of the drift sections and the lens action

$$M_{transfer} = M_{l_2} M_{lens} M_{l_1} = \begin{pmatrix} 1 & l_2 \\ 0 & 1 \end{pmatrix} \begin{pmatrix} 1 & 0 \\ -\frac{1}{f} & 1 \end{pmatrix} \begin{pmatrix} 1 & l_1 \\ 0 & 1 \end{pmatrix} = \begin{pmatrix} 1 - \frac{l_2}{f} & l_2 + l_1(1 - \frac{l_2}{f}) \\ -\frac{1}{f} & 1 - \frac{l_1}{f} \end{pmatrix} \tag{3.1}$$

In section 2.1.2 it is explained that the beam can be represented by a matrix σ_{beam} containing the Twiss parameters $\widehat{\alpha}$, $\widehat{\beta}$ and $\widehat{\gamma}$ and the beam emittance (see equation 2.2). The transformation matrix of equation 3.1 can be used to transfer matrix $\sigma_{virtual}$ containing the Twiss parameters at the virtual source position through the waist-scan setup of figure 3.1. This results in a beam description σ_{screen} of the beam at screen position σ_{screen}.

$$\sigma_{screen} = M_{transfer} \sigma_{virtual} M_{transfer}^T \tag{3.2}$$

For a non-skewed beam, $\widehat{\alpha} = 0$. Therefore relation 2.4 between the Twiss parameters reduces to $\widehat{\beta}\widehat{\gamma} = 1$. The beam size can be related to the Twiss parameters with $\sigma_x = \sqrt{\varepsilon\widehat{\beta}}$, or with help of the relation $\widehat{\beta}\widehat{\gamma} = 1$ as $\sigma_x = \sqrt{\frac{\varepsilon}{\widehat{\gamma}}}$. During a waist-scan the spot size at the screen is measured. By substituting the relations between the Twiss parameters, the emittance and virtual spot size into the expression found for $\widehat{\beta}_{screen}$ the measured beam size at the screen can be related to the properties of the optical linear system and the beam properties of the non-skewed beam.

$$\sigma_x = \sqrt{(l_1 l_2 - (l_1 + l_2) f)^2 \frac{\varepsilon^2}{\sigma_v^2 f^2} + (f - l_2)^2 \frac{\sigma_v^2}{f^2}} \tag{3.3}$$

When a waist-scan is performed, the beam size at the screen is measured and can be plotted as a function of the focal length of the magnetic lens. To determine the emittance equation 3.3 can be used as fit function [46]. The fit parameters for this fit function are the emittance ε (note that this emittance is not normalized), the virtual spot size σ_v and the distance to the virtual spot l_1. The distance l_2 between solenoid and screen is a constant in the setup and the measured distance is used as a constant in the fit function.

3.2 Pepper-pot

An alternative method to measure the transverse emittance of a charged particle beam is a pepper-pot measurement. For this measurement technique a plate with small holes, the pepper-pot, is inserted in the beam-path. In figure 3.2a, a schematic drawing of a pepper-pot plate is displayed. The pepper-pot method allows for the determination of different types (rms, 90%, 50%) of spatial resolved horizontal and vertical emittance profiles in one measurement [47, 49, 50]. The pepper-pot blocks most of the beam, and only allows small beamlets to propagate. The beamlets are allowed to drift over a certain distance, and then visualized on a screen. The relation between the spot-sizes of a beamlet on the screen, the initial hole size in the pepper-plot plate, the hole position in the pepper-pot plate, the position of the beamlet at the screen and the drift distance allows for the calculation of the emittance of this single beamlet.

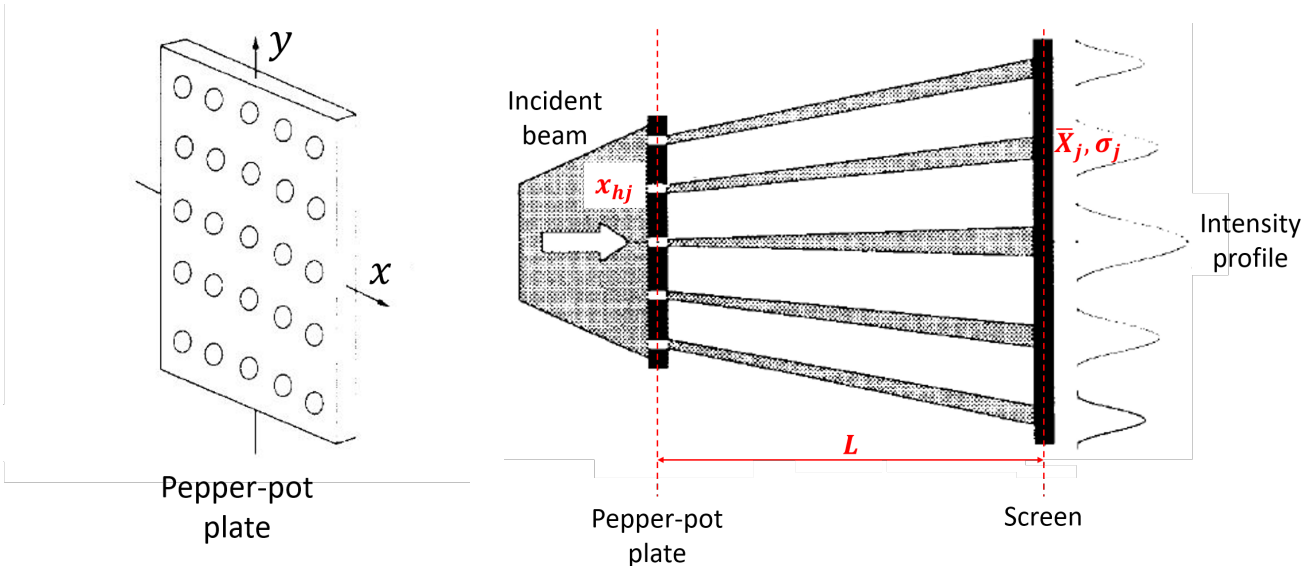

(a) (b)

Figure 3.2: Schematic drawings of a) a pepper-pot plate, b) the pepper-pot setup. In the pepper-pot setup, the hole position of hole j is indicated as x_{hj}, the average position of beamlet j is indicated as $\bar{X}_j$ and the size of the j^{th} beamlet is indicated as σ_j. [51]

3.2.1 Derivation pepper-pot emittance

Image 3.2b gives a schematic representation of a pepper-pot or slit experiment. The emittance in x- and y-direction is calculated separately following the same procedure. To calculate the emittance in x-direction the images of the pepper-pot beamlets in y-direction are summed up and vice versa. In this section, the derivation of the equation for the emittance in x-direction is discussed. The procedure can be repeated in order to find the emittance in y-direction.

The emittance calculated from a pepper-pot measurement is the rms-emittance at the position of the pepper-pot plate. In section 2.2, the differences between different types of emittances are discussed. The rms-emittance is defined as $\varepsilon_x \equiv \sqrt{< x^2 >< x'^2 > - < xx' >^2}$. Therefore methods to calculate the variance of particle position $< x^2 >$, the variance of particle divergence $< x'^2 >$ and the correlation between particle position and particle divergence $< xx' >$ from the measurement data are needed.

For a pepper-pot measurement, a few assumptions are made. The beamlets are assumed to be emittance dominated, this means that the space-charge effects in the beamlets and between neighbouring beamlets should be negligible.

Furthermore, it is assumed that the size of the holes in the pepper-pot plate are much smaller than the size of the beamlets as observed on the screen ($\sigma_{hole} << \sigma_{screen}$). This assumption allows for the holes to be described as point source, in the derivation all electrons of one beamlet originate from the same point in the pepper-pot mask.

The paper of Min Zhang [51] contains a detailed derivation of the emittance formula for pepper-pot or slit experiments.

$$\varepsilon_x^2 \approx \frac{1}{N^2}\{[\sum_{j=1}^{p} n_j(x_{hj}-\overline{x})^2]\cdot[\sum_{j=1}^{p}[n_j\sigma_{x'_j}^2+n_j(\overline{x'_j}-\overline{x'})^2]]-[\sum_{j=1}^{p} n_j x_{hj}\overline{x'_j}-N\overline{x}\overline{x'}]^2\} \tag{3.4}$$

In this equation N is the total number of electrons after the pepper-pot, and n_j is the number of electrons that propagates through the j$^t h$ hole. In a measurement it is difficult to obtain the actual number of electrons, instead a weighting of spot intensity can be used to define N and n_j. The hole position x_{hj} in the pepper-pot mask, and the drift length L between pepper-pot mask and screen are known. For every beamlet, the position of the center of the beamlet $\overline{X_j}$, and the rms size of the beamlet spot σ_j on the screen can be obtained by analyzing an image of the screen. The rms divergence of each beamlet $\sigma_{x'_j}$ can be calculated from the rms spot size and the drift length

$$\sigma_{x'_j} = \frac{\sigma_j}{L} \tag{3.5}$$

The mean position of the beam at the pepper-pot plate position can be determined by calculating a weighted average. The position of each hole is multiplied by the number of electrons that propagates through that hole and divided by the total number of particles.

$$\overline{x} = \frac{1}{N}\sum_{j=1}^{p} n_j x_{hj} \tag{3.6}$$

Due to the divergence of the beam, the beamlets show increase in spot size. Their average position also changes over drift length. The mean divergence $\overline{x'_j}$ of the j^{th} beamlet relates the position of the hole where the beamlet propagated through to the position of the beamlet on the screen

$$\overline{x'_j} = \frac{\overline{X_j}-x_{hj}}{L} \tag{3.7}$$

The mean divergence of all beamlets $\overline{x'}$ can be obtained by calculating the weighted average of the mean divergences of all beamlets.

$$\overline{x'} = \frac{1}{N}\sum_{j=1}^{p} n_j\overline{x'_j} \tag{3.8}$$

3.3 Waist-scan measurements vs pepper-pot measurements

3.3.1 Advantages and disadvantages of the waist-scan technique

The waist-scan technique is often used to measure a beam's transverse emittance. The main advantage of this technique is the ease of implementation. The only additional parts that need to be included in the beamline are an extra solenoid that can be used to focus the beam with different focal strengths and a phosphor screen on which the electron beam can be visualized.

There are also some disadvantages to the waist-scan technique. In order to calculate the emittance from the experimental data, assumptions regarding the absence of space-charge forces and the shape of the beam have to be made. In reality space charge forces do play a role. Since in focus the charge density is maximized their effect is even more important for a focused beam. The assumption that space-charge forces are negligible also becomes less valid for higher overall bunch charges. The relation between the spot size on the screen and the focal strength is derived under the assumption that the beam can be transferred by the linear system transfer matrix. To be able to use this method of transformation, the phase space equidensity contours are assumed to be elliptical and the

magneto optical system is assumed to be linear. In reality the beam will not consist of perfect elliptical equidensity contours, but will contain structures and the magneto optical system will not be perfectly linear. Both of these deviations are not taken into account, and can form a source of emittance growth between the virtual spot and the screen. The derivation of the waist-scan fit function is based on the assumption that the emittance is constant between the virtual spot and the screen. Emittance growth in this section is not taken into account.

The different error sources mentioned above can reduce the reliability of the waist-scan result. When studying the results obtained with this method, the inconsistencies with the assumptions should be considered, and one should have a critical look at the validity of the waist-scan method. Especially for bunches with a high charge density, difficulties are expected.

3.3.2 Advantages and disadvantages of the pepper-pot technique

The pepper-pot measurement technique will not be installed in the test beamline due to time related problems. However, it might be desirable to implement the technique in the final Smart*Light beamline. There are some main advantages of the pepper-pot technique over the waist scan technique.

First of all, the pepper-pot relates the measured emittance to a clear position along the beamline: the pepper-pot plate position. Furthermore the pepper-pot measurement method only requires one image of the beamlets projected on the screen. This results in a potential one-bunch measurement from which both the x- and y- emittance can be determined. For a waist-scan many images recorded for different waist-scan solenoid currents are required. This makes the waist-scan method vulnerable for fluctuations of the bunches over time. An one-shot measurement not only removes the potential error caused by fluctuations between different bunches, but can also possibly provide a real-time analysis of the beam quality. Since the beamlets all come from a different part of the original beam, the pepper-pot method offers a spatial resolved image of the beam quality. Not only the beam quality of the entire beam can be studied, but also possible relations to the shape or structure are captured. The last main advantage is that the pepper-pot method is less sensitive for space-charge effects than the waist-scan method. The pepper-pot mask filters out a significant part of the beam and only allows small beamlets to propagate. Space-charge effects are less likely to dominate the beamlets than to dominate the entire beam.

There are also some disadvantages of the pepper-pot method compared to the waist scan method. First of all, it is more difficult to implement a pepper-pot setup in a beamline. For the waist scan, only a phosphor screen needs to be inserted in the beamline. For the pepper-pot measurement a pepper-pot mask and a phosphor screen with a fixed distance with respect to each other need to be inserted. Furthermore, the use of a pepper-pot prevents visualization of the beam during the emittance measurement. Although it seems that pepper-pot measurements are less sensitive to invalidity of assumptions, there are also some issues that could complicate data analysis. Due to limited size and intensity it might be difficult to fit the beamlet on the screen. The beamlets needs to cover multiple pixels in order to observe an intensity profile and increase in spot size with respect to the hole size. The pixel size and intensity of the beam on the phosphor screen are not expected to be an issue for waist-scan measurements.

3.3.3 Conclusion

The pepper-pot emittance measurement seems to be better suitable to provide a complete and accurate indication of the emittance. The method seems to be less sensitive to space-charge effects. However, whether it will be possible to design and implement a pepper-pot in the Smart*Light beamline still has to be investigated. Simulations to come to a possible design will be performed in chapter 4. The waist scan method is easy to implement and for a general idea of the beam quality waist scan measurements are performed and discussed in chapter 6.

Chapter 4

Pepper-pot simulations

Due to time related issues it was decided to test the Smart*Light electron gun and UV-incoupler by measuring the emittance for different bunch charges with the waist-scan method. However, as discussed in section 3.3 the pepper-pot measurement method has significant advantages over the waist-scan method. The waist-scan setup will not be implemented in the final Smart*Light beamline. Nevertheless in this section the possibility to implement a pepper-pot experiment in the Smart*Light beamline is investigated.

4.1 Design pepper-pot holder

The Smart*Light setup is subject to many spatial limitations. It is not possible to implement a pepper-pot setup at an arbitrary position along the beamline. Within the current plans for the beamline (see figure 1.5), two options to implement a pepper-pot setup are investigated. The first option is to fit the entire pepper-pot setup in the diagnostic cross which is located at 45.4cm from the cathode. The main issue with this solution is the very limited amount of space inside the diagnostic cross in which the pepper-pot plate, phosphor screen and optic path towards the CCD need to be fitted. The second option is to use the phosphor screen already implemented in the diagnostic cross at 45.4 cm from the cathode and place a mechanism in the connection between velocity buncher cavity and diagnostic cross that can move the pepper-pot plate in and out of the beampath. This option is mechanically more difficult to realize but offers a larger drift length between pepper-pot plate and phosphor screen. For both options a camera that can be used to take images of the beamlet projection on the screen can be mounted to the window flange of the diagnostic cross.

To be able to perform simulations for the suggested pepper-pot setups first the diagnostic tools including pepper-pot plate, phosphor screen and light out coupling are designed. From the two designs specific information about the drift length L_d is obtained. This drift length L_d is crucial for the design of the pepper-pot plate itself and will be used in section 4.2 to determine the hole size and hole spacing.

Option 1: pepper-pot setup in diagnostic cross

The inner diameter of the vacuum cross is 63.5 mm. To be safe with the outer dimensions of the device, the basis of the pepper-pot device is chosen to be the same as the size of the phosphor screen holder and Faraday cup combination (see section 5.5) which is already in use and has a diameter of 54 mm. The mechanism for insertion and extraction in and out of the beamline is also kept similar to the mechanism for the phosphor screen holder and Faraday cup combination. To make sure the beam with rms beam size of 1.54 mm can be properly aligned to the pepper-pot plate the dimension of the pepper-pot plate is chosen to be 1x1 cm. In figure 4.1 schematic drawings for a potential device are displayed. The pepper-pot plate is mounted at a flattened side of the cylindrical plate and screen holder, the screen is mounted as far away from the plate as possible leaving just enough space to mount

a 45° mirror needed to couple the light emitted by the phosphor screen out. This potential setup leaves a drift length L_d of 4.3 cm. When the device is inserted into the beamline, the pepper-pot plate is positioned at 42.8 cm from the cathode and the phosphor screen is positioned at 47.1 cm from the cathode.

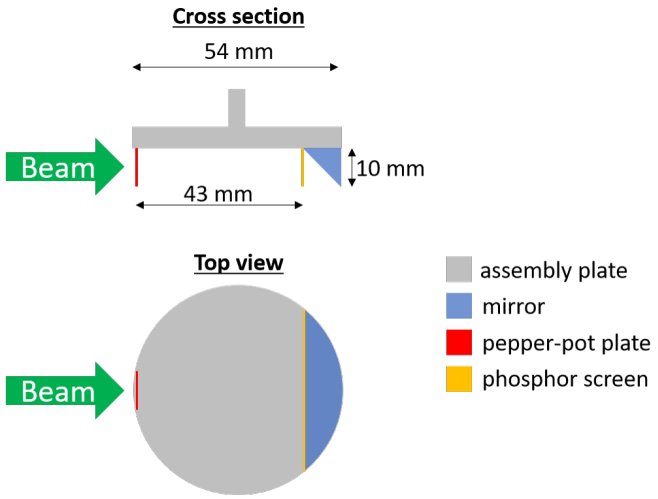

Figure 4.1: Schematic drawing of the idea of the potential pepper-pot device described as option 1. Both the pepper-pot plate and the phosphor screen are assembled in one device, and can be entered in the beampath in the vacuum cross at 45.4 cm from the cathode.

Option 2: pepper-pot in connection between cavity and cross and screen in diagnostic cross

The other option is to use two separate positions along the beamline to install the pepper-pot plate and the phosphor screen. The pepper-pot plate could possibly be mounted in the connection between velocity buncher cavity and diagnostic cross at 37.4 cm from the cathode. It is key that the pepper-pot setup can be lowered into and raised out of the beampath without breaking the vacuum. Possible options for inserting and retraction of the pepper-pot plate are a spring mechanism or insertion and retraction with a thread. The phosphor screen already used to visualize the beam can be used. This phosphor screen is positioned at 43.3 cm from the cathode and is already equipped with an insertion and extraction system. No second phosphor screen is needed. The drift length L_d between pepper-pot plate and phosphor screen for this potential setup is 5.9 cm.

4.2 Design pepper-pot plate

For a tantalum pepper-plate [52], the thickness required to stop 100 keV electrons is 29 μm [53]. The parameters that need to be optimized are the hole radius h and the hole spacing s. Drift length L_d for both option 1 and 2 are imposed by the results of the design options of the pepper-pot holder. The pepper-pot plate design requirements are that the beamlets should not overlap at the screen position, the beamlets should not be space-charge dominated and the hole size should be much smaller than the hole separation. Examples of pepper-pot design processes are given in [50, 54, 45].

GPT is used to simulate the beam propagation from cathode to pepper-pot plate position. The matlab script in appendix D then uses the phase space coordinates of each particle to relocate the particles to within range $s/2$ of a hole to a position within the hole (hole radius h). In figure 4.2, the redistribution of the particles is clarified. The particles are drifted each with their original divergence over distance L_d to the screen position. When a bin size that represents the area one CCD pixel represents on the phosphor screen is selected, the intensity profile on the

screen as would be observed for an actual measurement can be plotted.

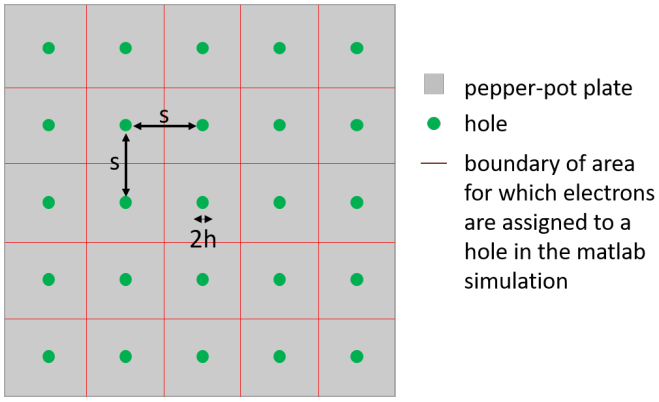

Figure 4.2: Example of how a pepper-pot plate is divided into smaller areas. All electrons falling within a certain area are reassigned to the point source in the middle of the area (the green dot). This redistribution of particles is used to simulate and study the beamlet propagation. The number of holes and the hole spacing in this schematic image is arbitrary.

Pepper-pot plate design for option 1

For design option 1, the drift length L is 4.3 cm. A 10 pC beam formed with a Gaussian UV-spot on the cathode with spot size of 200 μm has at the position of the pepper-pot plate (42.8 cm from the cathode) a rms beam size of 1.54 mm. The trace space projection of the beam to the x-x' plane is displayed in figure4.3.

First the maximum hole size for which the beamlets are not space-charge dominated is determined. For this purpose, the laminarity parameter ρ is introduced

$$\rho = \frac{\widehat{I}}{2I_A\gamma}\frac{\sigma_b^2}{\varepsilon_{n,rms}^2} \tag{4.1}$$

where $\widehat{I}$ is the peak current, I_A is the Alfvén current which is 17 kA, σ_b is the beamlet size which just after the pepper-pot plate is equal to h, and $\varepsilon_{n,rms}$ is the normalized root mean square emittance of the beamlet [36]. For a laminarity parameter $\rho \leq 1$ the beam is emittance dominated and space charge forces can be neglected. The average current density of the beam is 9.1e3 kA/m^2, a beamlet originating from a hole with hole radius h on average carries a peak current of $9.1 \cdot 10^3 \cdot \pi h^2$ kA. At the pepper-pot plate position, simulations have shown that the beam has a normalized rms emittance of 541 nm·rad. The emittance per beamlet is dependent on the hole position and the hole width. At this stage it is not possible to give an exact number for the emittance of each beamlet. Although this is a very rough estimate, for now the emittance is linearly scaled with the hole width. The emittance for a beamlet is estimated to be $\frac{h}{1.54\cdot10^{-3}} * 541$ nm·rad. Setting the laminarity parameter to 1 and substitution of the rough estimates for peak current and emittance per beamlet results in a maximum hole radius of 13 μm.

Taking into account that the beamlets should not overlap at the screen position, the ratio between beamlet width at the screen position and the hole separation should be smaller than 1. When it is also considered that the ratio between beamlet size on the screen and hole size should be larger than 1, it is possible to come up with a relation between hole radius h, hole separation s and drift length L

$$2h = 4\sqrt{3}\frac{\varepsilon_{n,rms}^2}{\gamma^2\sigma_{beam}^2}\frac{L_d^2}{s} \tag{4.2}$$

[50]. In this equation the divergence of a beamlet is approximated by the rms beam angle $\phi = \frac{\varepsilon_n}{\gamma\sigma_{beam}}$ of the entire

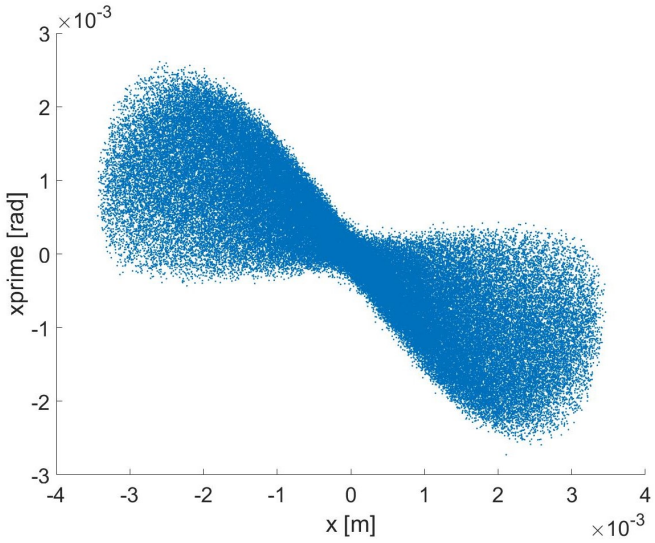

Figure 4.3: Trace space projection of the electron beam to the (x, x') plane at the pepper-pot plate position as presented in option 1 (42.8 cm from the cathode).

beam ($\varepsilon_{n,rms}$ is the normalized root mean square emittance of the beam and σ_{beam} is the beam size). One of the restrictions for the quality of the pepper-pot measurement will be the resolution of the image of the screen. For an optical setup as described in section 5.5.2, each CCD pixel represents an 20x20 μm area on the phosphor screen. To allow for a clear separation of the beamlets on the screen, a hole spacing of 10 pixels, which corresponds to 200 μm, is selected. Use of relation 4.2 resulted in an optimum hole radius of 3 μm. The design parameters for the pepper-pot plate are summarized in table 4.1.

The matlab script of appendix D is used to simulate the beamlet propagation from pepper-pot plate position to screen position. The intensity profile at the screen position is displayed in figure 4.4. The bin size in this image is set to 20 μm. the beamlet sizes in the center of the beam are much smaller than the beamlet sizes more to the sides of the beam. This was already expected from figure 4.3 since the spread in divergence is small close to the origin. Since the center beamlets only cover a few pixels, it might be difficult to fit them with a Gaussian. A larger drift length would allow the beamlets to diverge more and allow for a better fit quality. There is no overlap between the beamlets, from this histogram it could even be concluded that a smaller hole spacing of 120 μm is still sufficient. However, keep in mind that the real beam might have a larger emittance or show deviations. With the current hole spacing of 200 μm the beamlets would still be resolvable.

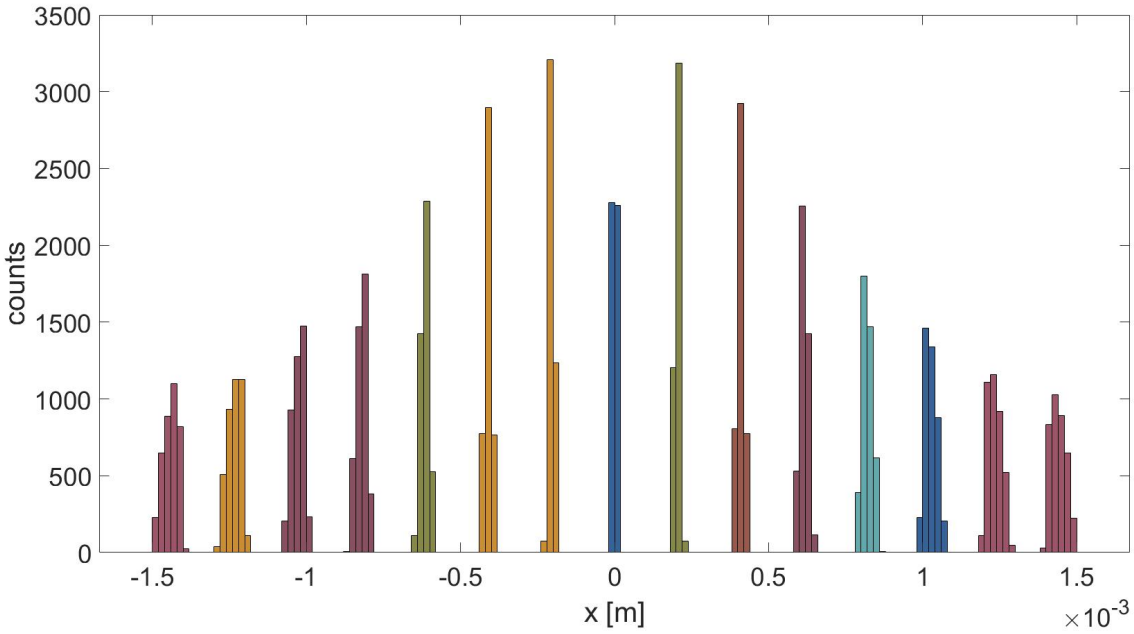

Figure 4.4: The intensity profile of the projection of the beamlets on the screen for setup option 1 and a pepper-pot plate with hole radius 3 μm and hole separation 200 μm. Each bin has a binwidth of 20 μm, this binwidth corrresponds to the area on the phosphor screen each camera pixel represents.

Pepper-pot plate design for option 2

The design process is repeated for the positioning of option 2. In figure 4.5 the trace space projection of the beam at 37.4 cm from the cathode is displayed. The rms beam size at the pepper-pot position is 1.60 mm. The peak current density at this position is 8.5e3 kA/m^2. The normalized rms emittance in x-direction as obtained from the GPT emittance is 602 nm·rad. From this information it is calculated that the maximum hole radius for which the beamlets are in the emittance dominated regime is $h = 15$ μm.

Equation 4.2 and a hole separation of 200 μm are again used to calculate the required hole width. This results in a hole radius of 6 μm. In matlab the beamlets are simulated according to the calculated pepper-pot plate geometry as summarized in table 4.1. Figure 4.6 shows the projection of the beamlets on the phosphor screen. The binwidth in the figure is 20 μm. The spots of the beamlets are wider than for option 1, however in the center the beamlets still only occupy a few bins and it might still be difficult to obtain the beamlet size from a fit with a Gaussian fit function.

Table 4.1: Pepper-pot design

	design option 1	design option2
pepper-pot plate position w.r.t. cathode	42.8 cm	37.4 cm
beam size on pepper-pot plate σ_{beam}	1.54 mm	1.60 mm
drift length L_d	4.3 cm	5.9 cm
hole radius h	3 μm	6 μm
hole separation s	200 μm	200 μm
resolution	15x15 holes	15x15 holes

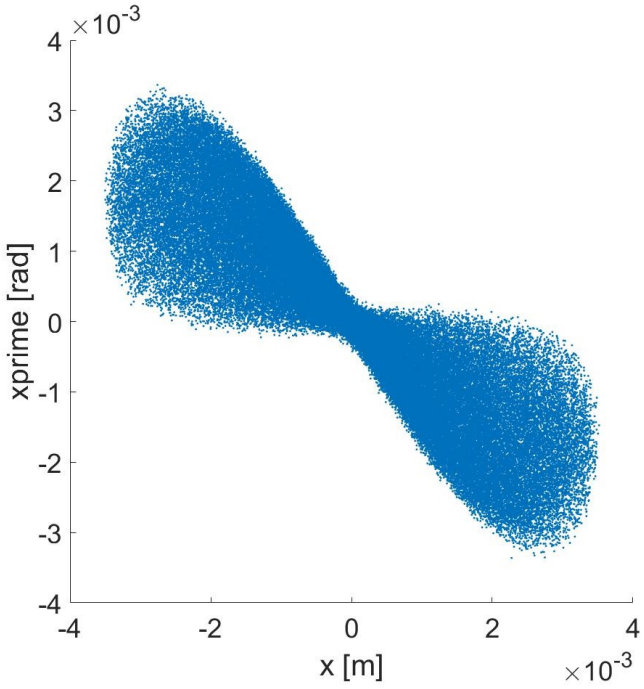

Figure 4.5: Trace space projection of the electron beam to the (x, x') plane at the pepper-pot plate position as presented in option 2 (37.4 cm from the cathode).

4.2.1 Remarks and conclusion

Two pepper-pot setup options are discussed. The results are summarized in table 4.1. For both design options the drift length is the limiting factor. An increase in drift length would allow the beamlets to diverge further, but at the same time limit the resolution of the emittance profile. It is advised not to limit the hole raster to 15x15 holes, but to increase the dimensions of this raster sufficiently (for example 30x30). This way, it will be easier to align the beam on the pepper-pot plate.

It might be possible to include one of the discussed designs in the Smart*Light beamline. There is however a detail that has to be kept in mind. The Smart*Light beamline is initially designed to be operated with bunch charges of 10 pC. Therefore the two presented pepper-pot designs are also designed for 10 pC bunches. If the bunch charge is at some point increased, this will affect the pepper-pot measurements. First of all, an increase in bunch charge will cause an increase in peak current density. Therefore the critical hole size for which the beamlets are emittance dominated will probably decrease. Since bunches with higher bunch charges also have a larger emittance, the beamlets are expected to diverge more over the same drift length. At some point, the spots on the phosphor screen might start to overlap.

Another remark regarding the design is that the current hole spacing is based on the calibration of the FLIR BLACKFLY (see section 5.5.2) as currently installed in the waist scan setup. When a different optical setup is used to monitor the phosphor screen on which the beamlets are projected, the binsize in the simulation might change. For smaller binsizes, the intensity profile of the spots is better resolved. For larger bin sizes, the proposed setups might become unusable since the intensity profiles of the spots become unresolvable.

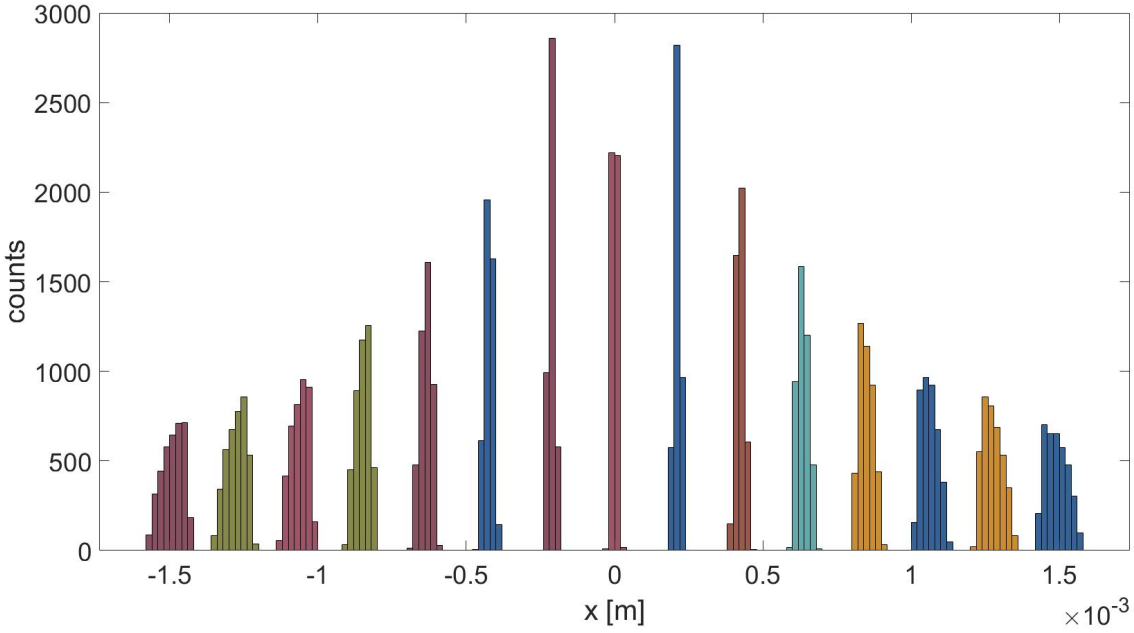

Figure 4.6: The intensity profile of the projection of the beamlets on the screen for setup option 2 and a pepper-pot plate with hole radius 6 μm and hole separation 200 μm. Each bin has a binwidth of 20 μm, this binwidth corrresponds to the area on the phosphor screen each camera pixel represents.

Chapter 5

Experimental setup

In this chapter, the experimental setup as used for the bunch charge measurements and waist scans will be discussed. First an overview of the beamline is presented, then the different elements of the beamline are subjected to a more in-depth discussion.

5.1 Beamline overview

In figure 5.1 a schematic drawing that includes the main elements of the beamline is displayed, the positions of the different elements with respect to the cathode are summarized in table 5.1. In this section the main elements will be introduced (from left to right). For most of the elements a more in-depth explanation follows later in this chapter. The first element in figure 5.1 is the 100 kV DC photo gun which consists of a vacuum vessel, cathode and iris shaped anode. More details will be given in section 5.2. The vacuum vessel is connected to a beam pipe with an inner diameter of 1.5 inch. The so called gun solenoid is placed around the beam pipe directly after the gun. This solenoid helps to reduce the expansion of the initial beam, details of this solenoid can be found in section 5.4.1. After the gun solenoid, a vacuum cross with two mirrors that are used for UV laser in- and out-coupling are installed. The first mirror reflects the incoming UV laser beam towards the cathode. The reflection on the cathode is directed towards the second mirror, this second mirror reflects the UV laser beam out of the beamline. More details of the path of the UV laser beam are discussed in section 5.3.2. The set of steering coils can be used to correct the direction of the electron beam, more information on the steering coils is given in section 5.4.2 and appendix B. The waist scan solenoid is part of the setup required to perform waist-scan emittance measurements. The waist-scan emittance measurement technique is already discussed in section 3.1. More details on the waist-scan solenoid can be found in section 5.4.1. In the diagnostic cross (a 5-way vacuum cross) at the end of the beamline a dual diagnostic tool consisting of a phosphor screen and a Faraday cup is installed. The phosphor screen can visualize the electron beam, the light produced by the phosphor screen is coupled out to a CCD camera outside of the vacuum. Both the phosphor screen and the Faraday cup are connected to an Ampere meter and can be used to measure the bunch charge. More information on the dual diagnostic tool, phosphor screen and Faraday cup is given in section 5.5.

The setup is operated at a vacuum pressure of about 10^{-7} mbar. To reach and maintain this vacuum level, three pump sets are installed. Each pump set consists of a backing pump and a turbo pump. One pump set is connected to the back of the electron gun vacuum vessel, one pump set is connected to one of the ports of the vacuum cross that is used for UV in-coupling, and one pump is connected to the beam pipe after the 5-way vacuum cross containing the diagnostic tools.

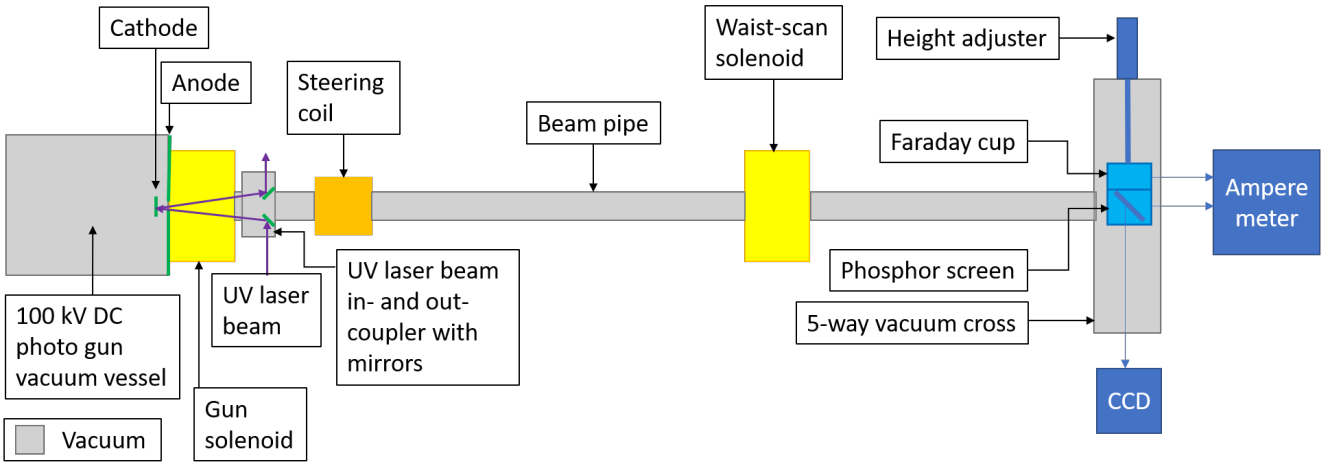

Figure 5.1: Schematic drawing of the beamline. The drawing is not in scale, although the distances give a good indication. The exact positions of the elements with respect to the cathode are summarized in table 5.1.

Table 5.1: The distances of the beamline geometry as schematically represented in figure 5.1, for elements with certain width, the reference point of this element is mentioned.

	Position w.r.t. cathode [cm]
cathode	0
interior anode plate	1.54
exterior anode plate	1.84
center gun solenoid	5.8
center steering coil	23.8
center waist scan solenoid	76.8
phosphor screen	117.8
entrance Faraday cup	117.8

5.2 Photo electron gun

At the start of the beamline, electrons need to be generated. This is done with an in-house developed 100 kV DC photo-electron gun. The properties of this gun are extensively studied by Thijs van Oudheusden in [15]. In figure 5.2, an artist impression of a 3-dimensional cross section of the 100 kV DC photogun is displayed. In this image, not only the outside vacuum vessel and the openings for the high voltage supply and vacuum pump are visible, but also the interior of the gun is visualized. The cathode is mounted on an inner conductor which is in contact with the high voltage supply. The insulating PEEK cone prevents breakdowns to take place between the inner conductor and the grounded vacuum vessel. In figure 5.3a an image of the cathode placed in the holder and mounted on the cylindrical conductor is displayed.

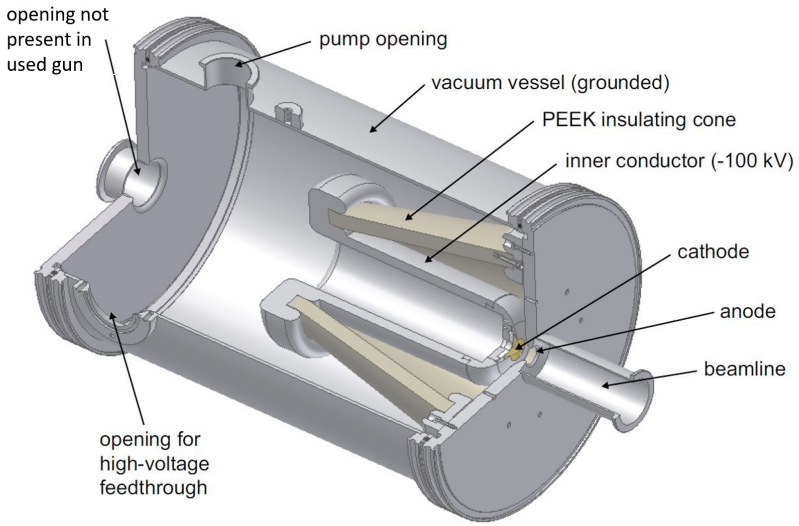

Figure 5.2: 3-Dimensional schematic cross section of the 100 kV DC photogun. [15]

5.2.1 Cathode

The cathode used in this gun is a new copper cathode. It is important there are no sharp edges since sharp edges could enhance the local electric field and cause breakdown. To fabricate a cathode with a surface as smooth as possible, a lathe is used. The cathode itself has a curved surface, but the center of the cathode is a flat surface with radius of 0.5 mm. The geometry of both cathode and anode are optimized in such a way that the electric field between the two is homogeneous [15]. Use of the lathe production method results in small grooves in the material. The reflection of the UV-beam on the grooves results in an interference pattern that can be visualized on the UV camera. A schematic drawing of the optical path from cathode to UV camera is displayed in figure 5.4. In figure 5.3b an image of the visualized groove structure is displayed.

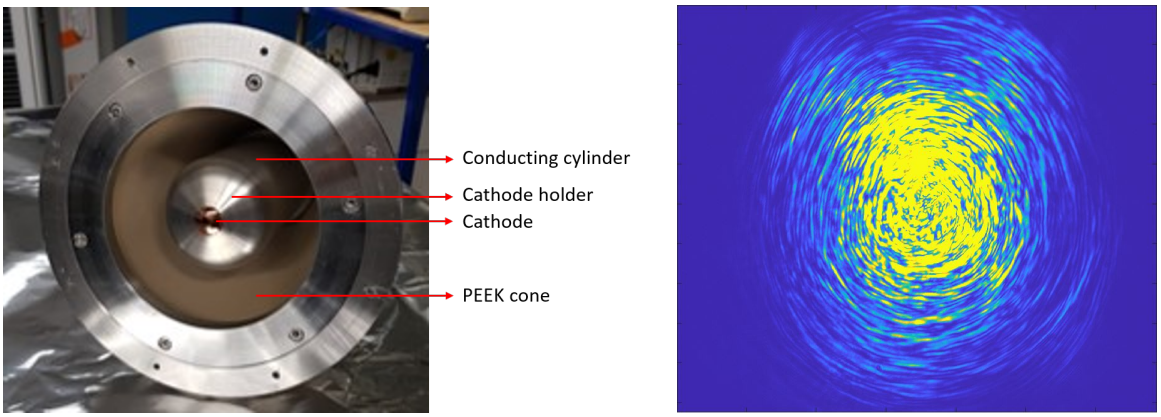

(a) (b)

Figure 5.3: a) Image of part of the inside of the electron gun. In the center, the copper cathode is placed in the cathode holder and the cathode holder is mounted on the cylindrical conductor. Part of the inside of the PEEK insulator cone is also visible. b) Interference pattern of UV reflected from the cathode. Image is made for an UV laser pulse that excites a bunch of 12 pC ± 15%.

5.2.2 High voltage power supply

The electric field at the cathode lowers the surface work function (see section 2.3.1), thereby enabling the excitation of electrons out of the cathode. Furthermore the electric field accelerates the free electrons towards the beamline. High electric fields do however come with some considerations, for electric fields higher than 25 MV/m breakdown of the vacuum can occur [15]. The current that runs through the breakdown arc can cause serious damage to the surfaces, so breakdowns should be prevented. For the 100 kV DC photogun used in this project, the maximum electric field at the cathode surface is 12 MV/m. Since the electric field strength is below the breakdown limit, major breakdowns should not take place.

The cathode is connected to a commercially available (Matsusada Precision Inc. AU-100N1.5L(220V)) 100 kV high voltage power supply while the anode is grounded. The high voltage power supply is connected to the electron gun with a coaxial cable. An in-house made feed through is designed in such a way that the vacuum is preserved and the field strength along the cable is kept below the breakdown limit. At the end of the cable the inner isolation is stripped from the cable and the cable is connected to the inner conductor, the high-voltage aluminum cylinder, onto which the cathode holder is placed.

5.2.3 Electron energy

The free electrons are accelerated by the electric field between cathode and anode. The kinetic energy of the electrons E_{kin} can be related to the rest mass of an electron m_e, the speed of light c and the Lorentz factor γ

$$E_{kin} = (\gamma - 1)m_e c^2 \tag{5.1}$$

This equation can be rewritten to find an expression for γ

$$\gamma = \frac{E_{kin}}{m_e c^2} + 1 \tag{5.2}$$

and this expression can subsequently be used to calculate the electron velocity

$$v = c\sqrt{1 - \frac{1}{\gamma^2}} \tag{5.3}$$

A voltage of 100 kV is applied over a gap of 1 cm. The electrons therefore have gained a kinetic energy of 100 keV after propagation through the gap. The initial energy of the free electrons after excitation out of the cathode surface is of the order of 0.5 eV which is much lower in comparison to the 100 keV gained by propagation through the gap. Therefore the electrons are assumed to be initially at rest. With this assumption, the Lorentz factor is calculated to be 0.655 and the electron velocity is calculated to be $1.64{\cdot}10^8$ m/s.

5.3 Optical setup electron gun

5.3.1 Laser system

The wavelength required to overcome the cathode surface work function is 266 nm. The laser system that is used to get to a laser beam of this wavelength starts with a Ti:sapphire oscillator (Coherent Mantis). The mode locked Mantis oscillator produces 30 fs pulses with a repetition rate of 75 MHz and an energy per pulse of approximately 4 nJ at 800 nm wavelength. The pulses are amplified by a Ti:Sapphire regenerative amplifier (Coherent, Legend) which is pumped by the Coherent Evolution 30 pump laser. After amplification, the pulse repetition rate is 1 kHz, pulses have a duration of 100 fs and the energy per pulse is in the order of 2 mJ. To prevent damage to the optical setup which is discussed in section 5.3.2 the repetition rate is reduced to 10 Hz.

The 800 nm laser pulses created by the femtosecond laser system are transported to the optical table where the actual electron gun and beamline are installed. To enable photo-emission from the cathode, the photon energy has to be tripled. The third harmonic generation module has three output beams of respectively 800 nm, 400 nm (the second harmonic) and the desired UV beam with a wavelength of 266 nm. An in-depth discussion of the working principles of the third harmonic generation module can be found in [55]. The 800 nm and 400 nm beams are blocked, and the UV beam is allowed to continue through an optical system towards the cathode.

5.3.2 UV beampath

In figure 5.4 a schematic drawing of the optical system starting from the output of the third harmonic generation module is shown. The elements that require further elaboration are numbered. At the position of element 2. a UV-filter can be inserted in the beampath. This UV-filter can be used to decrease the energy of the UV laser beam on the cathode, thereby decreasing the number of electrons per electron bunch. Lens 1. is used to focus the laser beam close to the (first) aperture (depending on the desired UV laser beam profile element 3. or 4.). To create a Gaussian UV laser beam profile, only one 150 μm aperture (element 4.) is inserted in the beam. This aperture works as a spatial filter and only allows the Gaussian mode to propagate, the other modes are blocked. In figure 5.5a an image of a Gaussian laser profile is displayed. The intensity profiles along the horizontal and vertical black line are plotted in the side graphs and compared to the initial bunch profile simulated with GPT. The bunch simulated in GPT has a spatial Gaussian distribution with cutoff at 3σ (3 times the standard deviation) and a σ of 140μm. To create a truncated Gaussian UV laser beam profile, two apertures (both elements 3. and 4.) are inserted in the beam. The first 100 μm aperture again only allows the Gaussian mode of the beam to propagate. After the first aperture, the beam diverges again but the Gaussian profile remains. By inserting the 150 μm aperture the tails of the Gaussian beam are blocked, and a truncated Gaussian profile is created. In figure 5.5b an image of the truncated Gaussian UV laser beam profile is displayed. Again the intensity profiles along the horizontal and vertical black line are plotted in the side graphs. The profile is compared to the initial beam profile simulated in GPT. The best match was found for a spatial Gaussian distribution with cutoff at 1.2σ (1.2 times the standard deviation) and a σ of 250μm. The histograms in figure 5.5b represent the profile of the initial beam in GPT.

The beam which now has the desired profile continues to a second lens (element 5.), this lens is used to image the (second) aperture on the cathode. The beam propagates through a sapphire window into the vacuum system, in the vacuum system the beam is reflected by the in-coupling mirror towards the cathode. Because of the structure of the cathode, the part of the beam that is reflected from the cathode forms an interference pattern. The reflected beam is coupled out of the vacuum system via a second window and imaged on the UV camera by lens 7..

Due to the intensity of the UV-beam part of the beam leaks through mirror 6., and continues towards the Sony XCD SX910UV camera. The beampath from mirror 6.to the UV camera and the beampath from mirror 6. to the cathode have approximately the same length. Therefore the image obtained on the CCD can be seen as the virtual cathode image. This image is used to determine the UV-laser spot size on the cathode.

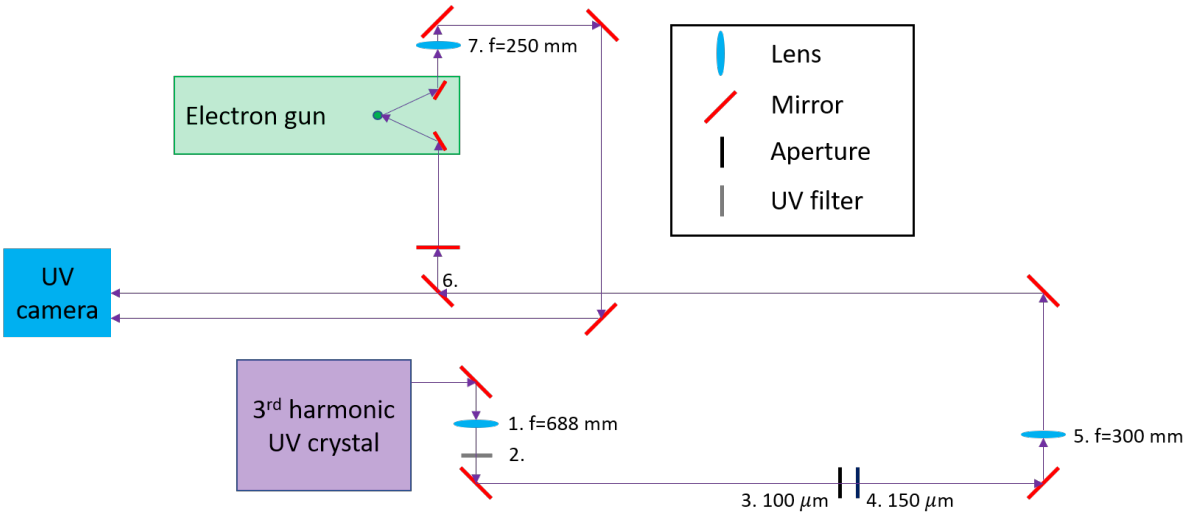

Figure 5.4: Schematic drawing of the UV beam path. Drawing contains the beam path from third harmonic generator to cathode and the beam paths of the imaging systems. In the drawing, the focal lengths of the lenses and the sizes of the aperture holes are indicated. The distances between the main optical elements are summarized in table 5.2.

Table 5.2: Distances in optical setup

Optical element	Distance between optical elements [cm]
exit 3rd harmonic generator - lens 1.	18
lens 1. - aperture 3.	59
aperture 3. - aperture 4.	2.5
aperture 4. - lens 5.	31
lens 5. - CCD	159.5
lens 5. - cathode	157.8
cathode - lens 7.	27.3
lens 7. - CCD	132

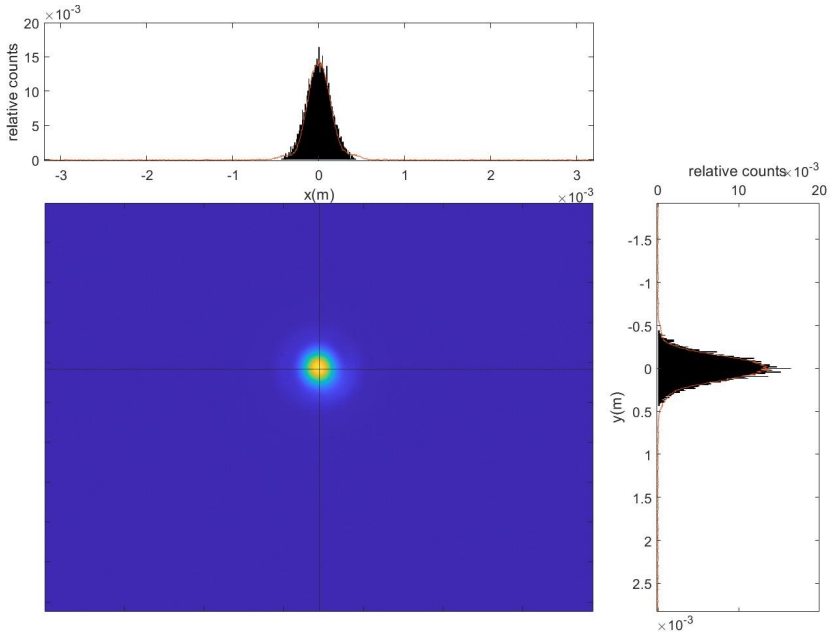

(a)

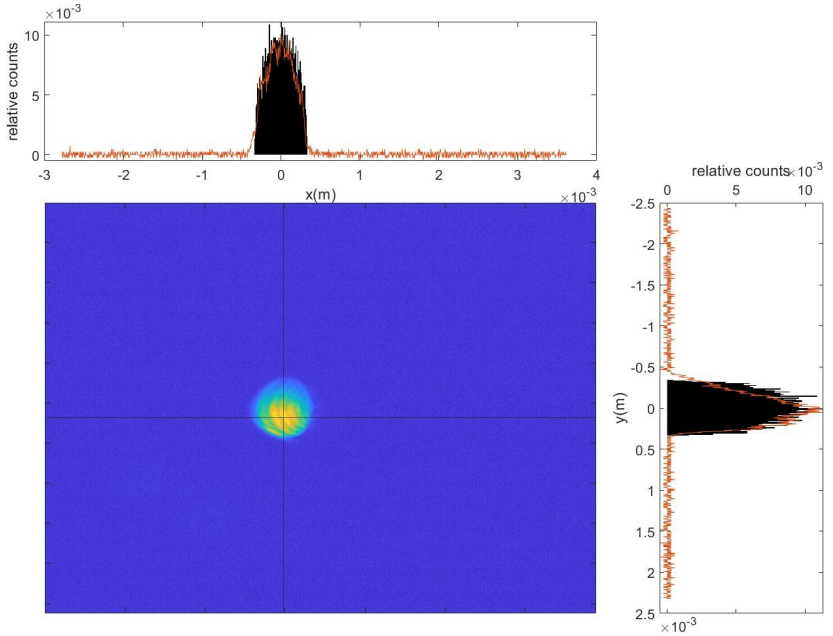

(b)

Figure 5.5: Image of the laser profile on the virtual cathode. The intensity profiles along the black lines are plotted at the sides and compared to the intensity profile of the initial bunch simulated in GPT (histogram). a) Gaussian profile created with a single 150 μm aperture, laser intensity for excitation of 12 pC $\pm$ 15% bunches. The initial beam simulated with GPT has a Gaussian profile with cutoff at 3σ and σ =140 μm. b) Truncated Gaussian profile created with a combination of a 100 μm and a 150 μm aperture, laser intensity for excitation of 15 pC $\pm$ 15% bunches. The initial beam simulated with GPT has a truncated Gaussian profile with a cutoff at 1.2σ and σ =250 μm.

5.4 Solenoids and steering coils

In section 2.4, the theory regarding the solenoid magnetic fields is covered. In this section, the purpose of the installed solenoids and the calibration measurements of the solenoid fields are discussed.

5.4.1 Main solenoids

In the setup (see figure 5.1) two identical solenoids are used. The first one is installed at the exit of the gun, with the center of the solenoid at 5.8 cm from the cathode. The purpose of this solenoid is to prevent blow-up of the beam due to space-charge forces and to control the emittance growth. The second solenoid is installed further downstream with the center of the solenoid at 76.8 cm from the cathode. This solenoid is used to perform the waist scan. In table 5.3 the specifications of the main solenoids are printed. The magnetic field along z-direction determines the focal strength of the solenoid, therefore it is important to know whether the actual field profile matches the field profile expected from theory and simulations.

Calibration results

The Hirst GM07 Gaussmeter is used to measure the on-axis magnetic fields (B_z). To be sure the probe is centered on the solenoid axis, two disks which just fit in the solenoid and have a centered hole of the size of the probe are positioned inside the solenoid. The distance of the probe to the solenoid center can be changed by changing the position of the probe standard on the rail. In figure 5.6 an image of the setup is displayed and the different elements are indicated.

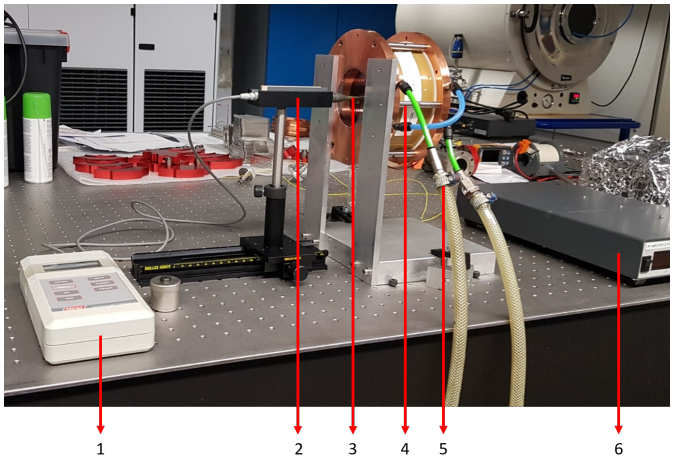

Figure 5.6: Setup used to measure the on-axis field of solenoid 2. Similar setups are used to measure the on-axis fields of solenoid 3 and the steering coils. 1) Hirst GM07 Gaussmeter, 2) probe standard, 3) on-axis field probe, 4) solenoid 2, 5) water cooling, 6) power supply

The on-axis magnetic field profile for a current of 10.0 A is measured as a function of distance to the center of the solenoid. In figure 5.7a the measured data points are plotted and fitted with a theoretical curve according to equation 2.14. For this fit, the current is used as the only fitting parameter. The current fitted to the measured B_z field is 10.64 ± 0.01 A, this is higher than the current indicated by the power supply display. There can be multiple reasons for this difference: a difference between the current as indicated by the power supply display and the actual output current (this can account for a current difference of ± 0.05 A), the actual winding of the solenoid and or a stronger dependency on the radius of each stack of windings of the theoretical equation. However, the most important conclusion that can be drawn is that the shape of the on-axis magnetic field profile matches the

theoretical prediction.

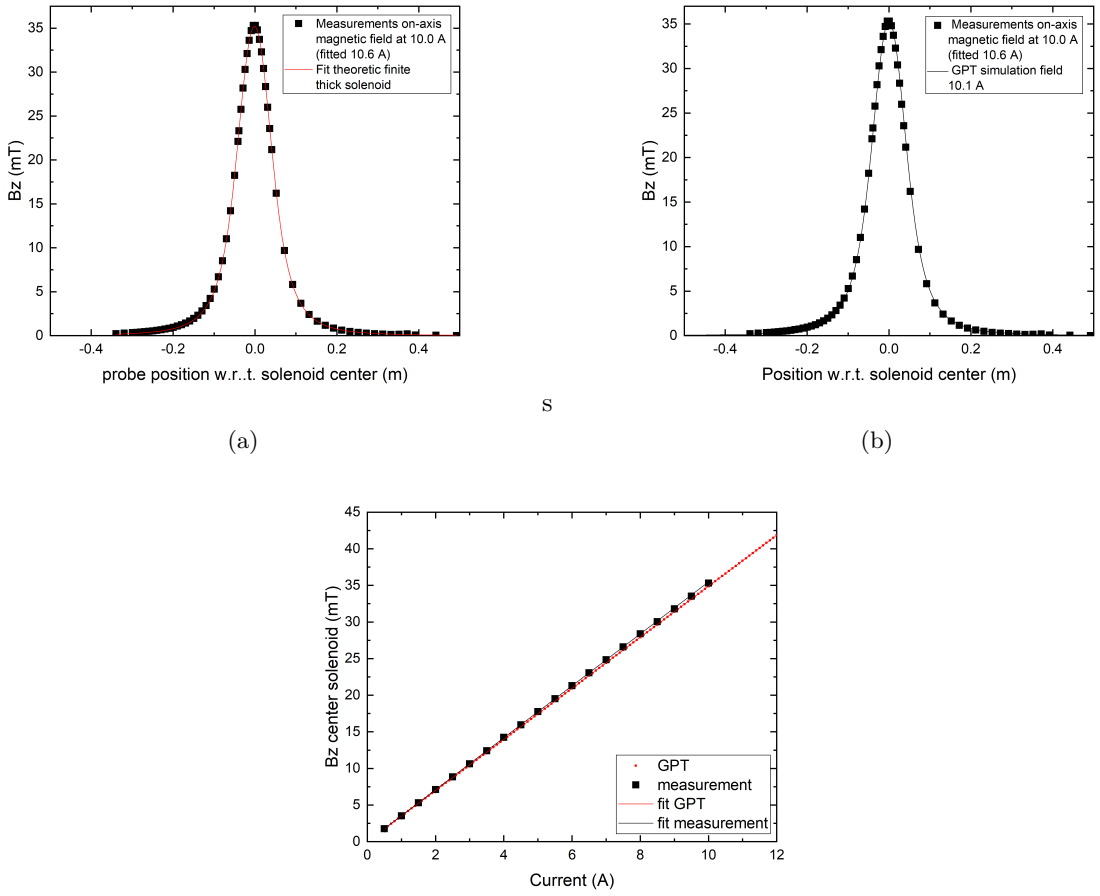

s

(a)

(b)

(c)

Figure 5.7: a) Measurements of the on-axis field profile for a solenoid current of 10 A. The data is fitted with equation 2.14 with solenoid current as fitting parameter, this resulted in a fitted current of 10.64 A. b) Measurements of the on-axis field profile for a solenoid current of 10 A and GPT simulated on-axis field profile for a current of 10.1 A. c) The measured and simulated on-axis peak magnetic fields as a function of solenoid current. The linear fits have a slope of respectively 3.55 mT/A for the measurement data and 3.49 mT/A for the GPT simulation data.

For a finite, thin solenoid the on-axis peak magnetic field is expected to scale linearly with the applied current. For a solenoid with 351 windings and a length of 61 mm, the theoretical slope is calculated with equation 2.13 to be 3.6 mT/A. To check this, the center peak magnetic field is measured for currents between 0.5 A and 10.0 A. For each measurement, the effective current is identified by fitting the peak field to the theoretical function. In figure 5.7c the measured peak field is plotted as a function of the solenoid current. The data points are fitted with a linear fit function with zero offset. The slope of the fitted linear function is 3.55 mT/A. This is less than the expected slope of 3.6 mT/A. The difference can partly be explained by the stacking of the windings for a thick solenoid. The windings with a larger radius are expected to contribute less to the magnetic field than the windings with a smaller radius, and therefore the slope of magnetic field as a function of solenoid current is lower than expected for a thin solenoid.

GPT simulations

Since GPT is used as the main simulation tool for particle trajectories in both the test beamline and the Smart*Light beamline, it is important that the simulated elements from the setup match with the real elements that will be used. In GPT solenoids can be simulated as a homogeneous solenoid with length and thickness that can produce a static magnetic field. The on-axis field of a solenoid simulated in GPT is given by

$$B(z,r) = \int_{r_1}^{r_2} \int_{z-L/2}^{z+L/2} \frac{\mu_0 I_{tot} r^2}{2(r^2+z^2)^{3/2}} dz dr \tag{5.4}$$

where r_1 is the inner radius of the solenoid, r_2 is the outer radius of the solenoid, L is the length of the solenoid and the total current I_{tot} is given by multiplying the number of windings N with the current I through the solenoid [56]. GPT offers the option to simulate magnetic fields, this allows a comparisson between the measured field profile of the main solenoids and the field profile of these solenoids as simulated in GPT.

The magnetic field of a solenoid is modelled according to the solenoid properties in table 5.3. The current through the solenoid is scanned between 0.5 A and 12.0 A in steps of 0.1 A. The simulation data is compared to the measurements and it is found that a current of 10.1 A in the simulation matches the center-peak field as measured for 10.0 A. In figure 5.7b the simulated on-axis magnetic field profile for a current of 10.1 A and the experimentally measured data points are plotted in one image. The simulated on-axis peak magnetic fields are also plotted as a function of applied current. In figure 5.7c the data points are fitted with a linear fit. The slope of the fit is 3.49 mT/A, which is also lower than the theoretical 3.6 mT/A for a finite thin solenoid. Since GPT also accounts for the thickness of a solenoid, this is as expected.

5.4.2 Steering coil

To correct the position and direction of the beam a steering coil is installed. Steering coils are used to correct the propagation angle and position of the beam. A steering coil set consists of 4 separate solenoids arranged in a square geometry, an artist impression of a steering coil is displayed in figure 5.8. The pairs of opposite coils are connected in series. The current in the horizontal pair of solenoids and the vertical pair of solenoids can be controlled independent of each other, therefore the magnetic fields B_x and B_y can be tuned separately. In the test setup, a steering coil is placed at 23.8 cm from the cathode. The specifications of the steering coil are summarized in table 5.3. In appendix B the results of magnetic field strength measurements of B_x and B_y as a function of current, and magnetic profile measurements of B_x and B_y on the central steering coil axis are displayed.

Table 5.3: Solenoid specifications

	main solenoids exit gun and waist scan	steering coil
number of windings	351	337
length [cm]	6.1	7
inner radius [m]	43.5e-3	
outer radius [m]	68e-3	
maximum current [A]	10	unknown
stacked layers	9 (estimate)	6

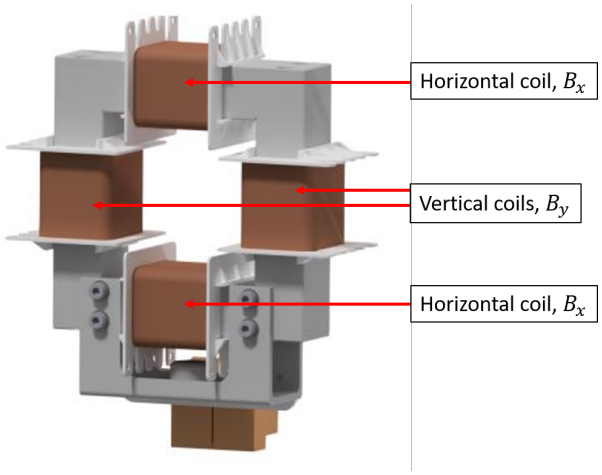

Figure 5.8: An artist impression of a steering coil, the horizontal coils are connected in series and the vertical coils are connected in series [57].

5.5 Diagnostics

A dual diagnostic tool which consists of a Faraday cup and a phosphor-screen was designed for use in both the test setup and the final Smart*Light setup. With this tool, it is possible to measure beam charge and visualize the beam. An image and schematic drawings of the tool are displayed in figure 5.9. A vacuum cross is included in the beamline. The device can be inserted into the beamline by lowering via a height adjustable mechanism. The device is mounted with the Faraday cup on top of the phosphor-screen and is inserted via the top flange of the cross. A window flange is used to close off the bottom flange of the cross, and a camera is mounted on the window flange to be able to visualize the light coming from the phosphor-screen.

5.5.1 Phosphor-screen

Two types of phosphor-screens with different decay times are available. In table 5.4 the properties of the phosphor-screens are summarized. The use of P46 phosphor is preferred since the decay time of this type of phosphor allows the measurement of single bunches at 1 kHz rate. However, if this screen provides insufficient light for the camera to observe the phosphor type can be changed to P43. The signal emitted by the P43 screen will last longer and it is therefore easier to observe on camera, however the signal of two bunches might overlap at 1 kHz bunch rate.

Table 5.4: phosphor-screen specifications [58]

	(25-008) P43 aluminized	(25-008) P46 aluminized
diameter screen	32.7 mm	32.7 mm
material	$GD_2O_2S:Tb^{3+}$	$Y_3AI_5O_12:Ce^{3+}$
color	white	yellow
phosphor thickness	10 - 15 μm	10 - 15 μm
grain size	2 μm	2 μm
decay time	1 ms	300 ns
peak wavelength	545 nm	530 nm

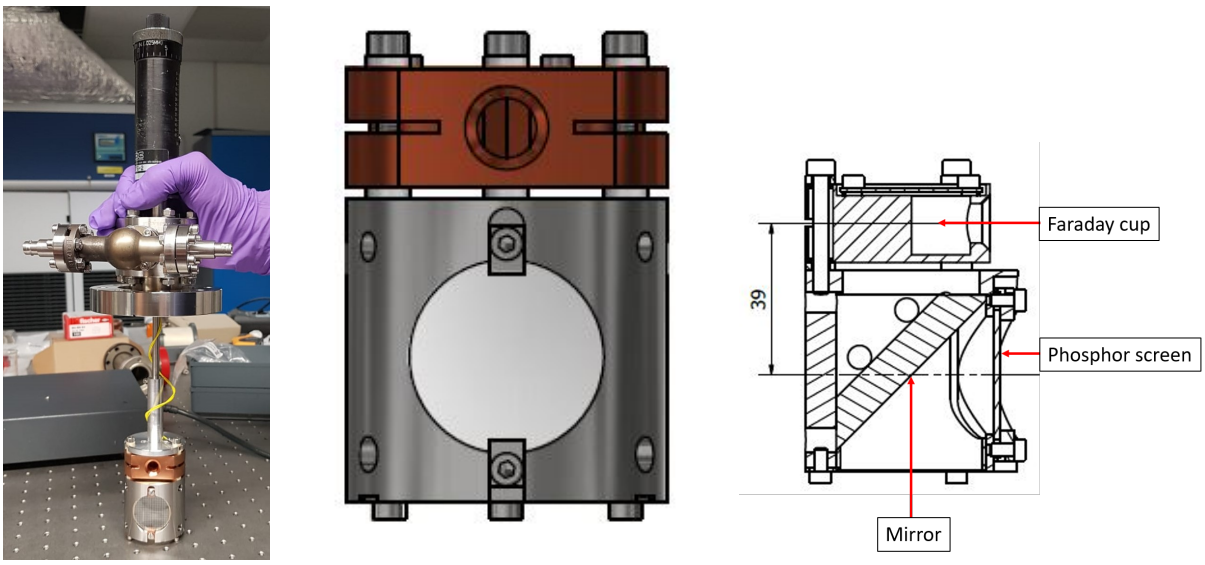

(a) (b) (c)

Figure 5.9: a) An image of the Faraday cup (top) and phosphor-screen holder (bottom) combination attached to a height adjustable suspension. b) Drawing of the front view of the Faraday cup (top) and phosphor-screen holder (bottom) combination. c) cross section of the faraday cup and phosphor-screen holder combination. Behind the phosphor-screen, a mirror with 45° angle w.r.t. the beamline is mounted. This mirror reflects the light towards a camera.

5.5.2 Camera

The phosphor-screen can be lowered into the beamline. However it is not possible to place a camera directly behind the phosphor-screen, this would form an obstruction for the beam when let through to continue the rest of the beamline. To solve this problem the light emitted by the phosphor-screen is reflected by a 45° angle mirror and is coupled out towards the optical table. The lower flange of the vacuum cross is closed with a window flange, the light signal can now be observed by a camera outside of the vacuum beamline.

The camera used in this setup is the FLIR BFS-PGE-31S4M-C. The specifications of the camera can be found in table 5.5. A 25 mm F1.4 Edmund optics lens is used to focus the light of the phosphor-screen on the CCD. To mount the camera in the gap between window flange and optical table, center the camera on the window flange and prevent stray light from reaching the camera a special cover is designed. In figure 5.10 a cross-cut drawing of the cover is displayed. It basically exists of a cylindrical cover which can be placed over the window flange.

Table 5.5: Camera specifications [59]

	BFS-PGE-31S4M-C
resolution	2048×1536
pixel size	3.45 μm
frame rate	35/s

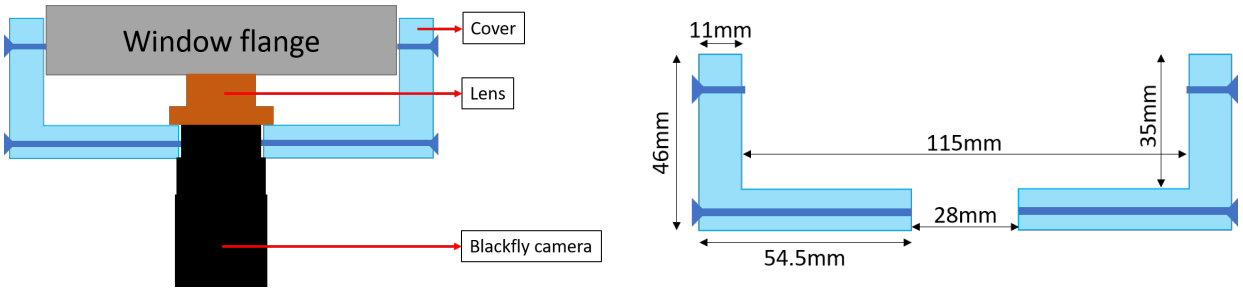

(a) (b)

Figure 5.10: Schematic drawings of the cover used to attach the camera to the window flange of the diagnostics cross. a) a cross cut from the cover cap, camera and lens, b) a cross cut from the cover cap including dimensions.

Calibration

To find the area on the phosphor screen one CCD pixel represents, calibration measurements are performed. A raster with the raster lines separated by 2 mm is printed on a transparent foil. The transparent foil and a glass plate, together of the same optical thickness as the phosphor-screen, are placed inside the phosphor-screen holder. The Faraday cup and phosphor-screen holder are mounted inside the cross. All flanges of the cross are closed and the cross is pumped to a vacuum pressure of the order 10^{-7} mbar. The camera is placed in the cover cap and attached to the window flange.

The camera is focused and the calibration raster is centered by adjusting the camera position. The phosphor-screen holder is lowered to beamline height (1.10 mm on micrometer height adjuster) and an image was saved, see figure 5.11 for an example of a calibration image. For the calibration images, the raster lines indicated with red lines are selected. By comparing the number of pixels between the calibration lines with a measured distance of 28±0.5 mm, the area each pixel represents is calculated. For each image the selection of calibration lines is executed 10 times. The results for four calibration images are taken into account, the horizontal size a pixel represents on the phosphor screen is calculated to be 19.95 μm ± 1.8 % and the vertical size a pixel represents on the phosphor screen is calculated to be 20.03 μm ± 1.8 %. The main contribution in this error comes from the uncertainty in the dimension of the calibration grid, with a high precision grid the quality of the calibration could be improved. In appendix E the matlab script that is used to analyze the calibration images is printed. In appendix F the selected pixel numbers for each of the four calibration images are displayed.

To have a sense of direction on the images of the phosphor screen later on, it is useful to know the camera orientation. The calibration grid is used to align the camera in such a way that the lines are parallel and perpendicular to the sides of the image. This means that the top of the image is above the phosphor screen and the left edge of the image is the on the left side of the phosphor screen (as seen from the gun).

The distortion of the image is checked by comparing the actual distance between four green dots in image 5.11 to the distance as calculated from the pixel size. The TV distortion factor is given by $DTV = \frac{\Delta H}{H} \cdot 100\%$, with H the distance between two of the green dots. The distortion is calculated for all sides of the square formed by the green dots. It can be concluded that the distortion lays within the uncertainty range due to pixel size and uncertainty of actual distance.

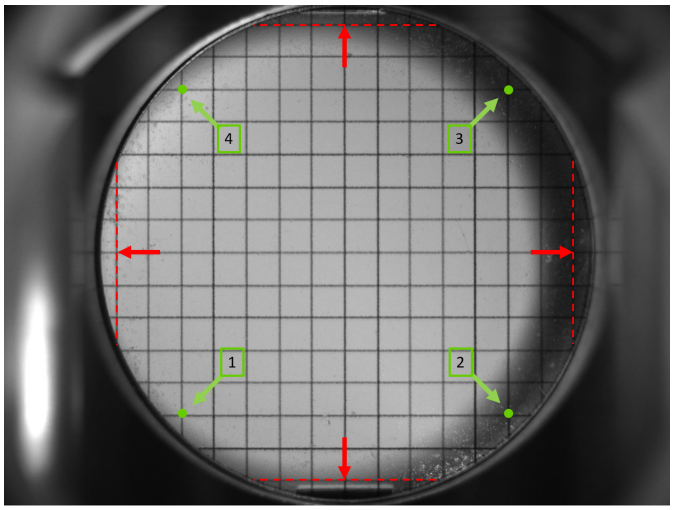

Figure 5.11: Image of the calibration raster made during the calibration process. The lines that are selected for calibration of the pixel size are indicated by the red dotted lines. The green dots indicate the points that are used for the calculation of distortion.

5.5.3 Charge measurements

The effect of space charge on the beam dynamics is highly dependent on the amount of charge per bunch. To be able to understand the beam propagation along the beam line and to match the experimental results to simulations, knowledge of the bunch charge is very important. For this a Faraday cup, a device solely committed to charge measurements, is used. The bunch enters the 1 cm diameter hole in the copper cylinder, and hits the wall. Most electrons are caught by the copper upon collision with the wall, however it is possible to have back scattering or secondary electron emission. The Faraday cup can be connected to the Keithley 616 programmable electrometer. This current measurement device is very sensitive and can measure currents between 10^{-15} A and 10^{-1} A. By measuring the current I coming from the cup, the bunch charge Q_{bunch} and number of electrons $N_{e,bunch}$ can be calculated with

$$Q_{bunch} = N_{e,bunch} \cdot q_e = \frac{I}{\nu_{bunch}} \tag{5.5}$$

where ν_{bunch} is the repetition rate of the gun and q_e is the electron charge.

Since the material of the phosphor-screen is also conducting, it is possible to measure charge by connecting the phosphor-screen to a current meter. The phosphor-screen is not designed to measure charge and the charge measured from the screen is lower than the charge measured with the Faraday cup. There are however two advantages of using the phosphor-screen instead of the Faraday cup to measure charge. When the screen is used to measure charge charge measurements and visualization of the beam can take place at the same time. Furthermore, the Faraday cup has an entrance of only 1cm diameter. This means that the beam has to be smaller in order to have a reliable measurement. The screen does not have such a restriction, it is almost as big as the inner radius of the beam pipe itself.

Ratio between charge on screen and charge in Faraday cup

To be able to use the phosphor-screen for the detection of charge, the relation between the charge measured in the Faraday cup and the charge measured on the phosphor-screen is determined. For three different UV laser beam intensities on the cathode, the charge accumulation in the Faraday cup and on the phosphor screen are measured. Each measurement is repeated three times. The time measured to reach a certain accumulated charge and the known bunch frequency of 10 Hz are used to calculate the average charge per bunch. For each UV laser beam intensity the ratio between the charge measured in the Faraday cup and the charge measured on the phosphor-screen

is calculated. The resulting ratios for all three different UV laser beam intensities on the cathode are displayed in figure 5.12. From the three ratios for the different UV laser beam intensities on the cathode, the average is calculated and the error is propagated. This results in an average ratio of 1.20±12%.

For the determination of bunch charge not only the ratio and the uncertainty of the ratio are of importance. During measurements it was observed that the charge measured on the screen varied with approximately 10% over time. This variation is attributed to instability of the laser pulse energy. Combining the error in the ratio between cup and screen and the error due to variation f bunch charge, results in a total error of 15%.

A remark is that the bunch charges for which the ratio are determined are of limited number and only in the range between 2 and 11 pC on the phosphor-screen. It is not necessarily trivial that this result can be extrapolated to other bunch charges. Nevertheless the ratio of 1.20±12% is used for all experiments discussed in this report.

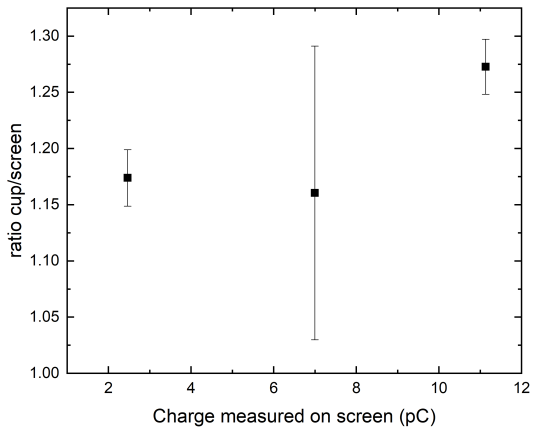

Figure 5.12: The ratio between charge measured in Faraday cup divided by charge measured on phosphor screen measured for different UV laser beam intensities on the cathode. The error bars are the result from the differences in time measured to get to a fixed accumulated charge. Most likely these time differences are caused by fluctuations of UV laser beam intensities during the measurements.

Chapter 6

Experimental results

In section 3.1, the waist-scan method, which can be used to measure the emittance, is explained. During a waist-scan, the beam size on a phosphor screen is measured as a function of focal length of the waist-scan solenoid. Equation 3.3 can be used to determine the emittance. In this chapter, waist-scan results obtained for different bunch charges, gun solenoid currents and UV laser beam profiles on the cathode are presented.

6.1 Waist-scan procedure and analysis

The femtosecond laser system is started and stabilized for approximately half an hour. Then the beam is allowed to continue to the third harmonic generation module. The desired UV laser beam profile on the cathode is obtained by inserting the aperture(s) in the UV laser beam path as described in section 5.3.2. The virtual cathode image is used to check the shape and size of the UV laser beam on the cathode (see image 5.5a and 5.5b). The position of the UV laser beam on the actual cathode can be checked by imaging the cathode on the UV camera (for an example see image 5.3b). The UV laser beam can be centered onto the cathode by slightly adjusting the UV in-coupling mirrors. When the high voltage power supply is turned on to apply a 100 kV voltage to the cathode and the laser beam continues its path to the cathode, bunches are accelerated into the beamline.

A current in the gun solenoid is needed to keep the emittance low and prevent beam loss in the initial phase of acceleration due to beam blowup. To check whether part of the beam is lost, the beam is visualized on the phosphor screen. If the visualized beam has sharp edges, this most likely indicates a cutoff of the beam somewhere along the beamline. Beam cutoff can be caused by a partial hit of the beam with the wall due to deviation of the beam path from the central axis or a blown up beam that hits the wall due to its expanding size. To compensate for deviations in the beam path (schematic drawing in figure 5.1), the steering coil can be used. The steering coil is adjusted in such a way that sharp edges of the beam visualized on the phosphor screen are removed and the electron beam path approximately coincides with the optical axis of the waist-scan solenoid (this is true when the position of the electron beam on the phosphor screen remains constant for changing waist-scan solenoid current). Lastly, it is checked whether the charge measured on the screen remains constant while increasing the gun solenoid current. The total bunch charge is calculated by multiplying the charge measured on the phosphor screen with 1.2 ± 12 %, which is the ratio between Faraday cup and screen as described in section 5.5.3.

A Labview code is used to efficiently control the waist-scan solenoid current and save the images of the electron beam on the phosphor screen recorded during a waist-scan. The start current, the end current, the number of steps in current and the number of images that need to be saved for each current step have to be entered. The delay between two saved images is set to 100 ms, after each current step a longer delay time of 1 s is used in order to allow the system to adjust and stabilize to the new solenoid current .

Fit beam size

To find the beam size of the electron beam on the phosphor screen, the images are fitted with a rotation symmetric Gaussian fit function

$$d = A \cdot \exp(-\frac{(x-x_0)^2 + (y-y_0)^2}{2\sigma_r^2}) + B \tag{6.1}$$

In this equation, d is the number of counts for a pixel, A is the amplitude of the fitted Gaussian, x is the x-position with respect to the offset x_0, y is the y-position with respect to offset y_0, σ_r is the beam size (radius) of the beam on the phosphor screen and B is the offset in counts of the image. The matlab scripts in appendices H.1 and H.2 are used to find the beam size of the beam on the phosphor screen in all images obtained for a waist-scan. For every current step of the waist-scan solenoid 5 images are available. For each current step the average spot size σ_r and the uncertainty in the average spot size are calculated (for calculation of the uncertainty see appendix I).

Fit of beam size over focal length

In Origin, the size of the beam on the phosphor screen is plotted as a function of focal length of the waist-scan solenoid. A user defined fit function based on equation 3.3 is defined. The distance between solenoid and screen l_2 is a constant in the experimental setup and is measured to be 41.0 ± 0.5 cm. The fit function uses the Levenberg-Marquardt iteration algorithm to find the fit parameters ε, σ_v and l_1. Fit parameter ε is normalized according to equation 2.7 in order to get the normalized emittance. The tolerance of the fit is set to $1 \cdot 10^{-9}$. When the variation in the reduced chi-square value between two successive iterations is smaller than the tolerance the fit has converged. For the fit, only the uncertainty in beam size is taken into account, the program does not allow for uncertainties in the independent variable f and constant l_2. Due to the accuracy of the power supply of the the waist-scan solenoid, the relative uncertainty in the focal length f is 1.0%. The distance between the center of the waist-scan solenoid and the screen is measured to be 41.0 ± 0.5 cm. The relative uncertainty in l_2 is calculated to be 1.2%. Due to the complexity of the relation between the different parameters and the fact that the parameters vary during a measurement, the total uncertainty can not easily be calculated. For the waist-scan results presented in this thesis only the uncertainty resulting from the fit is taken into account.

Comparison to GPT result

To validate the experimentally determined emittance, the obtained value is compared to the emittance of the beam as simulated with *General Particle Tracer*. The GPT files in appendices C.1, C.2 and C.3 simulate a beam path similar to the actual setup as described in chapter 5.1. The waist scan fit function 3.3 determines the emittance at the position of the virtual source. However, the derivation of the fit function is based on ideal beam propagation where the emittance is conserved. In reality the emittance is affected by non-conservative forces like space charge and therefore not conserved. The virtual source can be located within the gun solenoid field, therefore it is not convenient to compare the emittance at the virtual source position in the GPT simulation to the measured emittance. Instead it is chosen to compare the GPT simulated emittance at the screen position to the experimental value. To allow the determination of the emittance unaffected by a solenoid field of the waist-scan solenoid, the simulated waist-scan solenoid is switched off.

6.2 Waist-scans for electron beams with bunch charge < 20 pC created with a Gaussian UV laser beam profile on cathode

A Gaussian UV laser beam profile on the cathode with $\sigma = 140$ μm (radius) is used to initiate the electron beam. In theory, this would result in a Gaussian distributed electron beam. The measurement results are compared to GPT simulations of an initial beam with a Gaussian profile with $\sigma = 140$ μm and a cutoff after 3σ. The GPT simulation results are very dependent on the initial bunch size σ. In figure 5.5a the UV beam profile on the virtual cathode is compared to the initial beam profile simulated with GPT.

6.2.1 Example of a single waist-scan for low charge bunches

To gain insight in the different steps of the analyzing process, an example of a result of a single waist-scan is discussed. In this section a waist-scan performed for 0.7 pC ± 15% bunches created with a Gaussian UV laser profile on the cathode and a gun solenoid current of 10.35 is discussed in detail.

Fit of beam size

Throughout the range of waist-scan solenoid currents the images of the beam on the phosphor screen show that the bunches vary in size, shape and intensity. With increasing beam size on the phosphor-screen, the amplitude of the intensity decreases. Since the number of counts for each pixel is discreet, low light intensities can cause issues for low beams with low charge density. The variation of beam size, shape and intensity is illustrated by an image of an under-focused bunch in figure 6.1a, an image of a focused bunch in figure 6.1b and an image of an over-focused bunch in figure 6.1c.

In fit function 6.1 it is assumed that the beam size σ_r in the x- and y-direction are the same. This assumption is made because the fit of a single radius enables the calculation of an emittance for the bunch without accounting for varying beam rotation angles due to the varying solenoid fields. Due to the change of rotation angle during a waist-scan identification of the x- and y-axis of the beam on the phosphor screen is complicated. In reality the beam is not necessarily rotation symmetric. The bunches in this experiment are slightly elongated, this compromises the validity of fit function 6.1, and therefore the final waist-scan result.

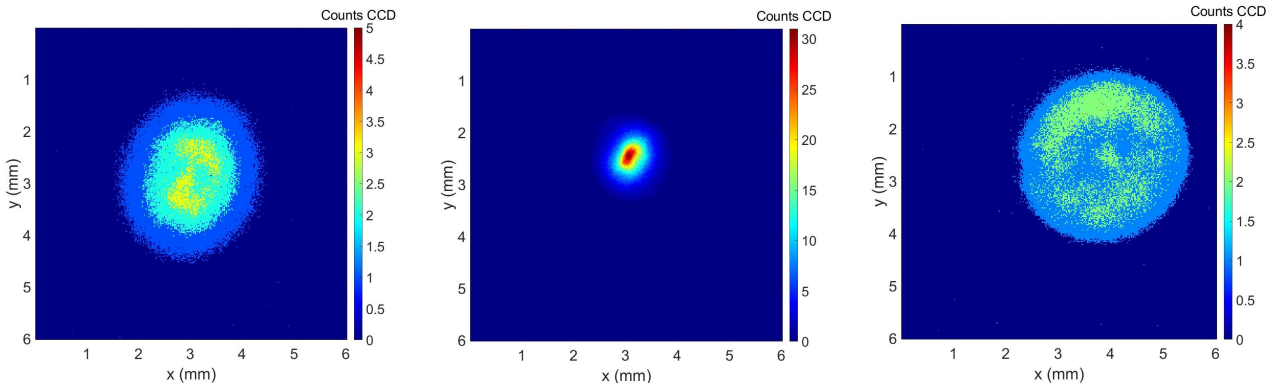

(a) (b) (c)

Figure 6.1: Images of the beam on the phosphor screen recorded for 0.7 pC ± 15%, a gun solenoid current of 10.35 A and a waist-scan solenoid current of a) 3.00 A (under-focused, R-squared=0.896), b) 4.00 A (focused, R-squared=0.959), c) 5.00 A (over-focused, R-squared=0.903). The fit quality of the beam size fit is best in focus.

Fit beam size over focal length

In figure 6.2 the beam sizes of the 0.7 pC bunches are plotted as a function of focal length of the waist-scan solenoid. The error bars in this figure represent the uncertainty in beam size. The fit parameters are summarized in table 6.1. For the fit in figure 6.2 the R-squared value is 0.987.

There are some differences between data and fit that stand out and should be addressed. The measured data shows an oscillation around the fit. An explanation for these oscillations can be a variation in bunch charge. Bunches with higher charge are more difficult to focus than bunches with lower charge. During the measurement, it was already observed that the measured current and the power of the UV laser beam were not stable but varied periodically

with approximately 10%. The fluctuations of UV power were not studied in further detail. From the plot in figure 6.2, the period of the oscillation is determined to be approximately 20.5±3.3 s. Secondly the minimum of the fit is steeper and less broad than the measured beam sizes. It is known that the camera was not saturated in any of the images, however it is possible that the phosphor was saturated. Another potential explanation is space charge effect in the beam focus, which possibly prevents focusing of the beam to a smaller spot. Thirdly it seems that the the data is fitted less accurate for over-focused beams than for under-focused beams. Blow-up of the beam due to space-charge forces in focus can be the cause of the higher increase in beam size on the phosphor screen for over-focused bunches and explain the non-Gaussian profile of the beam in figure 6.1c. If space-charge forces in the focus are the reason for wider minimum and fit quality for over-focused bunches, both effects should become stronger for higher charge bunches.

From figure 6.2 it can be seen that the minimum beam size is found at a focal length of the waist-scan solenoid of approximately 0.26 m. This focal length is smaller than the actual distance between solenoid and screen and this indicates that the virtual source lies on the left side of the waist-scan solenoid and the electron beam that enters the waist-scan solenoid field is divergent.

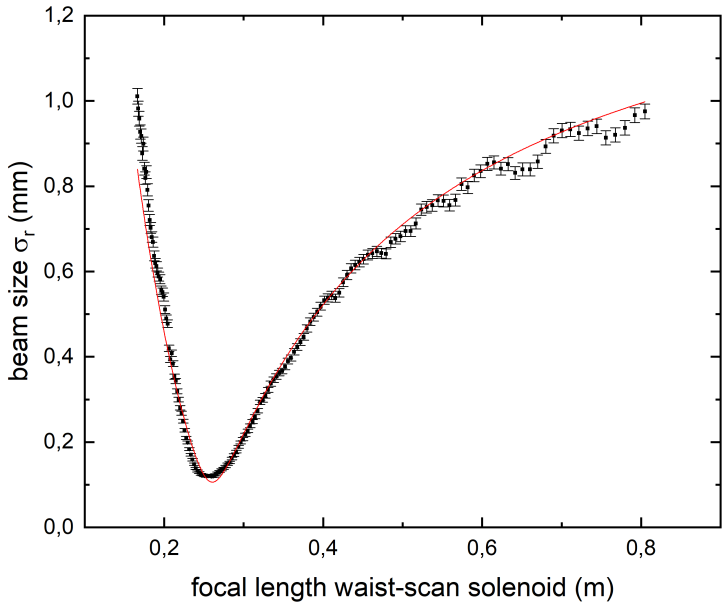

Figure 6.2: Plot of data obtained for a waist-scan of 0.7 pC ± 15% bunches at a gun solenoid current of 10.35 A. The fitted and averaged beam size is plotted over the focal length of the waist-scan solenoid. The experimental data is fitted with equation 3.3, the fit parameters are summarized in table 6.1.

Table 6.1: The fit parameters of the fit of equation 3.3 as displayed in figure 6.2

fit parameter	fit value
ε_n	158 ± 4 nm·rad
l_1	0.689 ± 0.004 m
σ_v	$1.82{\cdot}10^{-4}$ ± $4{\cdot}10^{-6}$ m

6.2.2 0.7 pC bunches, emittance for different gun solenoid currents

To investigate whether there is a gun solenoid current for which there is an optimum (minimum) in emittance, waist scans are performed for gun solenoid currents in the range of 9.65 A (lowest gun solenoid current for which no beam loss was observed) to 10.65 A. The measurement range could have been extended to higher gun solenoid currents since no beam loss was observed for 10.65 A. In figure 6.3 the results of all scans are plotted and fitted, separate figures of each of the waist-scans can be found in appendix J. The fit parameters of each waist-scan are summarized in table 6.2. To indicate the quality of the fit, the adjusted R-squared value is added in the fifth column. Both visual inspection and the adjusted R-squared values confirm the fits and the data points are a good match. The optimum in emittance is measured for a gun solenoid current of 10.35 A. However the differences in emittance measured for different gun solenoid currents are small and GPT simulations did not show much variation. For the 0.7 pC bunches, the effect of gun solenoid current on the emittance is low.

In figure 6.3 a shift in beam size minimum is observed. For increasing gun solenoid current, the focal length of the waist-scan solenoid for which the beam is focused on the phosphor screen decreases and the minimum beam size increases. These values are printed in table 6.3. The beam paths of the beam for different gun solenoid currents and in absence of a waist-scan solenoid are simulated with GPT and displayed in figure 6.4. For increasing gun solenoid current, the size of the beam at the waist-scan solenoid position decreases. In Gaussian optics the size of a waist is related to the incident beam angle, the larger the incident beam angle the smaller the waist. Comparison of figure 6.4 and table 6.3 shows that this relation also holds for the focus of the electron beam.

Table 6.2: Fit parameters that result from fitting equation 3.3 to the waist-scan data sets obtained for 0.7 pC ± 15% bunches and different gun solenoid currents.

current gun solenoid [A]	ε_n GPT [nm·rad]	ε_n fit [nm·rad]	l_1 [cm]	σ_v [m]	adjusted R-squared value
9.65	120	185 ± 6	79.9 ± 0.2	1.30e-4 ± 0.04e-4	0.993
9.75	120	181 ± 6	80.5 ± 0.2	1.37e-4 ± 0.05e-4	0.990
9.85	120	175 ± 6	80.5 ± 0.3	1.45e-4 ± 0.05e-4	0.990
9.95	119	174 ± 6	80.2 ± 0.3	1.55e-4 ± 0.05e-4	0.989
10.05	119	167 ± 5	79.8 ± 0.3	1.59e-4 ± 0.05e-4	0.989
10.15	118	164 ± 5	76.4 ± 0.3	1.68e-4 ± 0.05e-4	0.986
10.25	117	160 ± 4	73.4 ± 0.4	1.75e-4 ± 0.05e-4	0.983
10.35	116	158 ± 4	69.9 ± 0.4	1.82e-4 ± 0.04e-4	0.982
10.45	114	162 ± 3	62.6 ± 0.3	1.91e-4 ± 0.05e-4	0.983
10.55	111	168 ± 3	56.5 ± 0.3	1.99e-4 ± 0.03e-4	0.983
10.65	109	167 ± 2	49.6 ± 0.3	1.97e-4 ± 0.02e-4	0.986

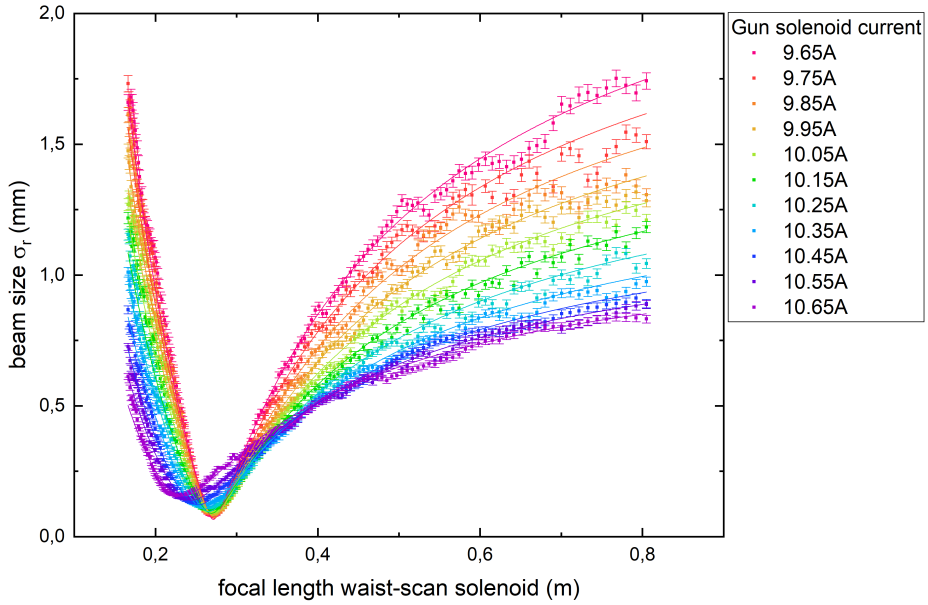

Figure 6.3: The data sets and corresponding fits of the waist-scans performed for 0.7 pC ± 15% bunches with gun solenoid currents between 9.65 A and 10.65 A. The fitting parameters obtained for each of these fits are summarized in table 6.2.

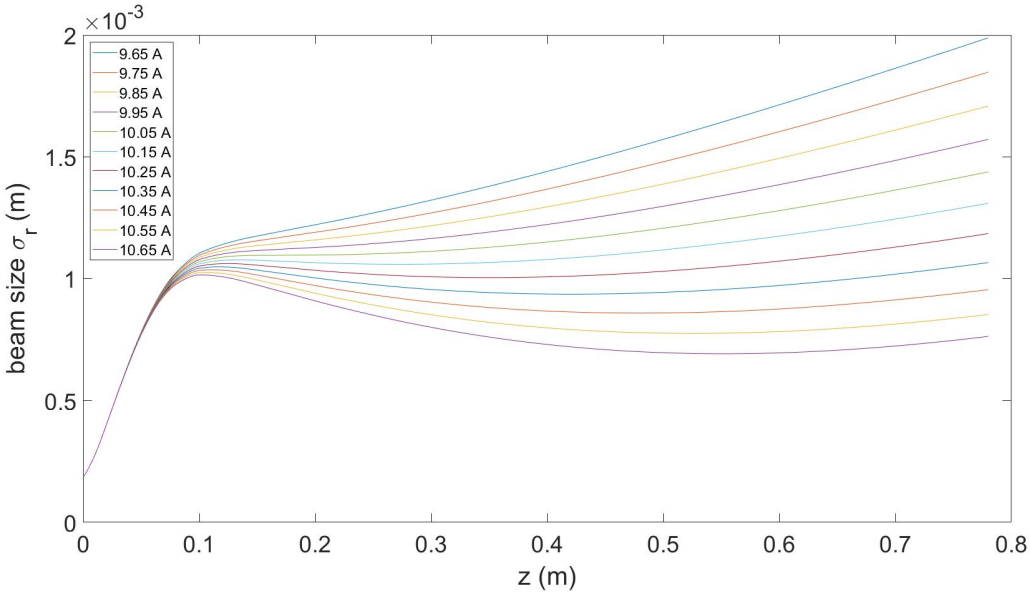

Figure 6.4: The average radius of 0.7 pC bunches over distance in propagation direction for bunches emitted at different gun solenoid currents.

Table 6.3: Characteristics of the waist scan data sets obtained for 0.7 pC ± 15% bunches and different gun solenoid currents.

current gun solenoid [A]	smallest σ_x [m]	f at smallest σ_x [m]
9.65	0.79e-4	0.272
9.75	0.83e-4	0.272
9.85	0.87e-4	0.272
9.95	0.92e-4	0.270
10.05	0.94e-4	0.272
10.15	1.02e-4	0.267
10.25	1.11e-4	0.267
10.35	1.19e-4	0.260
10.45	1.30e-4	0.246
10.55	1.44e-4	0.236
10.65	1.57e-4	0.223

6.2.3 12 pC bunches, emittance for different gun solenoid currents

The aim is to operate the Smart*Light project with bunch charges of approximately 10 pC. A series of scans as a function of the gun solenoid current is performed for bunch charges of 12 pC ± 15%.

Fit of beam size

In figure 6.5 three images of bunches observed for different waist-scan currents are shown. In general, and especially out of focus, the 12 pC bunches have a less Gaussian profile on the screen position. Therefore the fit-quality of the beam size fit is lower compared to the fits of the 0.7 pC bunches. The non-Gaussian profile is most likely caused by the increasing importance of space-charge forces on the beam propagation. For a waist-scan fit the data of the spots near focus is most important. Near focus, the bunch is compressed and shows the best Gaussian like behaviour. Therefore the measurement series are still considered valuable, however larger deviations for the tails of the waist-scan fits are expected.

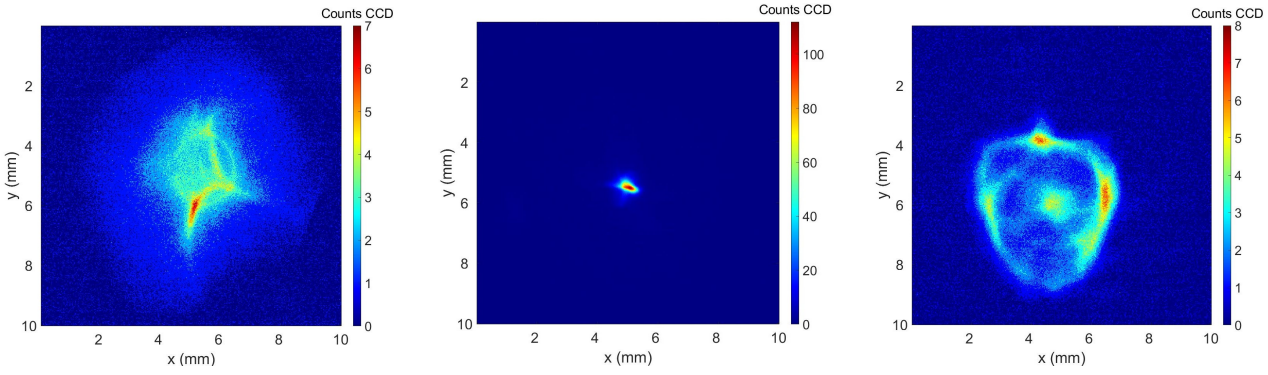

(a) (b) (c)

Figure 6.5: Images of the beam on the phosphor screen recorded for 12 pC ± 15% bunches, a gun solenoid current of 10.44 A and a waist-scan solenoid current of a) 3.10 A (under-focused, R-squared=0.689), b) 4.18 A (focused, R-squared=0.862), c) 4.90 A (over-focused, R-squared=0.547). The fit quality of the beam size fit is as expected from the clear deviation from a Gaussian profile significantly worse than for the low charge 0.7 pC bunches, but still best in focus.

Waist-scan results

The gun solenoid current is varied between 10.15 A and 11.05 A. In appendix K, the four obtained data sets are plotted and fitted. The waist-scan for a gun solenoid current of 11.05 A lacks the characteristic shape of a waist-scan plot due to an insufficient scanning range. Although the data points obtained for 11.05 A can still be fitted it is difficult to determine the quality of the fit, therefore this waist-scan is not taken into account. The fit parameters for the waist-scans are summarized in table 6.4.

Table 6.4: Fit parameters that result from fitting equation 3.3 to the waist-scan data sets obtained for 12 pC ± 15% bunches and different gun solenoid currents.

current gun solenoid [A]	ε_n GPT [nm·rad]	ε_n [nm·rad]	l_1 [cm]	σ_v [m]	adjusted R-squared value
10.15	544	784 ± 64	101.4 ± 0.58	3.22e-4 ± 0.27e-4	0.963
10.44	484	644 ± 31	101.7 ± 0.71	3.81e-4 ± 0.19e-4	0.966
10.75	425	754 ± 12	72.0 ± 0.54	5.23e-4 ± 0.08e-4	0.978

6.3 Waist-scans for electron beams with bunch charge < 20 pC created with a truncated Gaussian UV laser beam profile on cathode

In the thesis of Thijs van Oudheusden [15] it is explained that the emittance of space-charge dominated bunches is conserved for uniformly filled ellipsoidal bunches. It was shown that a concentrically truncated Gaussian beam, which can be produced by focusing of the laser beam on a 2σ diameter pinhole, already shows improved an improvement of bunch quality. In section 5.3.2 the UV laser beam shaping for this experimental setup is shortly discussed. In figure 5.5b the UV laser beam profile of the truncated Gaussian beam is visualized on the virtual cathode, comparison to the truncated Gaussian profile used for the experiments in [15] shows that there the truncated Gaussian profile used in this experiment could be improved. For future experiments it is advised to put more time and effort in the creation of the desired UV laser beam profile on the cathode.

The truncated Gaussian UV laser beam profile used in this experiment was created with a 150 μm pinhole. In figure 5.5b the UV laser beam profile as observed on the virtual cathode is compared to the initial beam profile as simulated with GPT. The initial beam size is determined to approximately be a Gaussian with cutoff at 1.2σ and σ =250 μm. The results of the waist-scan measurements are compared to GPT simulations based on this initial beam profile.

6.3.1 2.1 pC bunches, emittance for different gun solenoid currents

First the behaviour of low-charge bunches created with flat top UV-profile are studied. Waist-scans are performed for bunches with a bunch charge of 2.1 pC ± 15% and gun solenoid currents between 9.50 A and 11.75 A.

In figure 6.6 images of the beam on the screen are shown for three different waist-scan currents. The images show slightly elongated bunches, but their internal structure resembles a Gaussian. As can be seen from the scale of the color bars the intensity of the of light emitted by the phosphor screen that reaches the CCD is low, this seems to reduce the fit quality.

In appendix L plots of the waist-scans are displayed. The fit parameters are summarized in table 6.5. Both from visual examination as from the adjusted R-square value it can be concluded that the fits match the waist-scan data well. However it has to be noted that the measurement ranges for gun solenoid currents 11.25 A, 11.50 A and 11.75 A are limited for small focal length (beam focused before the screen). Therefore it is difficult to assign value to the

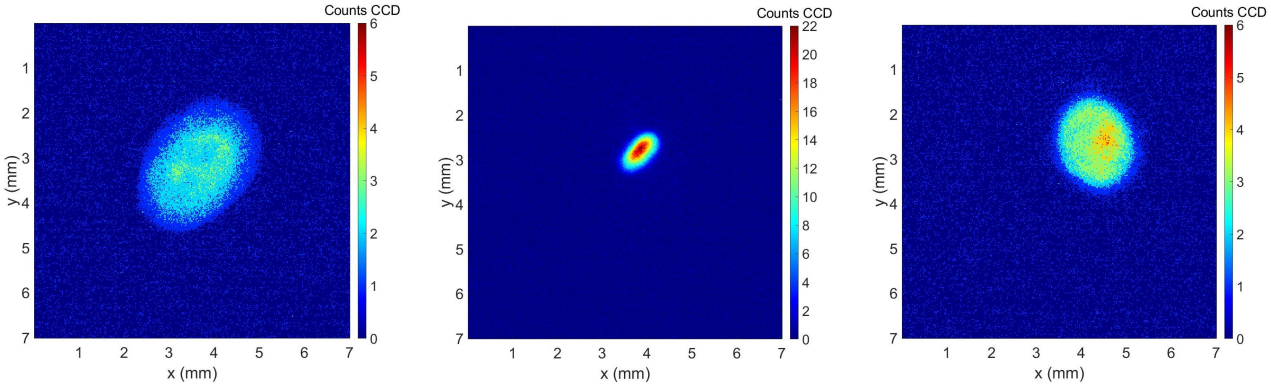

(a) (b) (c)

Figure 6.6: Images of the beam on the phosphor screen recorded for 2.1 pC ± 15% bunches, a gun solenoid current of 10.50 A and a waist-scan solenoid current of a) 3.10 A (under-focused, R-squared=0.240), b) 4.08 A (focused, R-squared=0.651), c) 4.80 A (over-focused, R-squared=0.403). The fit quality of the beam size fit as indicated by the R-squared value does not match the expected high fit quality expected from observation of the spot images and images of the plotted fits. A possible explanation is the low light intensity on the CCD.

fit parameters resulting from these fits. Close comparison of each data set and the corresponding fit again shows that the fit has a sharper minimum than the measured data. The fit does deviate from the actual data for high focal length.

Table 6.5: Fit parameters that result from fitting equation 3.3 to the waist scan data sets obtained for 2.1 pC ± 15% bunches and different gun solenoid currents.

current gun solenoid [A]	ε_n GPT [nm·rad]	ε_n fit [nm·rad]	l_1 [cm]	σ_v [m]	adjusted R-squared value
9.50	185	493 ± 26	78.8 ± 0.2	1.59e-4 ± 0.08e-4	0.990
9.75	172	444 ± 26	81.9 ± 0.3	1.79e-4 ± 0.11e-4	0.980
10.00	162	406 ± 14	85.3 ± 0.3	2.11e-4 ± 0.08e-4	0.987
10.25	152	364 ± 12	86.7 ± 0.4	2.50e-4 ± 0.09e-4	0.981
10.50	145	328 ± 7	80.9 ± 0.5	3.03e-4 ± 0.07e-4	0.979
10.75	141	366 ± 7	62.4 ± 0.5	3.54e-4 ± 0.07e-4	0.978
11.00	143	406 ± 3	32.3 ± 0.2	3.26e-4 ± 0.02e-4	0.989
11.25	148	470 ± 6	18.8 ± 0.2	2.42e-4 ± 0.03e-4	0.987
11.50	145	503 ± 8	18.3 ± 0.1	1.70e-4 ± 0.02e-4	0.993
11.75	154	337 ± 26	21.2 ± 01	0.92e-4 ± 0.07e-4	0.951

6.3.2 5.4 pC bunches, emittance for different gun solenoid currents

The bunch charge of the flat top bunches is increased to 5.4 pC ± 15%. This results in a higher intensity on the CCD which eases the fit of the images of the beam on the phosphor screen. Waist-scans are performed for gun solenoid currents between 9.75 A and 11.50 A. The data sets are plotted and fitted, the figures can be found in appendix M. The fit parameters are printed in table 6.6.

Table 6.6: Fit parameters that result from fitting equation 3.3 to the waist-scan data sets obtained for 5.4 pC ± 15% bunches and different gun solenoid currents.

current gun solenoid [A]	ε_n GPT [nm·rad]	ε_n fit [nm·rad]	l_1 [cm]	σ_v [m]	adjusted R-squared value
9.75	389	654 ± 63	85.4 ± 0.3	1.97e-4 ± 0.19e-4	0.974
10.00	333	630 ± 33	90.7 ± 0.3	2.46e-4 ± 0.13e-4	0.985
10.25	277	542 ± 20	94.6 ± 0.4	2.93e-4 ± 0.11e-4	0.985
10.50	221	508 ± 11	97.7 ± 0.5	3.85e-4 ± 0.09e-4	0.988
10.75	177	473 ± 9	79.5 ± 0.6	4.37e-4 ± 0.09e-4	0.978
11.00	185	567 ± 5	37.5 ± 0.3	4.48e-4 ± 0.04e-4	0.975
11.25	259	654 ± 12	16.7 ± 0.3	3.00e-4 ± 0.05e-4	0.951
11.50	262	864 ± 21	16.5 ± 0.1	2.28e-4 ± 0.05e-4	0.984

6.3.3 15 pC bunches, emittance for different gun solenoid currents

To be able to come to a conclusion on which profile is more beneficial for the creation of low emittance bunches in the charge range of 10 pC waist-scans are performed for 15 pC ± 15% bunches created with a flat top UV laser beam profile on the cathode.

In figure 6.7 three images of bunches observed for different waist-scan currents are shown. The bunches still show non-Gaussian internal structure, especially when out of focus. However when compared to the internal structure in the non-Gaussian profiles observed for the 12 pC ± 15% bunches created with a Gaussian UV laser beam profile on the cathode (see figure 6.5), the internal structure for the bunches created with a truncated Gaussian UV laser beam profile on the cathode seems to be less severe. The bunches are fitted with Gaussian fit function 6.1.

Waist-scans are performed for gun solenoid currents between 10.00 A and 11.50 A. The individual plots of the beam size on the phosphor screen over focal length can be found in appendix N. The scan performed for a gun solenoid current of 10.00 A shows a flattened minimum, this possibly indicates strong repulsive space charge effects in the focal point. Due to the deviating shape of the 10.00 A, the fit parameters for this scan are not considered. In general, the fits seem to match the waist-scan data. Again it is observed that the minimum of the fit is steeper than the measured beam sizes on the phosphor screen. For the waist-scan performed for gun solenoid currents of 10.25 A the fit deviates from the measured beam size for long focal lengths. This was previously seen for 2.1 pC ± 15% and the 5.4 pC ± 15% bunches created with a flat top UV-profile. The waist-scans performed for gun solenoid currents of 11.00 A and 11.25 A show irregularities in spot size. At the time of the measurement there was a lot of activity in the lab. This could have affected the laser stability and therefore the stability of the bunch charge. Nevertheless it is decided to take the fit results in account for the study of emittance development. For the waist-scan performed for a gun solenoid current of 11.50 A visual inspection of the match between fit and data set shows that the fit function does not follow the same trend as the measurement set. This data set is not taken into account. In table 6.7 the fit parameters obtained for the different waist-scans are summarized.

6.4 Waist-scans for electron beams with bunch charge > 20 pC created with a truncated Gaussian UV laser beam profile on cathode

With the current electron gun, bunches with bunch charges up to 50 pC can be produced. For the Smart*Light project, it can be interesting to investigate the use of higher charge bunch charges since a higher number of electrons could potentially result in a higher number of produced x-ray photons. In the measurements performed on the low and medium charge bunches (< 20 pC), it was observed that bunches with a bunch charge of 10 pC already suffer from deviations of the bunch profile due to space-charge forces. The validity of waist-scans performed on bunches with a bunch charge between 10 pC and 20 pC still results in a potentially valuable rough estimate of the beam

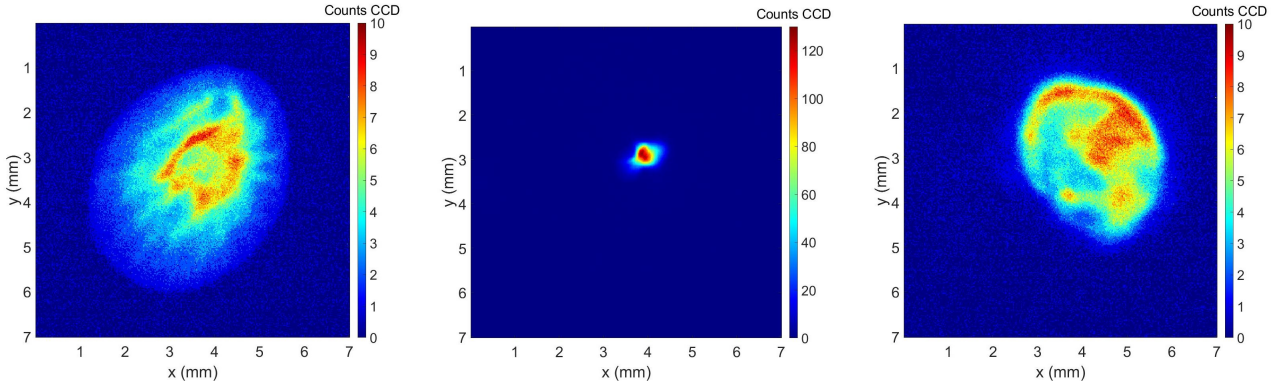

(a) (b) (c)

Figure 6.7: Images of the beam on the phosphor screen recorded for 15 pC ± 15% bunches, a gun solenoid current of 10.50 A, and a waist-scan solenoid current of a) 3.40 A (under-focused, R-squared=0.792), b) 4.10 A (focused, R-squared=0.935), c) 4.60 A (over-focused, R-squared=0.741). Although observation of the spot images shows clear deviation from a Gaussian beam profile, the R-squared values indicate that the beam size fit does still give a good indication of the beam size on the phosphor screen.

Table 6.7: Fit parameters that result from fitting equation 3.3 to the waist-scan data sets obtained for 15 pC ± 15% bunches and different gun solenoid currents.

current gun solenoid [A]	ε_n GPT [nm·rad]	ε_n fit [nm·rad]	l_1 [cm]	σ_v [m]	adjusted R-squared value
10.25	820	787 ± 45	109.0 ± 0.4	2.93e-4 ± 0.11e-4	0.974
10.50	575	705 ± 18	110.4 ± 0.5	3.85e-4 ± 0.09e-4	0.983
10.75	351	725 ± 6	88.2 ± 0.6	4.37e-4 ± 0.09e-4	0.990
11.00	471	1185 ± 31	29.3 ± 0.3	4.48e-4 ± 0.04e-4	0.898
11.25	818	1101 ± 40	9.9 ± 0.3	3.00e-4 ± 0.05e-4	0.713

quality. Increase of the charge does however further compromise the use of the waist-scan method. To study whether valuable information can still be obtained for high charge bunches, measurements are performed for 30 pC and 47 pC bunches.

6.4.1 30 pC bunches, emittance for different gun solenoid currents

To investigate whether it might be possible to increase the bunch charge in the Smart*Light project waist-scans are performed for 30 pC ± 15% bunches. Since space charge effects are of increasing influence on the beam propagation, first the shape of the bunches and structure within the bunch are visualized. In figure 6.8 three images are displayed each recorded for a different focusing strength of the waist-scan solenoid. The under-focused beam clearly has a non-Gaussian profile, and the over-focused beam shows a high intensity center and a wide low intensity tail. The expansion of over-focused bunches seems to stagnate for increasing focal strength. In figure 6.9a the beam size does not increase for focal lengths smaller than 0.10 m. The peak of the waist-scan fit is shifted to a low focal length and visual validation shows a bad match between data and fit. When the data for focal lengths smaller than 0.10 m is not taken into account the fit quality improves, this can be seen in figure 6.9b. In appendix O, the waist-scan data sets are plotted and fitted. In table 6.8 the fit parameters that result from the fit are summarized.

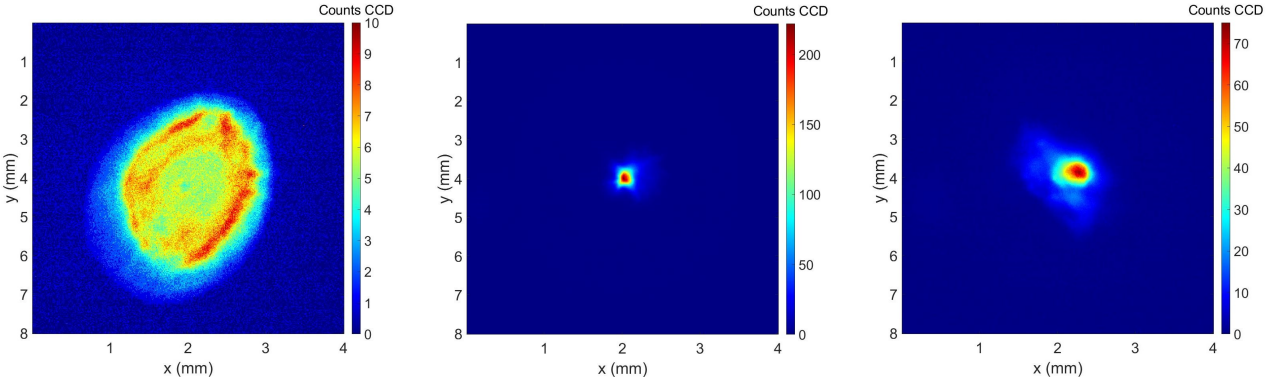

(a) (b) (c)

Figure 6.8: Images of the beam on the phosphor screen recorded for 30 pC ± 15% bunches, a gun solenoid current of 10.50 A and a waist-scan solenoid current of a) 3.50 A (under-focused, R-squared=0.785), b) 4.16 A (focused, R-squared=0.928), c) 4.40 A (over-focused, R-squared=0.830).From the images it can be concluded that the beam does not behave as expected from a Gaussian beam going through the focus. The R-squared values are still relatively high compared to R-squared values obtained for the beam size fits of the lower charged bunches. Nevertheless, the observation that the beam behaves different than expected still greatly reduces the reliability of this measurement.

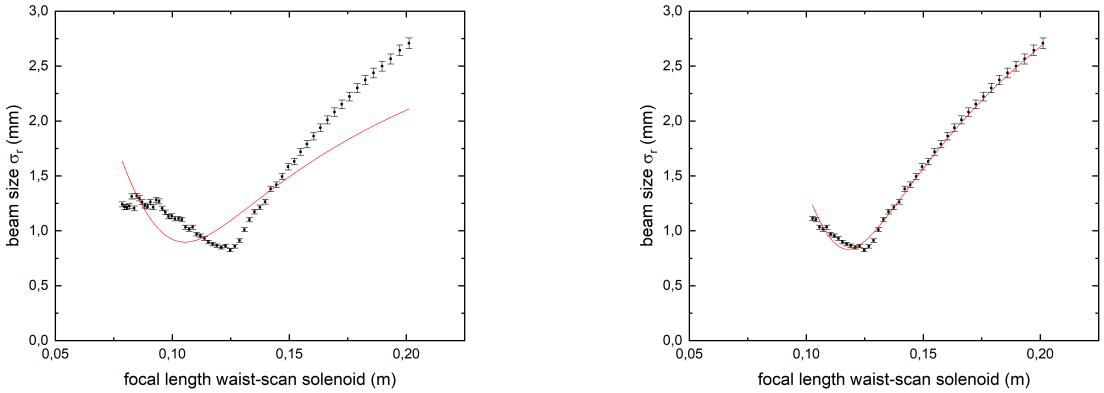

(a) (b)

Figure 6.9: Waist-scan measurement of 30 pC bunches created with a flat top UV-profile and a gun solenoid current of 11.50 A. The waist-scan data is fitted with fit function 3.3. a) waist-scan fit where the entire range of measured beam sizes on the phosphor screen is taken into account, b) waist-scan fit for which the beams fitted with beam size smaller than expected are not taken into account.

Table 6.8: Fit parameters that result from fitting equation 3.3 to the waist-scan data sets obtained for 30 pC ± 15% bunches and different gun solenoid currents.

current gun solenoid [A]	ε_n GPT [nm·rad]	ε_n fit [nm·rad]	l_1 [cm]	σ_v [m]	adjusted R-squared value
10.25	1539	1005 ± 83	95.2 ± 0.5	3.28e-4 ± 0.29e-4	0.952
10.50	1229	853 ± 49	95.1 ± 0.7	3.71e-4 ± 0.23e-4	0.953
10.75	1107	1084 ± 34	85.0 ± 0.8	5.76e-4 ± 0.19e-4	0.929
11.00	1524	2214 ± 26	44.1 ± 0.6	9.87e-4 ± 0.08e-4	0.967
11.25	1829	1762 ± 11	12.2 ± 0.1	4.64e-4 ± 0.01e-4	0.992
11.50	1522	2120 ± 51	15.3 ± 0.1	3.18e-4 ± 0.07e-4	0.946

6.4.2 47 pC bunches, emittance for different gun solenoid currents

The maximum bunch charge that could be achieved for this setup is 47 pC ± 15%. In figure 6.10 three images of bunches focused with increasing focal strength are displayed. The focusing of the bunches is different than seen for the other bunch charges. In focus (6.10b) the bunch is not as small and still has structure. The validity of a Gaussian fit for this image of the beam on the phosphor screen is questionable. This compromises the further waist-scan analysis.

Waist-scan measurements are performed for gun solenoid currents between 10.25A to 11.50 A. Plots of the obtained data can be found in appendix P and show clear deviation from the characteristic waist-scan shape. As can be seen in figure 6.11a, the minimum in beam size on the phosphor screen as a function of focal length is flattened. This effect was observed previously in the waist-scan for 15 pC bunches and a gun solenoid current smaller than 10.25 A. However, the effect now seems to be visible for gun solenoid currents up to 11.00 A. The flattening of the minimum, at a larger beam size than the expected minimum can most possibly be attributed to space charge forces. The beam size at which the curve is flattened is not constant, but seems to increase for an increasing gun solenoid current. Because of the non-consistent shape between measurement set and fit, the results of the waist-scan for currents from 10.25 A to 11.00 A are not considered for the determination of the beam emittance. In table 6.9 the fit parameters obtained for the fits of 11.25 A and 11.50 A are summarized. The fit of the waist-scan performed for a solenoid current of 11.25 A shows the best match to the data obtained from the measurement, the plot and figure are displayed in figure 6.11.

Table 6.9: Fit parameters that result from fitting equation 3.3 to the waist-scan data sets obtained for 47 pC ± 15% bunches and different gun solenoid currents.

current gun solenoid [A]	ε_n fit [nm·rad]	l_1 [nm·rad]	σ_v [cm]	adjusted [m]	ε_n GPT R-squared value
11.25	2304	2201 ± 44	15.1 ± 0.2	3.36e-4 ± 0.05e-4	0.910
11.50	1964	2142 ± 79	16.8 ± 0.1	3.27e-4 ± 0.12e-4	0.897

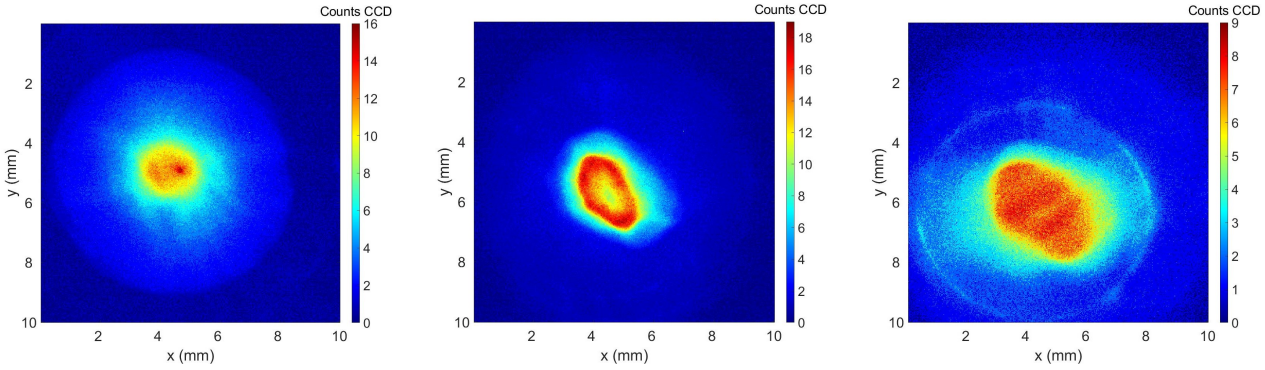

(a) (b) (c)

Figure 6.10: Images of the beam on the phosphor screen recorded for 47 pC ± 15% bunches, a gun solenoid current of 11.25 A, and a waist-scan solenoid current of a) 5.00 A (under-focused, R-squared=0.856), b) 6.65 A (focused, R-squared=0.836), c) 7.40 A (over-focused, R-squared=0.822). From the images it can be concluded that the beam does not behave as expected from a Gaussian beam going through the focus. The R-squared values are still relatively high compared to R-squared values obtained for the beam size fits of the lower charged bunches. Nevertheless, the observation that the beam behaves different than expected still greatly reduces the reliability of this measurement.

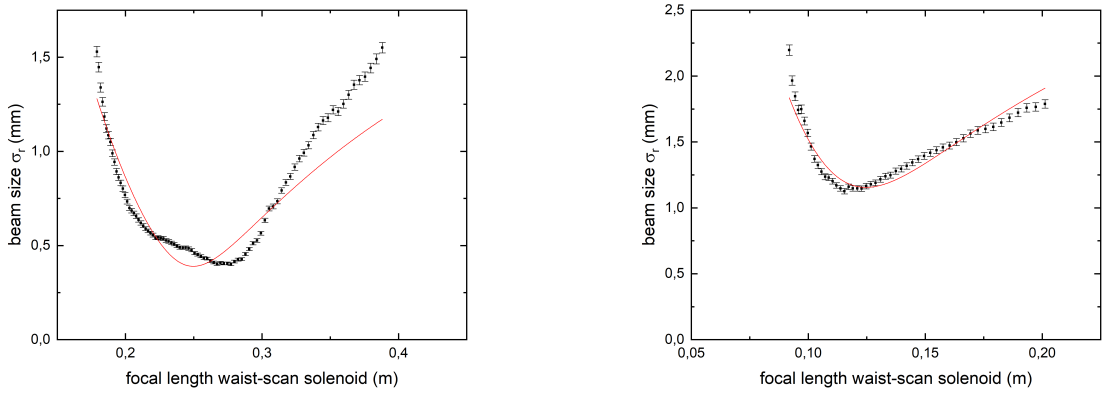

(a) (b)

Figure 6.11: a) Waist-scan measurement of 47 pC bunches created with a flat top UV-profile and a gun solenoid current of 10.75 A. The waist-scan data is fitted with fit function 3.3. The minimum in beam size on the phosphor screen is flattened. b)Waist-scan measurement of 47 pC bunches created with a flat top UV-profile and a gun solenoid current of 11.25 A. The waist-scan performed for this gun solenoid current shows the best match between fit and measurement.

6.5 Discussion

The results of the individual waist-scans are summarized and discussed. However, apart from pointing out irregularities during the measurements and in the obtained data sets, the validity and meaning of the results and the appropriateness of the use of the waist-scan method are not discussed in detail. In this section, the reliability of the results and the waist-scan method are discussed. Special attention is given to the effect of increasing charge on the analysis. Furthermore the relation between the experimental results and the GPT simulation results as presented in the tables containing the fit parameters of each experiment will be considered.

6.5.1 Fit of the beam size

The fit function used to determine the size of the beam on the phosphor screen is a rotation symmetric Gaussian. Observation of the different beams on the phosphor screen often showed slight elongation of the beam. The change in solenoid field during a waist-scan does however cause the beam rotation to be different for each waist-scan solenoid current step. This complicates the identification of the x- and y-direction of the beam in the images. Therefore it is opted to use a rotation symmetric fit function and calculate a direction independent beam emittance. The measurement can be improved by replacing the solenoid with a quadrupole. A quadrupole field focuses a beam independently in x- and y- direction, and causes no beam rotation. This allows identification of the x- and y-direction of the beam in the images, an therefore the use of the 2D rotated Gaussian fit function for beam size determination.

For very low bunch charge and a Gaussian UV laser beam profile on the cathode, the beam profile resembles a Gaussian relatively well. Nevertheless the beam-profile of over-focused bunches already starts to show deviations from the ideal Gaussian beam profile. Since space-charge forces are strongest in the focal point, this indicates space-charge forces already compromise the beam propagation of the very low charge 0.7 pC bunches. Increase of bunch charge to 12 pC already visibly causes the beam profile to deviate from a Gaussian and internal structure is starting to form over the entire focusing range. In an attempt to prevent bunch deterioration due to space-charge effects the UV laser beaM profile on the cathode is changed from Gaussian to a truncated Gaussian. Waist-scans are again performed for low charge bunches, and the bunch profile on the screen seems to be improved slightly. However, for a medium bunch charge of 15 pC internal structure again starts to dominate the beam profile. In future experiments, more effort should be made to create an UV laser beam with a clear truncated Gaussian profile (truncated at radius waist 1σ) and comparative measurements between the Gaussian and the truncated Gaussian UV laser beam profiles should be executed for bunches with equal charge.

Non-Gaussian internal bunch structure not only compromises the method of beam size determination but also indicates possible emittance growth along the beamline. When the trace space projection of a beam deviates from an ellipsoid, drift sections and solenoid field rotations cause the area occupied in phase-space to grow. This process is called beam filamentation. In figure 6.12 the filamentation process is visualized. The initial beam distribution in figure 6.12a is not an ideal ellipsoid and the drift section causes the beam to fill the larger beam area of figure 6.12b. The non-Gaussian spatial distribution observed for bunches (especially with high bunch charge) results in a non-Gaussian spatial distribution and therefore a deviation from the ideal ellipsoidal phase-space projection. Therefore filamentation and emittance growth is likely to take place.

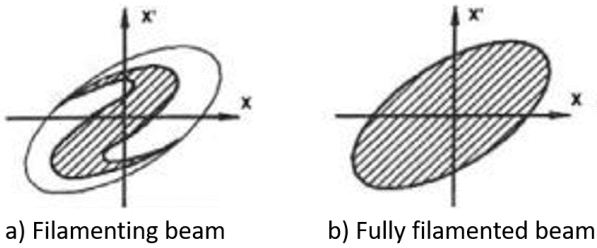

Figure 6.12: Schematic drawings of the beam filamentation process [24]. In a) it can be seen that the trace-space projection is not an ellipsoid, drift of the beam causes the beam to occupy a larger area in trace-space as can be seen in b).

6.5.2 Waist-scan fit

For each waist-scan, the fitted beam beam size on the phosphor screen is plotted over the focal length of the waist-scan solenoid. The emittance of the beam is determined by fitting the data points with the waist-scan fit function. During the discussion of the results it has to be kept in mind that the fit function is derived under the assumptions that the beam is a conservative system, is not subjected to space-charge forces, and has a Gaussian trace-space profile. This is only partially true, and with increasing bunch charge these assumptions become less valid.

For low charge bunches (< 10 pC), both the data obtained with a Gaussian and a truncated Gaussian UV laser beam profile shows the expected characteristic waist-scan shape, and the fit-quality of the waist-scan fit to the data is generally high. Nevertheless when the fitted emittance is compared to emittance obtained from GPT simulations, differences between measurements and simulations are observed. The outcome of the simulations is very sensitive to the initial beam size. For the bunches created with a Gaussian UV laser beam profile on the cathode the difference between simulation and experimental result can possibly be explained by a difference between simulated initial beam size and actual size of the UV laser beam on the cathode. For the bunches created with the truncated Gaussian UV laser beam profile, a mismatch in initial beam size can not be the only reason of the mismatch which is more than a factor 2 for all scans (both for 2.1 pC and 5.4 pC). This indicates that the waist-scan method might not be valid for electron bunches with non-Gaussian initial profiles.

For medium bunch charges (between 10 pC and 20 pC), deviations of the characteristic waist-scan shape are first observed. For low gun solenoid currents, the minimum in spot size as a function of focal length is flattened. It is known that the CCD was not saturated. Calculation of the charge density in the flattened minima does not show a saturation of charge density at one single value. This indicates that the phosphor was also not saturated. The most likely explanation is that space-charge forces prevent the beam from focusing to a smaller spot. Comparison of the measured emittance to the GPT simulated emittance shows that the measurement and simulation result in emittances of the same order, but the GPT emittance is more sensitive to the gun solenoid current and has a lower minimum.

Further increase of the bunch charge (> 20 pC) shows a quick fall in reliability of the results. Not only the beam profile on the phosphor screen is not Gaussian, but also the beam size on the phosphor screen plotted as a function of focal length starts to significantly deviate from the characteristic waist-scan shape. The flattening of the minimum is observed for higher gun solenoid currents, and especially the expansion of over-focused bunches is not related to the focal length in the way expected according to the waist-scan fit function. For 47 pC, the maximum bunch charge that can be reached for the current setup, focusing of the bunches proved to be difficult.

Optimum gun solenoid current

Waist-scans were performed for different gun solenoid currents, the aim was to find a gun solenoid current where the emittance is minimal. For low bunch charges, both the measured emittance and the simulated emittance do not vary much. For higher bunch charges, the gun solenoid currents does start to affect the beam quality more. Since it also becomes more difficult to control the blowup of the beam, this behaviour is as expected. Unfortunately the measurement results for higher bunch charge also become less reliable. Therefore it is difficult to say whether the minima found from the measurements are really found for the optimum gun solenoid currents. In table 6.10 the gun solenoid currents for which the waist-scan showed the lowest emittance are summarized.

Table 6.10: List of the gun solenoid currents for which the lowest emittances were measured for each series of waist-scans.

bunch charge [pC]	UV profile	gun solenoid current [A]	emittance from waist-scan [nm·rad]
0.7 ± 15%	Gaussian	10.35	158 ± 4
12 ± 15%	Gaussian	10.44	644 ± 31
2.1 ± 15%	flat-top	10.50	328 ± 7
5.4 ± 15%	flat-top	10.75	473 ± 9
15 ± 15%	flat-top	10.50	705 ± 18
30 ± 15%	flat-top	10.50	853 ± 49

6.5.3 Validity waist-scan technique

During the derivation of the waist-scan fit function many assumptions regarding the beam shape and beam behaviour are made. The system is assumed to be conservative, and this means the space-charge forces should not affect the beam dynamics and there should be no emittance growth between virtual source and screen. Furthermore it is assumed that the beam has a Gaussian distribution in phase-space. To be able to fit the beam size on the screen this assumption is taken even further, and it is assumed the beam has a rotation symmetric Gaussian profile on the screen. The result of these assumptions is that the waist-scan is only reliable for very low charge rotation symmetric beams.

To improve the validity of the waist-scan technique, the solenoid could be replaced by a quadrupole. After this modification, the requirement of a rotation symmetric beam is not necessary.

In the series of scans performed in this thesis it was observed that space-charge forces already become important for bunch charges higher than 10 pC. Beneath 20 pC the waist-scans might still provide a rough estimate of the emittance, but for higher bunch charges the behaviour of the beam deviates strongly from the the expected behaviour of a beam during a waist-scan measurement. Therefore it is not advised to use the waist-scan method for beams with bunch charges higher than 20 pC.

Chapter 7

Conclusion

The aim of Smart*Light is to produce a new type of x-ray source based on inverse Compton scattering of laser photons on relativistic electrons. For this application, it is important that both the laser beam and the electron beam are of high quality. High intensity beams improve the scattering probability, and the quality of the beams affects the quality of the produced x-ray beam. To check whether the electron beam quality of electron beams produced by the 100 kV DC photo electron gun aimed for the Smart*Light project is sufficient, measurements of the electron beam quality are performed. In this thesis, waist-scans are used to measure the emittance of electron beams created with different UV laser beam profiles on the cathode and different bunch charges. Since the gun solenoid can be used to counteract emittance growth, it is also tried to find an optimum in gun solenoid current for which the beam quality of the propagating beam is maximized.

The waist-scan measurement technique is based on a number of assumptions. Violation of these assumption can seriously affect the validity of the waist-scan results. To determine the beam size of the beam on the phosphor screen, a rotation symmetric Gaussian fit function is used. Since this fit function determines a single beam size, the beam rotation due to the waist-scan solenoid field can be ignored. However measurements have shown that the beam is often slightly elongated, and therefore not rotation symmetric. It is suggested to replace the waist-scan solenoid by a quadrupole. Since quadrupoles cause no beam rotation, a 2D rotated Gaussian fit function can be used to determine the beam size, and therefore also the emittance ε_x and ε_y, in two independent directions.

To be able to derive the waist-scan fit function the waist-scan setup is assumed to be a conservative system. This means that the effect of space-charge forces on the beam propagation is not considered, and that the emittance is assumed to be conserved between the virtual source and the screen. The derivation of the waist-scan fit function is based on the propagation of a Gaussian beam through the waist-scan setup, and the fit function used to determine the beam size assumes the beam to have a Gaussian profile on the phosphor screen. Waist-scan measurements were performed for beams with different bunch charges. For very low bunch charges, space-charge forces do not seem to affect the beam profile on the screen. This indicates that it can be assumed that space-charge effects only have minor influence on the beam propagation, and the assumptions made for both derivation of the waist-scan fit function and the fitting of the beam size on the screen are valid. For higher bunch charges (over 10 pC), images of the beam show clear deviations from a Gaussian profile. This indicates that space-charge forces do affect the beam propagation, and the waist-scan results are already compromised. Nevertheless, the shape of the characteristic waist-scan relation is still as expected, so the results of the waist-scans might still give a rough estimate of the emittance. For 12 pC $\pm$ 15% bunches created with a Gaussian initial beam profile, an emittance of 644 nm·rad was measured. This is of the same order as expected from GPT simulations, and therefore indicates a beam quality as expected. Increase of bunch charge amplifies the effects, and deviations of the characteristic waist-scan relation between focal length and beam size on the phosphor screen are observed. The assumptions made to derive the waist-scan fit function are violated toO much to make the results representative for the actual situation.

In an attempt to prevent emittance growth due to space-charge forces, the UV laser beam profile which is used to form the initial electron beam is changed from Gaussian to a Gaussian truncated at 1.2σ. The more uniform distribution of this beam should minimize the effect of the space-charge forces. However, a non-Gaussian distribution compromises the assumption of Gaussian beam propagation and the use of a Gaussian fit function to determine the beam size on the phosphor screen. Although the shape of the characteristic waist-scan relation is as expected, the resulting emittance deviates strongly from the emittance simulated in GPT. For future experiments, more effort should be put in the creation of a clear truncated profile at 1σ and it is advised to perform comparative measurements of for bunches of equal charge but different initial beam profile.

For each bunch charge, it is tried to find the optimum gun solenoid current for which the emittance is minimal. Although a relation between gun-solenoid current and emittance was observed, the reliability of the waist-scan measurements for higher charged bunches and bunches created with a non-Gaussian UV laser profile has to be considered. Simulations showed the minimum emittances were observed for beams approximately parallel after the gun solenoid, this is as expected.

In short it can be concluded that the waist-scan method is only applicable for low charge, rotation symmetric, Gaussian beams. Deviations from these conditions compromise the validity of the waist-scan technique. Since the beams interesting for Smart*Light (bunch charge $>$ 10 pC) are already partly affected by space-charge effects, the waist-scan technique is not a very reliable method for emittance determination. It is advised to implement a pepper-pot in order to get a more reliable emittance measurement for higher charge bunches. Comparison of waist-scan measurements and pepper-pot measurements can also be used to come to a more definite conclusion of the effect of space-charge on the outcome of a waist-scan measurement.

7.1 Future Outlook

A measurement method that has much potential for precise emittance measurements is the pepper-pot method. Although this method was not implemented due to time related issues, the potential of this measurement method for the Smart*Light setup is investigated. Advantages of the pepper-pot method over the waist-scan method are that use of the pepper-pot filters out a large portion of the space-charge effects and that the pepper-pot method can be used to obtain a position dependent profile of the emittance. Although the pepper-pot is not used in the test-setup, it might be possible to implement one in the actual Smart*Light beamline. The design of a pepper-pot setup for the Smart*Light setup is restricted by the spatial possibilities. In chapter 4, two potential designs are presented. Note that pepper-pot designs are dependent on the intended bunch charge. Both presented options are designed for 10 pC bunches. For higher bunch charges it might be necessary to decrease the hole size and increase the hole spacing in order to keep the beamlets in the emittance dominated regime and prevent overlap.

The work presented in this thesis focused on measurements of the quality of electron beams produced by the 100 kV DC photo electron gun that will be used in the Smart*Light setup. Although the waist-scan measurements only resulted in a rough estimate of the emittance for 10 pC bunches, this rough estimate indicates that the beam quality was of the same order as expected from simulations. This allows for continuation of the project. The gun can be moved to the Smart*Light setup and other elements can be installed and tested.

Bibliography

[1] Rade R Babić, Stanković Gordana Babić, Strahinja R Babić, and Nevena R Babić. 120 years since the discovery of x-rays. *Medicinski pregled*, 69(9-10):323–330, 2016.

[2] Soft x-rays - hard x-rays.

[3] Allahyar Kangarlu and Pierre-Marie L Robitaille. Biological effects and health implications in magnetic resonance imaging. *Concepts in Magnetic Resonance: An Educational Journal*, 12(5):321–359, 2000.

[4] Oscar E Hemberg, Mikael Otendal, and Hans M Hertz. Liquid-metal-jet anode x-ray tube. *Optical Engineering*, 43(7):1682–1688, 2004.

[5] Australian Radiation Protection and Nuclear Safety Agency. X-rays, May 2019.

[6] File:esrf grenoble.jpg.

[7] Akiko Hokura and Emiko Harada. *Synchrotron Radiation X-Ray Analysis of Metal-Accumulating Plants*, pages 125–145. Springer Japan, Tokyo, 2017.

[8] A Snigirev, I Snigireva, V Kohn, S Kuznetsov, and I Schelokov. On the possibilities of x-ray phase contrast microimaging by coherent high-energy synchrotron radiation. *Review of scientific instruments*, 66(12):5486–5492, 1995.

[9] Stephanie Kulpe, Martin Dierolf, Eva Braig, Benedikt Günther, Klaus Achterhold, Bernhard Gleich, Julia Herzen, Ernst Rummeny, Franz Pfeiffer, and Daniela Pfeiffer. K-edge subtraction imaging for coronary angiography with a compact synchrotron x-ray source. *PLoS One*, 13(12):e0208446, 2018.

[10] Stephanie Kulpe, Martin Dierolf, Benedikt Günther, Madleen Busse, Klaus Achterhold, Bernhard Gleich, Julia Herzen, Ernst Rummeny, Franz Pfeiffer, and Daniela Pfeiffer. K-edge subtraction computed tomography with a compact synchrotron x-ray source. *Scientific reports*, 9(1):1–8, 2019.

[11] William Thomlinson, Hélène Elleaume, L Porra, and P Suortti. K-edge subtraction synchrotron x-ray imaging in bio-medical research. *Physica Medica*, 49:58–76, 2018.

[12] FA Dilmanian, XY Wu, EC Parsons, B Ren, J Kress, TM Button, LD Chapman, JA Coderre, F Giron, D Greenberg, et al. Single-and dual-energy ct with monochromatic synchrotron x-rays. *Physics in Medicine & Biology*, 42(2):371, 1997.

[13] Martin Reiser and Patrick O'Shea. *Theory and design of charged particle beams*, volume 312. Wiley Online Library, 1994.

[14] BRUCE M Dunham. Dc/rf injectors. *Photoinjectors-An Engineering Guide, Ed.: T. Rao, D. Dowell, to be published by Bentham Scientific Publishers.*

[15] Thijs van Oudheusden. *Electron source for sub-relativistic single-shot femtosecond diffraction*. PhD thesis, Ph. D. thesis, Eindhoven University of Technology, 2010.

[16] PLEM Pasmans, DC Van Vugt, JP Van Lieshout, GJH Brussaard, and OJ Luiten. Extreme regimes of femtosecond photoemission from a copper cathode in a dc electron gun. *Physical Review Accelerators and Beams*, 19(10):103403, 2016.

[17] The compact linear collider.

[18] Arthur H Compton. A quantum theory of the scattering of x-rays by light elements. *Physical review*, 21(5):483, 1923.

[19] Jom Luiten. Ics-sxr source, Nov 2015.

[20] Marco Sluis. Artist impression of the smart*light setup, 2020.

[21] Helmut Wiedemann. *Particle accelerator physics*. Springer Nature, 2015.

[22] Klaus Wille. *The physics of particle accelerators: an introduction*. Clarendon Press, 2000.

[23] Klaus Floettmann. Some basic features of the beam emittance. *Physical Review Special Topics-Accelerators and Beams*, 6(3):034202, 2003.

[24] Dieter Möhl. Sources of emittance growth. 2006.

[25] WS Graves, LF DiMauro, R Heese, ED Johnson, J Rose, J Rudati, T Shaftan, and B Sheehy. Measurement of thermal emittance for a copper photocathode. In *PACS2001. Proceedings of the 2001 Particle Accelerator Conference (Cat. No. 01CH37268)*, volume 3, pages 2227–2229. IEEE, 2001.

[26] Herbert B Michaelson. The work function of the elements and its periodicity. *Journal of applied physics*, 48(11):4729–4733, 1977.

[27] W Li and DY Li. On the correlation between surface roughness and work function in copper. *The Journal of chemical physics*, 122(6):064708, 2005.

[28] DH Dowell, FK King, RE Kirby, JF Schmerge, and JM Smedley. In situ cleaning of metal cathodes using a hydrogen ion beam. *Physical Review Special Topics-Accelerators and Beams*, 9(6):063502, 2006.

[29] H Chen, Y Du, W Gai, A Grudiev, J Hua, W Huang, JG Power, EE Wisniewski, W Wuensch, C Tang, et al. Surface-emission studies in a high-field rf gun based on measurements of field emission and schottky-enabled photoemission. *Physical review letters*, 109(20):204802, 2012.

[30] HJ Qian, C Li, YC Du, LX Yan, JF Hua, WH Huang, and CX Tang. Experimental investigation of thermal emittance components of copper photocathode. *Physical Review Special Topics-Accelerators and Beams*, 15(4):040102, 2012.

[31] David H Dowell and John F Schmerge. Quantum efficiency and thermal emittance of metal photocathodes. *Physical Review Special Topics-Accelerators and Beams*, 12(7):074201, 2009.

[32] D Dowell, S Lidia, and J Schmerge. Lecture 2: Electron emission and cathode emittance, uspas course on high brightness electron injectors for 4th generation light sources, uc santa cruz, january 2008 santa rosa, ca.

[33] Hyeri Lee, Siddharth Karkare, Luca Cultrera, Andrew Kim, and Ivan V Bazarov. Review and demonstration of ultra-low-emittance photocathode measurements. *Review of Scientific Instruments*, 86(7):073309, 2015.

[34] Ryoji Nagai, Ryoichi Hajima, and Nobuyuki Nishimori. Magnetic emittance suppression using a bucking coil for a dc photocathode electron gun. *Review of Scientific Instruments*, 83(12):123303, 2012.

[35] Vinit Kumar. Understanding the focusing of charged particle beams in a solenoid magnetic field. *American Journal of Physics*, 77(8):737–741, 2009.

[36] M Ferrario, M Migliorati, and L Palumbo. Space charge effects.

[37] Thomas P Wangler. Emittance growth from space-charge forces. In *AIP Conference Proceedings*, volume 253, pages 21–40. American Institute of Physics, 1992.

[38] Ivan V Bazarov, Bruce M Dunham, Colwyn Gulliford, Yulin Li, Xianghong Liu, Charles K Sinclair, Ken Soong, and Fay Hannon. Benchmarking of 3d space charge codes using direct phase space measurements from photoemission high voltage dc gun. *Physical Review Special Topics-Accelerators and Beams*, 11(10):100703, 2008.

[39] Alexander Wu Chao, Karl Hubert Mess, et al. *Handbook of accelerator physics and engineering*. World scientific, 2013.

[40] David J Griffiths. Introduction to electrodynamics, 2005.

[41] Hitoshi Hayano. Wire scanners for small emittance beam measurement in atf. *arXiv preprint physics/0008084*, 2000.

[42] K Poorrezaei, RB Fiorito, RA Kishek, and BL Beaudoin. New technique to measure emittance for beams with space charge. *Physical Review Special Topics-Accelerators and Beams*, 16(8):082801, 2013.

[43] M Martini and Horst Otto Schönauer. Emittance measurements in the cern ps complex. *Part. Accel.*, 58(CERN-PS-97-018-CA):137–151, 1997.

[44] P Piot, J Song, R Li, GA Krafft, D Kehne, K Jordan, E Feldl, and J-C Denard. A multislit transverse-emittance diagnostic for space-charge-dominated electron beams. In *Proceedings of the 1997 Particle Accelerator Conference (Cat. No. 97CH36167)*, volume 2, pages 2204–2206. IEEE, 1997.

[45] Siriwan Pakluea and Sakhorn Rimjaem. Design and development of emittance measurement device by using the pepper-pot technique. In *Journal of Physics: Conference Series*, volume 901, page 012025. IOP Publishing, 2017.

[46] W Root et al. *Generation of high-field, single-cycle terahertz pulses using relativistic electron bunches*. PhD thesis, Ph. D. thesis, Eindhoven University of Technology, 2009.

[47] KT McDonald and DP Russell. Methods of emittance measurement. In *Frontiers of particle beams; observation, diagnosis and correction*, pages 122–132. Springer, 1989.

[48] Lianmin Zheng, Jiahang Shao, Yingchao Du, John G Power, Eric E Wisniewski, Wanming Liu, Charles E Whiteford, Manoel Conde, Scott Doran, Chunguang Jing, et al. Overestimation of thermal emittance in solenoid scans due to coupled transverse motion. *Physical Review Accelerators and Beams*, 21(12):122803, 2018.

[49] Y Yamazaki, T Kurihara, H Kobayashi, I Sato, and A Asami. High-precision pepper-pot technique for a low-emittance electron beam. *Nuclear Instruments and Methods in Physics Research Section A: Accelerators, Spectrometers, Detectors and Associated Equipment*, 322(2):139–145, 1992.

[50] SG Anderson, JB Rosenzweig, GP LeSage, and JK Crane. Space-charge effects in high brightness electron beam emittance measurements. *Physical Review Special Topics-Accelerators and Beams*, 5(1):014201, 2002.

[51] Min Zhang. Emittance formula for slits and pepper-pot measurement. Technical report, Fermi National Accelerator Lab., Batavia, IL (United States), 1996.

[52] Marco Sluis. Technical drawing of pepper-pot for project wiebe toonen, 2018.

[53] National Institute of Standards and NIST Technology. Estar : Stopping power and range tables for electrons.

[54] Wang Wen-Jing, Huang Sen-Lin, Quan Sheng-Wen, Lin Lin, and Liu Ke-Xin. An emittance measurement device for a space-charge dominated electron beam. *Chinese Physics C*, 36(9):867, 2012.

[55] K.A. Daamen. Reverse engineering the ingcrys laser systems ltd. third harmonic generation crystal package, 2007.

[56] GPT User Manual. Pulsar physics. *Flamingostraat*, 24:3582.

[57] DoctorX Works b.v. Steering coils, 2020. https://drx-works.nl/?products=steering-coils.

[58] Beam Imaging Solutions. Phosphor screens, 2020. http://beamimaging.com/product/phosphor-screens/.

[59] Blackfly FLIR. Blackfly s gige, 2020. https://www.flir.eu/products/blackfly-s-gige/?model=BFS-PGE-31S4M-C.

Chapter 8

Appendices

A Symbol list

Alfven current	I_A
angle reflected x-ray photon	θ
average velocity electrons electron beam	v
beam rotation due to solenoid field	ϕ
beam size fit function counts CCD pixel	d
beam size fit function amplitude fitted Gaussian	A
beam size fit function offset x- and y- position	x_0, y_0
beam size fit function beam radius	σ_r
beam size fit function offset counts	B
Boltzmann constant	k_B
brilliance x-ray beam	$B*_x$
bunch charge	Q_{bunch}
cross section electron beam at interaction point	σ_e
cross section laser beam at interaction point	σ_0
effective work function	π_{eff}
electric field	G_a
electron charge	e
electron mass	m_e
electron temperature	T_b
emittance, initial photo-electric normalized root mean square x-x' plane	$\varepsilon_{x,photo}$
emittance, magnetic normalized root mean square (x-x' plane)	$\varepsilon_{x,mag}$
emittance, normalized root mean square	$\varepsilon_{n,rms}$
emittance, total normalized root mean square (x-x' plane)	$\varepsilon_{x,tot}$
kinetic energy	E_{kin}
laminarity parameter	ρ
Larmour frequency	ω_L
Lorentz factor	γ
magnetic field on-axis (z-direction)	B_z
magnetic field (radial)	B_r

number of electrons at interaction point	N_e
number of electrons per bunch	$N_{e,bunch}$
number of photons at interaction point	N_0
number of stacked solenoid layers	k
number of solenoid windings per meter	n
number of x-ray photons at interaction point	N_x
particle momenta	p_x, p_y, p_z
peak current	$\widehat{I}$
pepper-pot average divergence of the beamlet j	$\overline{x'_j}$
pepper-pot average divergence of all beamlets	$\overline{x'}$
pepper-pot average position beam at plate position	$\overline{x}$
pepper-pot beam size at pepper-pot plate position	σ_{beam}
pepper-pot beamlet size	σ_b
pepper-pot divergence of beamlet j	$\sigma_{x'_j}$
pepper-pot drift length	L_d
pepper-pot hole separation	s
pepper-pot hole size (radius)	h
pepper-pot number of electrons through hole j	n_j
pepper-pot position hole j	x_{hj}
pepper-pot position of the center of beamlet j on the screen	$\overline{X_j}$
pepper-pot rms size of beamlet j on the screen	σ_j
pepper-pot total number of electrons	N
relativistic beta factor	β
speed of light	c
solenoid current	I
solenoid focal length	f
solenoid inner radius	r_{min}
solenoid length	L
solenoid lens strength parameter	k^2
solenoid outer radius	r_{max}
solenoid radius (thin solenoid)	r
surface enhancement factor	β^*
surface work function	ϕ_0
Thomson cross section	σ_T
Twiss parameters	$\widehat{\alpha}$, $\widehat{\beta}$, $\widehat{\gamma}$
vacuum permeability	μ_0
vacuum permittivity	ε_0
waist-scan distance solenoid - screen	l_2
waist-scan distance virtual source - solenoid	l_1
waist-scan beam size on screen	σ_x
waist-scan virtual source size	σ_v
wavelength incoming photons before Compton scattering	λ_0
wavelength x-ray photons (after Compton scattering)	λ_x

B Magnetic field measurements for the steering coils

In section 5.4.2 the purpose of the steering coils is explained. Calibration measurements of the magnetic fields B_x and B_y are performed. The field profile of the magnetic fields in x- and y-direction are probed as a function of distance the center of the steering coil along the line of beam propagation (z-axis) for a current of 0.5 A. The obtained field profiles are displayed in figure 8.1a. As expected, the profiles of B_x and B_y are similar. The magnetic field strength B_x and B_y in the center of the steering coil are also measured as a function of applied solenoid current. The results for both fields are plotted in figure 8.1b and fitted with a linear function. From both the field profiles of B_x and B_y along the z-axis and the relation between current and magnetic field strength it can be concluded that the fields produced by the horizontal coils and the vertical coils behave similar.

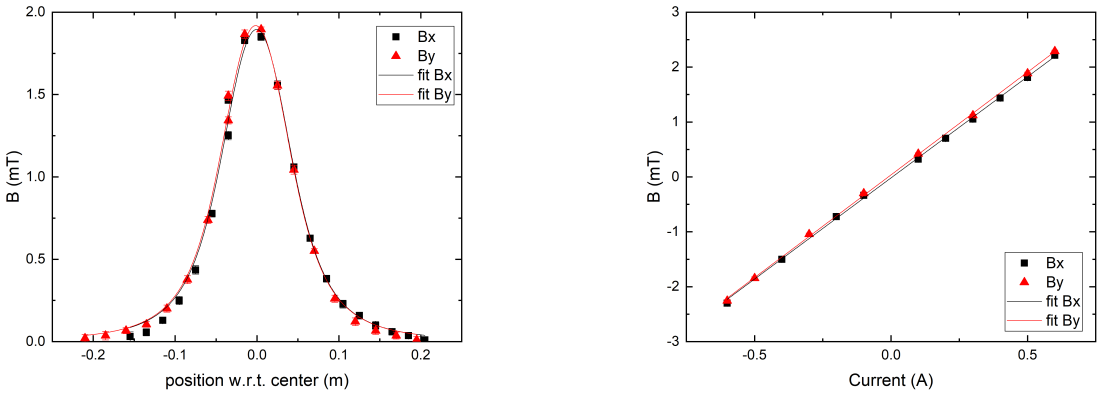

(a) (b)

Figure 8.1: a) Magnetic field profile of B_x and B_y as a function of distance to the center of the steering coil for a current of 0.5 A. b) Magnetic field B_x and B_y at the center of the steering coil as a function of current. The linear fits have a slope of respectively 3.68 ± 0.03 mT/A for B_x and 3.74 ± 0.03 mT/A for B_y.

C GPT code: test setup

C.1 smartlight.in

```
– constants –

FWHM2Gauss = (1/2.35482) ; Ratio of FWHM to 1 sigma

–Initial particle
setparticles("beam",N,me,qe,-Qtot); Set a beam of N macroparticles with mass me, charge qe and total charge of Qtot
settdist("beam","g",0,sigt*FWHM2Gauss,3,3); Set the distribution as gaussian with a 1 sigma length of sigt. Cut off at 3 sigma.
setrxydist( "beam", "u", Rb/2,Rb ) ; For 2D uniform distributions
setrxydist( "beam", "g", 0, Rb, 0, sright ) ; For gaussian profile
setphidist( "beam", "u", 0,2*pi ) ;  Uniform distribution azimuthal
setGBzdist( "beam", "u", 0.0016,0 ) ;  Emittance: 0.46 for uniform Rb=1 mm
setGBthetadist( "beam", "u", pi/4,pi/2 ) ;
setGBphidist( "beam", "u", 0,2*pi ) ;

–spacecharge if( Qtot)
spacecharge3Dmesh("Cathode","RestMaxGamma",1000) ;

 – photogun –
map2D_E("wcs","z",0,"map100kVgun10um.gdf","R","Z","Er","Ez",Efact); Superfish
forwardscatter("wcs","I","remove",0); deeltjesdietegendeanode
scatteriris("wcs","z",zIris,Rhole,1)scatter = "remove"; vliegen, wordenopgemerkt

 – gun solenoid –
R1sol1 = 87e-3/2 ;  Inner diameter
R2sol1 = 137e-3/2 ;  Outer diameter
Lsol1 = 61e-3 ;  Length
Nsol1 = 351 ;  Aantal wikkelingen
rectcoil("wcs","z", zAnode+zsol1, R1sol1, R2sol1, Lsol1, Nsol1*Isol1 ) ;

 – waist scan solenoid –
R1sol2 = 37e-3/2;87e-3/2 ;  Inner diameter
R2sol2 = 68e-3/2;137e-3/2 ;  Outer diameter
Lsol2 = 64e-3 ;  Length
Nsol2 = 759 ;  Aantal wikkelingen
rectcoil("wcs","z", zAnode+zsol2, R1sol2, R2sol2, Lsol2, Nsol2*Isol2 ) ;

–output–
accuracy(acc) ;
dtmaxt(-3*sigt,3*sigt,sigt/50) ;
zminmax("wcs","I",-1e-3, 2) ;
rmax("wcs","I",2e-2) ;
screen("wcs","I",0,1.16+zAnode,1e-3);
```

C.2 smartlight.mr

```
 Overall settings
acc 5
N 1e4 number of macroparticles
zAnode 18.4e-3
zIris 15.4e-3
Rhole 8e-3
Qtot 12e-12 amount of bunch charge
sigt 500e-15
Rb 150e-6 size laser spot on cathode
sright 3
Efact 1  1 is 100keV
zsol1 40e-3
Isol1 10.44 current is gun solenoid
zsolws 0.726 position waist scan solenoid w.r.t. anode
Isolws 2.5 5.5 0.02 current multirun waist scan solenoid

```

C.3 smartlight.bat

```
mr -o results.gdf scan_optimised.mr gpt -v smartlight.in

:rem Batch lines for screen command
gdfa -o avgs_position_screen.gdf results.gdf position Q nemixrms nemiyrms nemizrms nemirrms nemix90 nemiy90 nemiz90 nemix100 nemiy100 nemiz100 CSalphax CSalphay CSalphaz CSbetax CSbetay CSbetaz CSgammax CSgammay CSgammaz numpar avgr avgBx avgBy avgBz avgG avgx avgy avgz avgt stdG stdx stdy stdz stdt stdBx stdBy stdBz rmax dt_50 avgp
gdftrans -o traj_bunch.gdf results.gdf position x Bx

```

D Matlab script: pepper-pot beamlet propagation

```
clear all


%% Load data
cd 'C:\Users\s142761\OneDrive - TU Eindhoven\Documents\GPT\Smart light\20200123
    _beam dynamics 10MW pepper-pot_Annemarie\final beamline';

avgs_beam=load_gdf("finalbeam_avgs_position_screen_n1e5_nobunchercav.gdf");
traj_beam=load_gdf("finalbeam_results_n1e5_nobunchercav.gdf");

%% Simulation data
zAnode=18.4e-3;      %position anode w.r.t cathode (zero point)
zsol2=0.25;          %position sol2 w.r.t anode

d=12e-6;             %pepper-pot hole diameter
w=200e-6;            %pepper-pot hole separation
nholes=15;

%% Plot properties
ax=gca;
ax.FontSize=28;

%% Pepper-pot plate position
rmswaist.row=374;

% Save x and x' coordinates at xrms waist position
particle.xposition=zeros(1,avgs_beam.d.numpar(rmswaist.row));
particle.xbeta=zeros(1,avgs_beam.d.numpar(rmswaist.row));
particle.xprime=zeros(1,avgs_beam.d.numpar(rmswaist.row));

for j=1:avgs_beam.d.numpar(rmswaist.row)
    particle.xposition(1,j)=traj_beam(rmswaist.row+2).d.x(j);
    particle.xbeta(1,j)=traj_beam(rmswaist.row+2).d.Bx(j);
    particle.xprime(1,j)=particle.xbeta(1,j)/avgs_beam.d.avgBz(rmswaist.row);
end

%%% Plot trace space at xrms waist position
% figure(1)
% scatter(particle.xposition(1,:),particle.xprime(1,:),5,'filled');
% xlabel('x [m]','Fontsize',30);
% ylabel('xprime [rad]','Fontsize',30);
% ax=gca;
% ax.FontSize=28;
% pbaspect([1 1 1])
%
%% Create hole and select particles that get through, write properties of particles
    getting through in structure hole_calc
for h=1:nholes
    hmin=-(d+w)/2-(d+w)*(nholes-1)/2+(d+w)*(h-1);%-102.5e-6-205e-6*7+205e-6*(h-1);
```

```
48      hmax=(d+w)/2-(d+w)*(nholes-1)/2+(d+w)*(h-1);%102.5e-6-205e-6*7+205e-6*(h-1);
49      a=0;
50      b=0;
51       for n=1:avgs_beam.d.numpar(rmswaist.row)
52          if hmin<=particle.xposition(1,n) && particle.xposition(1,n)<=hmax
53              a=a+1;
54              beamlet.calc.hole(h).xpos(a,1)=particle.xposition(1,n);
55              beamlet.calc.hole(h).xprime(a,1)=particle.xprime(1,n);
56              beamlet.calc.hole(h).xbeta(a,1)=particle.xbeta(1,n);
57          else
58              b=b+1;
59          end
60       end
61          beamlet.calc.hole(h).npart=a;
62          beamlet.calc.hole(h).nohole=b;
63  end
64
65  %% Calculate the beamlet propagation
66  Ldrift=0:1e-3:0.059;
67  for h=1:nholes
68      beamlet.proj.hole(h).S=(d+w)*(h-1)-(d+w)*(nholes-1)/2;
69      for n=1:beamlet.calc.hole(h).npart
70          beamlet.proj.hole(h).xpos(n,:)=beamlet.proj.hole(h).S+beamlet.calc.hole(h).
                xpos(n,1)*d/(d+w)+beamlet.calc.hole(h).xprime(n,1).*Ldrift;
71          beamlet.proj.hole(h).xprime(n,:)=beamlet.calc.hole(h).xprime(n,1);
72      end
73  end
74
75  %%% Plot the beamlet propagation
76  % figure(4)
77  % for h=1:nholes
78  %      for n=1:beamlet.calc.hole(h).npart
79  %          plot(Ldrift(1,:),beamlet.proj.hole(h).xpos(n,:))
80  %          hold on
81  %      end
82  % end
83  % xlabel('z [m]','Fontsize',20)
84  % ylabel('x [m]','Fontsize',20);
85  %% title('Beamlet propagation, 0.95A','Fontsize',28);
86
87  %% Plot the beamlet projection on a screen
88  Ldrift=0.059;
89  screen=59;
90
91  figure(5)
92  for h=1:nholes
93      for n=1:beamlet.calc.hole(h).npart
94          screencount(h)=histogram(beamlet.proj.hole(h).xpos(:,screen));
95          screencount(h).BinWidth=20e-6;
96
97          hold on
98      end
```

```
99  end
100 xlabel('x [m]','Fontsize',28);
101 ylabel('counts','Fontsize',28);
```

E Matlab script: camera calibration

```
close all
clear all

importbmp("....bmp")

% Calculate pixel size
Pixels CCD 2048x1536

figure(1)                    % display entire image
imshow(cdata);

calculate horizontal pixel size: first click left, then click right
[xhpixel,yhpixel]=ginput(2);
nxhpixel=round(xhpixel(2))-round(xhpixel(1));
hpsize=28e-3/nxhpixel

calculate vertical pixel size: first click lower limit, then click upper
limit
[xvpixel,yvpixel]=ginput(2);
nvpixel=round(yvpixel(2))-round(yvpixel(1));
vpsize=28e-3/nvpixel

close figure 1

%% identify lines
BW=edge(cdata,'canny');

[H,theta,rho]=hough(BW);
peaks=houghpeaks(H,30);
lines=houghlines(cdata,theta,rho,peaks);

figure(1)
imshow(cdata)
hold on
for k=1:length(lines)
    xy=[lines(k).point1; lines(k).point2];
    plot(xy(:,1),xy(:,2),'Linewidth',2,'Color','green')
end


%% intensity profiles integrated lines
% Only integrate raster area

% define integration area
roi=drawrectangle();         % draw a rectangle around the region of interest and
    press enter
pos_rect=roi.Position;       % save the position of the drawn rectangle
pos_roi=round(pos_rect);     % round the position of the rectangle to .. pixel
    numbers
```

```
48 img_cropped=cdata(pos_roi(2)+(0:pos_roi(4)),pos_roi(1)+(0:pos_roi(3))); %save the
       date within the rectangle to img_cropped
49 img_cropped_rot=imrotate(img_cropped,0); %rotate image if necessary
50 % (rotate with given angle anti clockwise)
51
52 figure(2)                    % display a new image 1 with just the region of
       interest
53 imshow(img_cropped_rot)
54
55 %% Find linespacing
56 nlines=size(lines);
57      j=0;
58      k=0;
59 for i=1:nlines(1,2)
60      if lines(i).point1(1,1)==lines(i).point2(1,1)
61      j=j+1;
62      vline(j)=lines(i);
63      else k=k+1;
64      hline(k)=lines(i);
65      end
66 end
67
68 nvlines=size(vline);
69 for i=1:nvlines(1,2)
70 vdim(i)=vline(i).point1(1,1);
71 end
72 vdim=sort(vdim);
73
74 for j=1:nvlines(1,2)-1
75      vlinespacing(j)=vdim(j+1)-vdim(j);
76 end
77
78 nhlines=size(hline);
79 for i=1:nhlines(1,2)
80 hdim(i)=hline(i).point1(1,2);
81 end
82 hdim=sort(hdim);
83
84 for j=1:nhlines(1,2)-1
85      hlinespacing(j)=hdim(j+1)-hdim(j);
86 end
87
88 %% Plot intensity horizontal and vertical direction
89 hnpix_roi=[pos_roi(1):(pos_roi(1)+pos_roi(3))];
90 hcountdata=(sum(img_cropped_rot));
91 figure(3)
92 plot(hnpix_roi,hcountdata)
93 title('Horizontal integrated counts (2048 pixel direction)')
94 xlabel('pixel number')
95 ylabel('counts')
96
97 %find local minima (horizontal line position)
```

```
98  hcountdata_inverted=-hcountdata;
99  [hpks,hlocs]=findpeaks(hcountdata_inverted,'MinPeakDistance',40,'MinPeakHeight'
        ,-1.4e5);
100
101 vnpix_roi=[pos_roi(2):(pos_roi(2)+pos_roi(4))];
102 vcountdata=sum(transpose(img_cropped_rot));
103 figure(4)
104 plot(vnpix_roi,vcountdata)
105 title('Vertical integrated counts (1536 pixel direction)')
106 xlabel('pixel number')
107 ylabel('counts')
108
109 %find local minima (vertical line position)
110 vcountdata_inverted=-vcountdata;
111 [vpks,vlocs]=findpeaks(vcountdata_inverted,'MinPeakDistance',40,'MinPeakHeight'
        ,-1.6e5);
```

F Camera calibration

F.1 Pixel selection

For four calibration images, the pixel numbers for the calibration lines indicated in image 5.11 are selected. In table 8.1 the pixel numbers averaged for 10 repeated pixel selections performed for the same image are displayed. The uncertainty in pixel number is determined as the standard deviation of the set of 10 pixel values.

Table 8.1: Position of calibration lines on CCD array of Blackfly camera mounted on cross for every calibration iteration.

image number	pixel number left calibration line	pixel number right calibration line	pixel number upper calibration line	pixel number lower calibration line
1	347.2±1.6	1750.9±1.3	61.4±1.0	1459.1±1.1
2	346.8±0.6	1750.2±1.6	60.0±0	1458.0±1.1
3	346.2±1.0	1750.7±0.9	60.2±0.6	1458.6±0.8
4	348.2±1.0	1751.5±1.3	60.0±0.8	1457.6±1.0

F.2 Uncertainty in area one pixel represents on the phosphor screen

The total uncertainty in the area one a pixel represents on the phosphor screen is calculated by uncertainty propagation of the different uncertainties. In table 8.1 the pixel number of the calibration lines and the standard deviation for these pixel numbers are displayed. The pixel number of a calibration line is averaged over all four images. The uncertainty for this average pixel number is calculated by

$$\sigma_{\text{av}} = \frac{\sqrt{\sigma_1^2 + \sigma_2^2 + \sigma_3^2 + \sigma_4^2}}{4} \tag{8.1}$$

Where σ_{av} is the error in pixel number averaged for the four calibration images and σ_1, σ_2, σ_3 and σ_4 are respectively the uncertainties in pixel numbers for image 1, 2, 3 and 4. The uncertainty in the number of pixels between the two horizontal calibration lines can then be calculated as

$$\sigma_{\text{h,pix}} = \sqrt{\sigma_{\text{av,left}}^2 + \sigma_{\text{av,right}}^2} \tag{8.2}$$

Where $\sigma_{\text{av,left}}$ and $\sigma_{\text{av,right}}$ are respectively the uncertainties in the average pixel number of the left calibration line and the right calibration line and $\sigma_{\text{h,pix}}$ is the uncertainty in the number of pixels between the vertical calibration lines. The same calculation holds for the horizontal calibration lines. To calculate the size a pixel represents on the phosphor screen, the actual distance between the two opposing calibration lines is divided by the number of pixels that separate the two lines. If the average number of pixels between the two vertical calibration lines is n, the distance between the two vertical calibration lines is s and the uncertainty in distance between the two vertical calibration lines is given by $\sigma_{\text{h,dist}}$ the relative uncertainty in the size a pixel represents on the phosphor screen $\sigma_{\%h}$ is given by

$$\sigma_{\%h} = \sqrt{(\frac{\sigma_{\text{h,dist}}}{n})^2 + (\frac{\sigma_{\text{h,dist}}}{s})^2} \tag{8.3}$$

G Uncertainty in bunch charge

In section 5.5.3 the ratio between charge measured in the Faraday cup and charge measured on the phosphor screen is determined. For each UV laser beam intensity the time required to accumulate certain charge in the Faraday cup or on the phosphor screen is measured three times. The average charge per bunch is calculated for each measurement. The three measurements are averaged and the standard deviation is determined. The ratio between charge measured in the Faraday cup and charge measured on the phosphor screen is determined by dividing the bunch charge measured with the Faraday cup by the bunch charge measured on the phosphor screen. The uncertainty σ_{ratio} devided by ratio r can be calculated with

$$\frac{\sigma_{\text{ratio}}}{r} = \sqrt{(\frac{\sigma_{\text{cup}}}{q_{\text{cup}}})^2 + (\frac{\sigma_{\text{screen}}}{q_{\text{screen}}})^2} \tag{8.4}$$

where σ_{cup} is the uncertainty in the bunch charge q_{cup} measured in the Faraday cup and σ_{screen} is the uncertainty in the bunch charge q_{screen} measured on the phosphor screen. The ratios for the three UV laser beam intensities on the cathode are of the same order. To come to one ratio that can be used for all bunch charge measurements, the three calculated ratios are averaged. The uncertainty in the average ratio $\sigma_{\overline{\text{ratio}}}$ is calculated as

$$\sigma_{\overline{\text{ratio}}} = \frac{\sqrt{\sigma^2_{\text{ratio},1} + \sigma^2_{\text{ratio},2} + \sigma^2_{\text{ratio},3}}}{3} \tag{8.5}$$

where $\sigma_{\text{ratio},1}$, $\sigma_{\text{ratio},2}$ and $\sigma_{\text{ratio},3}$ are the uncertainties of the ratios calculated with equation 8.4 for the different UV laser beam intensities. The total uncertainty in bunch charge not only depends on the uncertainty in the measured bunch charge ratio but also on the variation of bunch charge due to variation in UV laser beam intensity on the cathode. It is estimated that the UV laser beam intensity shows relative variations of approximately $\sigma_{\%q} = 10\%$. The total relative uncertainty in bunch charge $\sigma_{\%\text{bunch}}$ calculated from a charge measurement performed with the phosphor screen is

$$\sigma_{\%\text{bunch}} = \sqrt{(\frac{\sigma_{\overline{\text{ratio}}}}{\overline{r}})^2 + (\sigma_{\%q})^2} \tag{8.6}$$

where $\overline{r}$ is the average ratio between cup and screen.

H Matlab script: fit beam size

H.1 General script

```
close all
clear all

%% physical constants
mu0=1.2566370614e-6;      %Newton/Ampere^2
qe=1.60217662e-19;        %Coulomb
me=9.10938356e-31;        %kilograms
c=299792458;              %m/s

%% file folder
cd 'location image folder';
files=dir('*.bmp');

%% Load image and fit spots with gaussians, save std, mean and amplitude
for i=1:length(files)
    cd 'location image folder'; %select the location of the data images
    importbmp(files(i).name); %import image i
    image(i).current_sol2=str2double(files(i).name(20:28))/100e4; %save the current
        for which this image was taken
    image(i).nimage=str2double(files(i).name(31)); %save the number of this image
    data_double=double(cdata); %convert the image to a double

    data_spot=data_double(250:1100,550:1400); %select part image that contains the
       spot
    maxValue= max(data_spot, [], 'all'); %find the pixel with the highest number of
        counts
    [ymax, xmax] = find(data_spot == maxValue); %find the coordinate of the pixel
       with the highest number of counts
    x=1:size(data_spot,2); %create an array to number the image columns
    y=1:size(data_spot,1); %create an array to number the image rows


    cd 'location image analysis folder'; %select the location where analysis
       pictures are to be stored
    f=figure('visible','off');
    imagesc(data_spot);
    colorbar
    saveas(gcf,sprintf('image_Isol2=%d_%d.png',image(i).current_sol2,image(i).
       nimage))%save the image of the spot
    close(f)

    [fitresult, gof] = fitsigmar(x, y, data_spot, maxValue,xmax(1),ymax(1));%fit
       the spot with the fitfunction as printed in the next subappendix
    saveas(gcf,sprintf('3Dfit_Isol2=%d_%d.png',image(i).current_sol2,image(i).
       nimage))%save the image of the fit
    close all

```

```
40      %% save the fitparameters
41      image(i).sigmar=fitresult.sigmar;
42      image(i).x0=fitresult.x0;
43      image(i).y0=fitresult.y0;
44      image(i).amplitude=fitresult.A;
45      image(i).gof.sse=gof.sse;
46      image(i).gof.rsquare=gof.rsquare;
47      image(i).gof.dfe=gof.dfe;
48      image(i).gof.adjrsquare=gof.adjrsquare;
49      image(i).gof.rmse=gof.rmse;
50      image(i).conf95=confint(fitresult);
51
52      %% Map and plot the differences between fit and data
53      for j=1:length(x)
54          for k=1:length(y)
55              fitfunction(k,j)=round(image(i).amplitude*exp(-((j-image(i).x0).^2+(k-
                    image(i).y0).^2)./(2*image(i).sigmar^2)));
56          end
57      end
58      checkfit=data_spot-fitfunction;
59
60      f=figure('visible','off');
61      imagesc(checkfit)
62      colorbar
63      saveas(gcf,sprintf('checkfit_Isol2=%d_%d.png',image(i).current_sol2,image(i).
            nimage))
64      close(f)
65  end
66
67  %% average the fitparameters of images with same Isol2
68  average.matrix_Isol2(1,1)=image(1).current_sol2;
69  average.matrix_sigmar(1,1)=image(1).sigmar;
70  average.matrix_x0(1,1)=image(1).x0;
71  average.matrix_y0(1,1)=image(1).y0;
72  average.matrix_amplitude(1,1)=image(1).amplitude;
73  average.matrix_uncertainty_meas_sigmar(1,1)=image(1).conf95(2,2)-image(1).conf95
        (1,2);
74  average.matrix_rsquared(1,1)=image(1).gof.rsquare;
75  k=1;
76  j=2;
77  for i=2:length(files)
78      if image(i).current_sol2==image(i-1).current_sol2
79          average.matrix_Isol2(j,k)=image(i).current_sol2;
80          average.matrix_sigmar(j,k)=image(i).sigmar;
81          average.matrix_x0(j,k)=image(i).x0;
82          average.matrix_y0(j,k)=image(i).y0;
83          average.matrix_amplitude(j,k)=image(i).amplitude;
84          average.matrix_uncertainty_meas_sigmar(j,k)=image(i).conf95(2,2)-image(i).
                conf95(1,2);
85          average.matrix_rsquared(j,k)=image(i).gof.rsquare;
86          j=j+1;
87      else
```

```
88          k=k+1;
89          average.matrix_Isol2(1,k)=image(i).current_sol2;
90          average.matrix_sigmar(1,k)=image(i).sigmar;
91          average.matrix_x0(1,k)=image(i).x0;
92          average.matrix_y0(1,k)=image(i).y0;
93          average.matrix_amplitude(1,k)=image(i).amplitude;
94          average.matrix_uncertainty_meas_sigmar(1,k)=image(i).conf95(2,2)-image(i).
                conf95(1,2);
95          average.matrix_rsquared(1,k)=image(i).gof.rsquare;
96          j=2;
97      end
98  end
99
100 average.Isol2=mean(average.matrix_Isol2(1:5,:));
101 average.sigmar=mean(average.matrix_sigmar(1:5,:)).*2e-5;
102 average.dsigmar=(max(average.matrix_sigmar)-min(average.matrix_sigmar))/(4*sqrt(5))
        .*2e-5;
103 average.x0=mean(average.matrix_x0(1:5,:));
104 average.y0=mean(average.matrix_y0(1:5,:));
105 average.amplitude=mean(average.matrix_amplitude(1:5,:));
106 average.rsquared=mean(average.matrix_rsquared(1:5,:));
107
108 %% Calculate gamma %%put this somewhere in report, make chapter relativistic
        effects
109 Egun=100e3;
110 Erest=0.511e6;
111 gamma=Egun/Erest+1;
112 v=c*sqrt(1-1/gamma^2);
113
114 %% Focussing magnetic solenoid
115
116 %on-axis solenoid field thick finite solenoid
117 n=359/61e-3;      %number of windings per meter
118 L=61e-3;          %Length solenoid
119 rmax=0.06675;     %maximum radius solenoid
120 rmin=0.04475;     %minimum radius solenoid
121 k=9;              %number of stacks
122 nI=length(average.Isol2);
123 syms Bzstack(z) Bz(z) Bz2(z) Bzstack_new(z)
124 for i=1:nI
125     Bzstack(z)=0;
126     for j=1:k
127         Bzstack_new(z)=((L+z)/sqrt((L+z)^2+(rmin+(j-1/2)*(rmax-rmin)/k)^2)-z/sqrt(z
                ^2+(rmin+(j-1/2)*(rmax-rmin)/k)^2));
128         Bzstack(z)=Bzstack(z)+Bzstack_new;
129     end
130     Bz(z)=mu0*n*average.Isol2(i)/(2*k)*Bzstack;
131     Bz2(z)=Bz^2;
132     spot.I(i).Bzcenter=double(Bz(-L/2));%on-axis magnetic field in center of
            solenoid
133     spot.I(i).Leff=double(1/spot.I(i).Bzcenter^2*vpaintegral(Bz2,z,-inf,inf));
```

```
    spot.I(i).intBz2=double(vpaintegral(Bz2,z,-inf,inf));%-L-(spot.I(i).Leff-L)/2,(spot.I(i).Leff-L)/2));
    spot.I(i).oneoverf=double((qe^2/(4*gamma^2*me^2*v^2)*spot.I(i).intBz2));%one over focal length
end
f=zeros([nI 1]);
for i=1:nI
    f(i)=1/spot.I(i).oneoverf;
end
```

H.2 Fit function

```
function [fitresult, gof] = fitsigmar(x, y, data_spot, Maximum, xmax, ymax)
%CREATEFIT(X,Y,DATA_SPOT)
%  Create a fit.
%
%  Data for 'sigmar' fit:
%      X Input : x
%      Y Input : y
%      Z Output: data_spot
%  Output:
%      fitresult : a fit object representing the fit.
%      gof : structure with goodness-of fit info.
%
%  See also FIT, CFIT, SFIT.

%  Auto-generated by MATLAB on 14-Oct-2020 19:54:37


%% Fit: 'sigmar'.
[xData, yData, zData] = prepareSurfaceData( x, y, data_spot );

% Set up fittype and options.
ft = fittype( 'A*exp(-((x-x0)^2+(y-y0)^2)/(2*sigmar^2))+B', 'independent', {'x', 'y'}, 'dependent', 'z' );
opts = fitoptions( 'Method', 'NonlinearLeastSquares' );
opts.Display = 'Off';
opts.Lower = [0 0 0 0 0];
opts.StartPoint = [Maximum 10 0 xmax ymax];
opts.Upper = [255 300 255 601 601];

% Fit model to data.
[fitresult, gof] = fit( [xData, yData], zData, ft, opts );

% Plot fit with data.
figure( 'visible','off','Name', 'sigmar' );
h = plot( fitresult, [xData, yData], zData );
legend( h, 'sigmar', 'data_spot vs. x, y', 'Location', 'NorthEast', 'Interpreter', 'none' );
% Label axes
xlabel( 'x', 'Interpreter', 'none' );
```

```
38 ylabel( 'y', 'Interpreter', 'none' );
39 zlabel( 'intensity', 'Interpreter', 'none' );
40 grid on
41 view( -6.9, 20.4 );
```

I Uncertainty in beam size

In appendices **??** and **??** the scripts used to analyse the waist-scan images are printed. In section 6.2.1 this process is explained. In this appendix, the calculation of the total error in beam size is elaborated.

The images are fitted with Gaussian function **??**. The fit parameter σ_r represents the rms beam size. The confidence bound of the fit parameters is set to 0.6827. This means that the confidence bound indicates a range of 2σ. Since the beam size is found by averaging over 5 images, the standard deviation should be the result of error propagation of the standard deviation of each fit.

$$\sigma_{\mathrm{fit}\sigma_r} = \frac{\sqrt{\sigma^2_{\sigma_r 1} + \sigma^2_{\sigma_r 2} + \sigma^2_{\sigma_r 3} + \sigma^2_{\sigma_r 4} + \sigma^2_{\sigma_r 5}}}{5} \tag{8.7}$$

In this equation $\sigma_{\mathrm{fit}\sigma_r}$ is the uncertainty in the size of the beam due to the fit in pixels and $\sigma_{\sigma_r 1}$, $\sigma_{\sigma_r 2}$, $\sigma_{\sigma_r 3}$, $\sigma_{\sigma_r 4}$ and $\sigma_{\sigma_r 1}$ are the standard deviations of the respective fits in pixels. Another source for uncertainty is the uncertainty in pixel size $\sigma_{\sigma\mathrm{pixel}}$ as calibrated in section 5.5.2.

$$\sigma_{\sigma_r} = \sigma_r \cdot \sqrt{(\frac{\sigma_{\mathrm{fit}\sigma_r}}{\mathrm{fit}\sigma_r})^2 + (\frac{\sigma_{\sigma\,\mathrm{pixel}}}{\sigma_{pixel}})^2} \tag{8.8}$$

Here σ_{σ_r} is the total uncertainty in spot size, σ_r is the mean beam size, $\mathrm{fit}\sigma_r$ is the mean beam size from the fits in pixels and σ_{pixel} is the calibrated pixel size.

J Fits waist-scan series 0.7 pC ±15% bunches

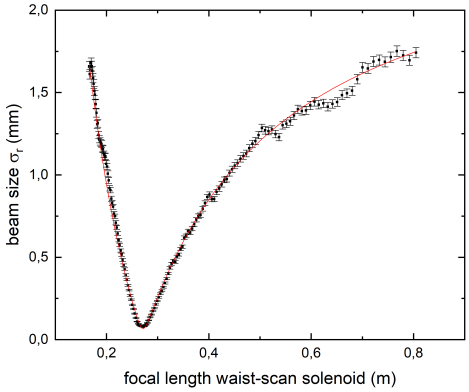

(a) Gun solenoid current 9.65 A

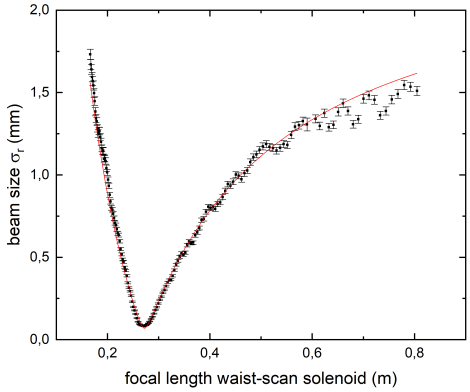

(b) Gun solenoid current 9.75 A

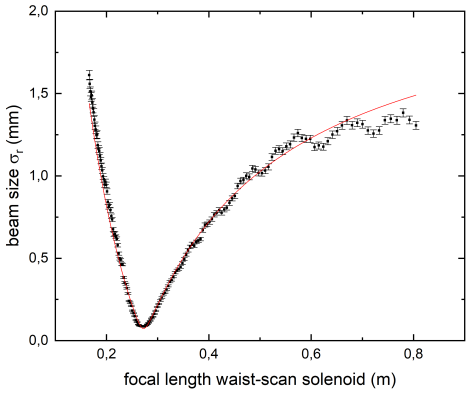

(c) Gun solenoid current 9.85 A

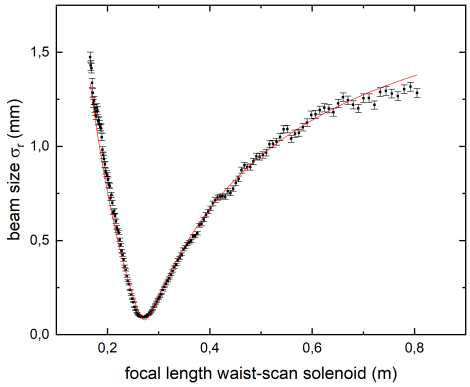

(d) Gun solenoid current 9.95 A

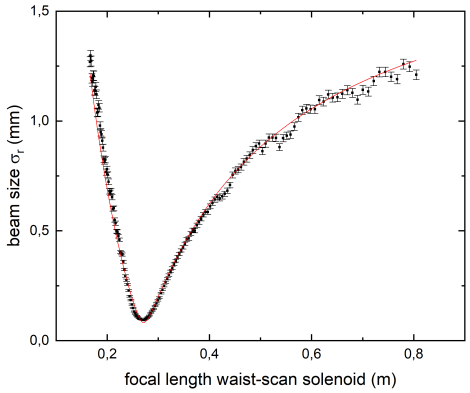

(e) Gun solenoid current 10.05 A

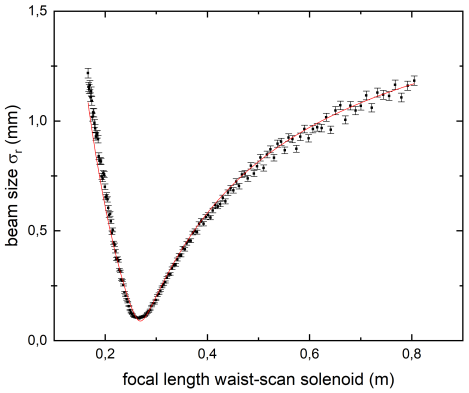

(f) Gun solenoid current 10.15 A

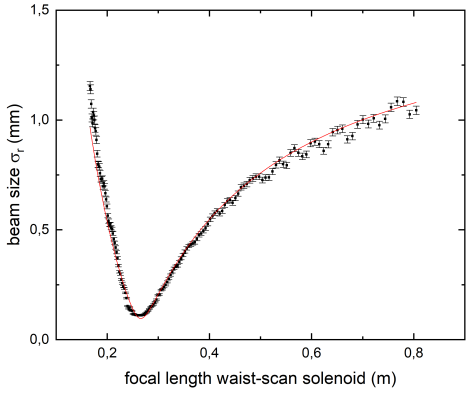

(g) Gun solenoid current 10.25 A

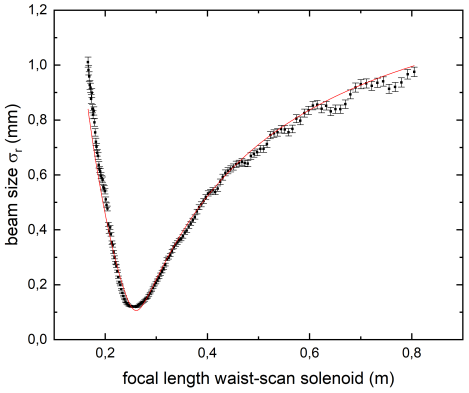

(h) Gun solenoid current 10.35 A

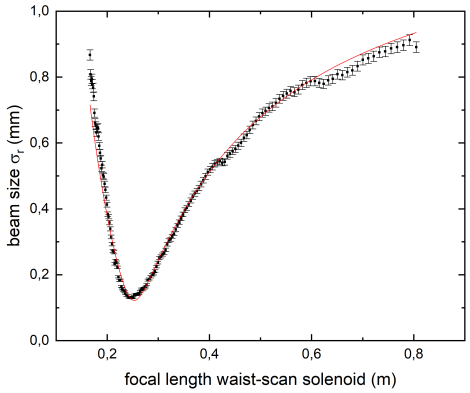

(i) Gun solenoid current 10.45 A

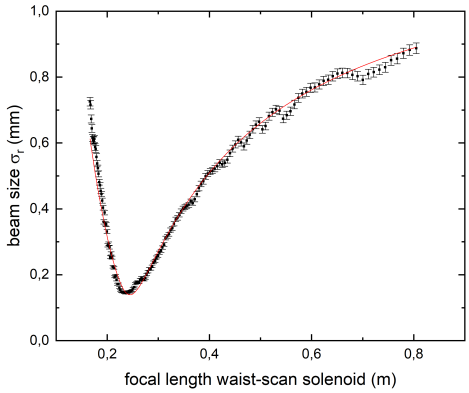

(j) Gun solenoid current 10.55 A

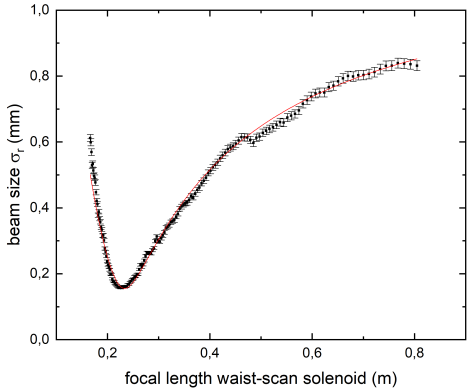

(k) Gun solenoid current 10.65 A

Figure 8.2: The data sets and corresponding fits of the individual waist scans performed on 0.7 pC $\pm$ 15% bunches and different gun solenoid currents. The beam size on the phosphor screen is plotted as a function of the focal length of the waist-scan solenoid and fitted with the waist-scan fit function. The bunches are created with a Gaussian UV laser beam profile on the cathode.

K Fits waist-scan series 12 pC ±15% bunches

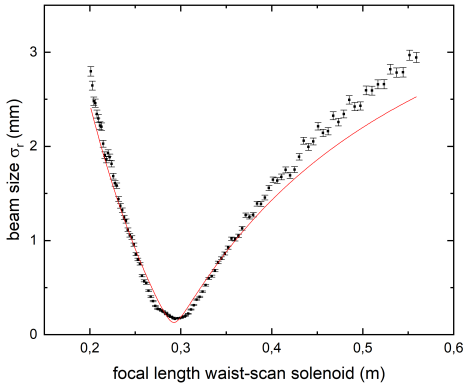

(a) Gun solenoid current 10.15 A

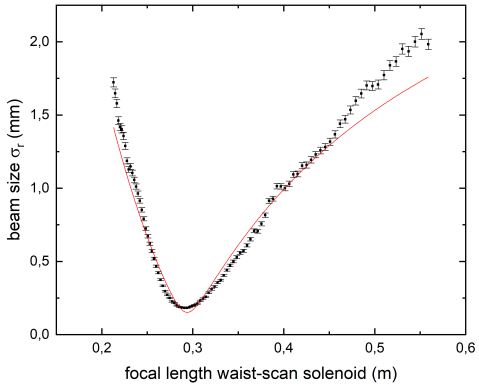

(b) Gun solenoid current 10.44 A

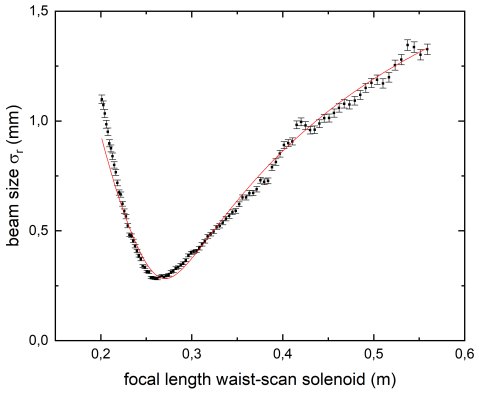

(c) Gun solenoid current 10.75 A

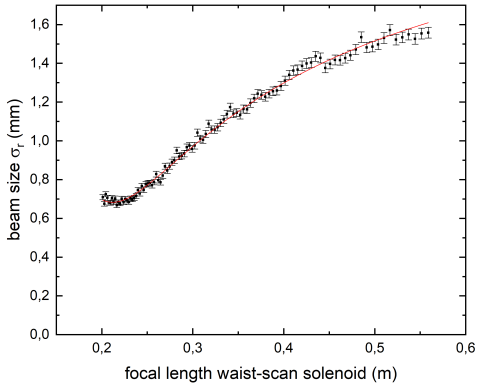

(d) Gun solenoid current 11.05 A

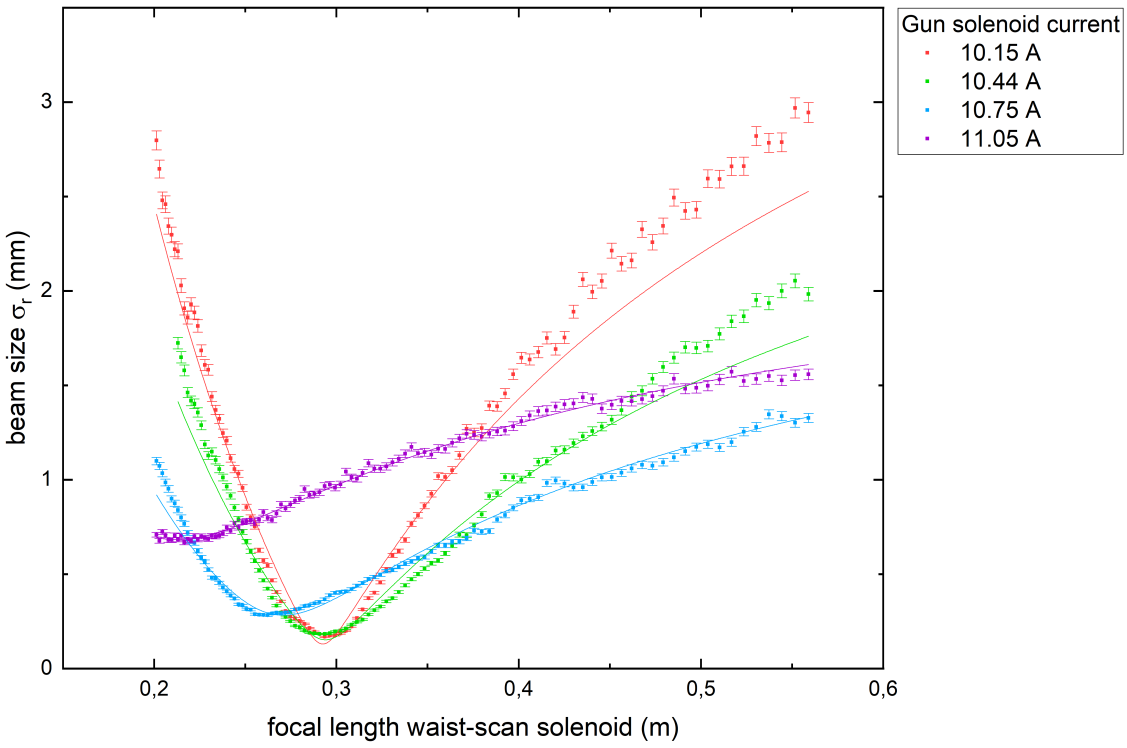

(e) All four data sets are plotted in the same figure.

Figure 8.3: The data sets and corresponding fits of the individual waist scans performed on 12 pC ± 15% bunches and different gun solenoid currents. The beam size on the phosphor screen is plotted as a function of the focal length of the waist-scan solenoid and fitted with the waist-scan fit function. The bunches are created with a Gaussian UV laser beam profile on the cathode.

L Fits waist-scan series 2.1 pC ±15% bunches

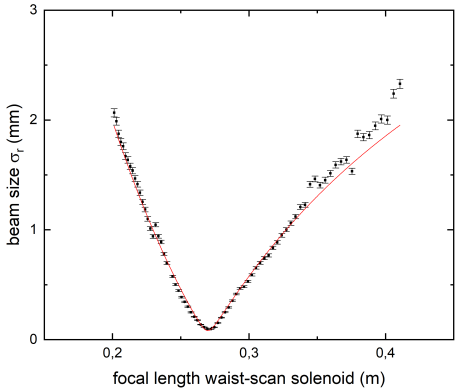

(a) Gun solenoid current 9.50 A

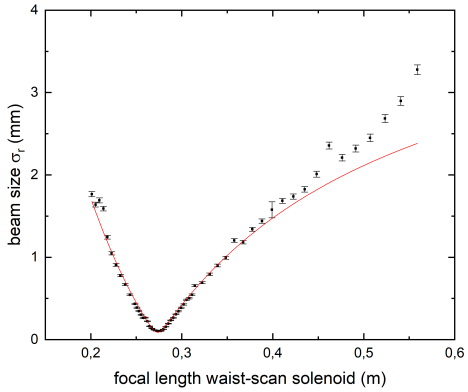

(b) Gun solenoid current 9.75 A

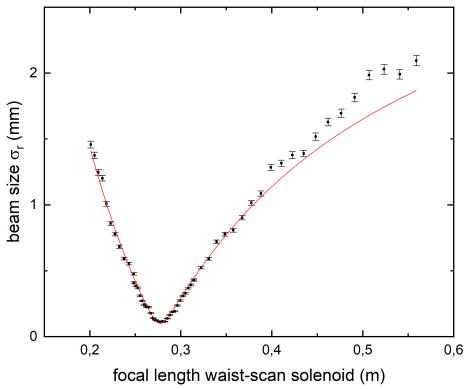

(c) Gun solenoid current 10.00 A

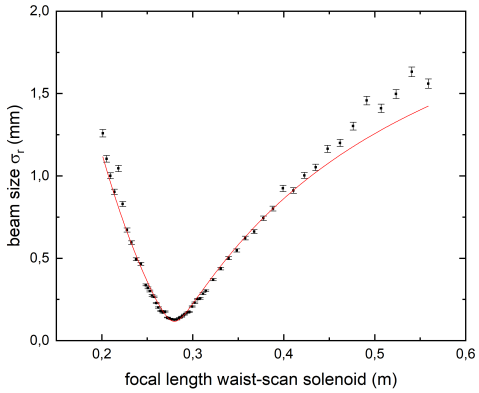

(d) Gun solenoid current 10.25 A

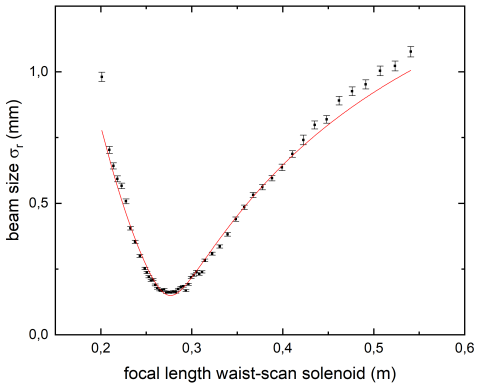

(e) Gun solenoid current 10.50 A

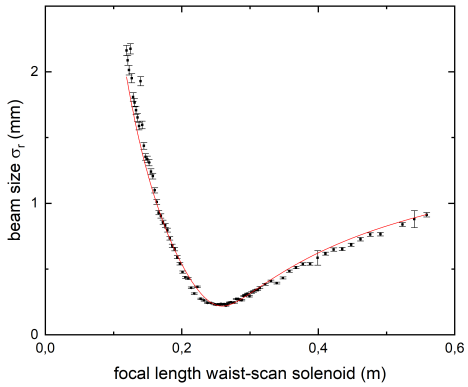

(f) Gun solenoid current 10.75 A

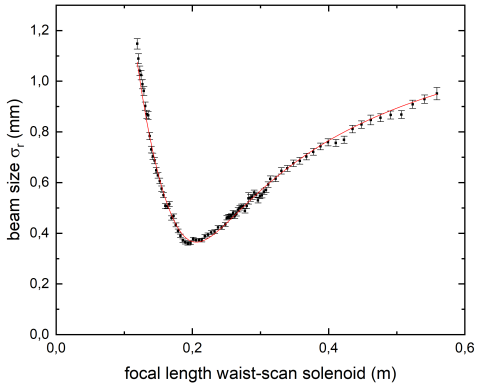

(g) Gun solenoid current 11.00 A

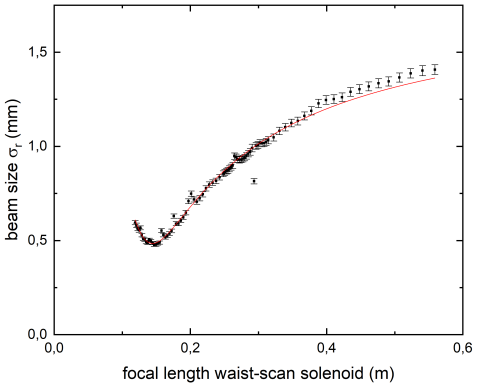

(h) Gun solenoid current 11.25 A

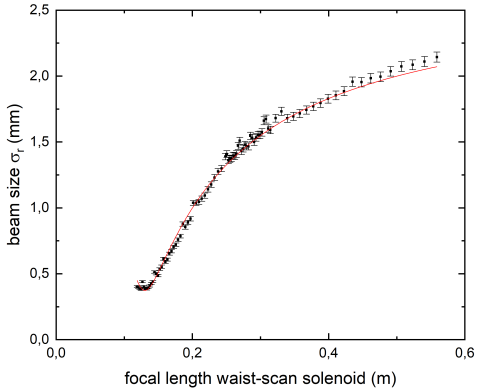

(i) Gun solenoid current 11.50 A

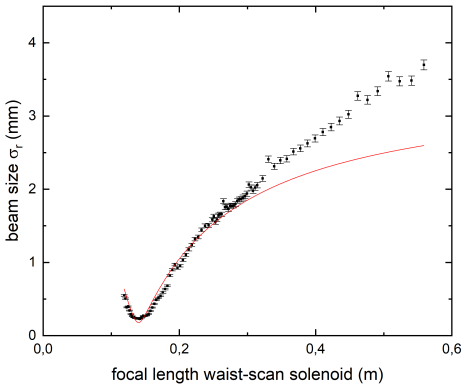

(j) Gun solenoid current 11.75 A

Figure 8.4: The data sets and corresponding fits of the individual waist scans performed on 2.1 pC $\pm$ 15% bunches and different gun solenoid currents. The beam size on the phosphor screen is plotted as a function of the focal length of the waist-scan solenoid and fitted with the waist-scan fit function. The bunches are created with a flat top UV laser beam profile on the cathode.

M Fits waist scan-series 5.4 pC ± 15% bunches

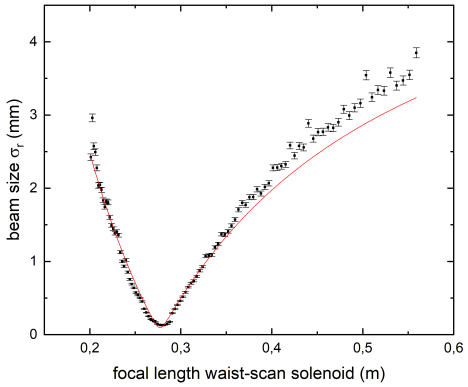

(a) Gun solenoid current 9.75 A

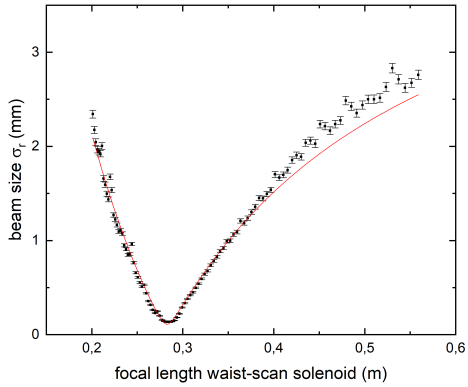

(b) Gun solenoid current 10.00 A

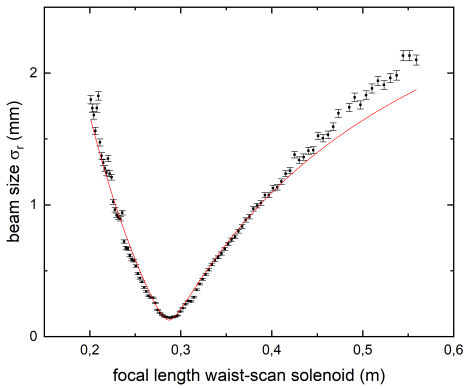

(c) Gun solenoid current 10.25 A

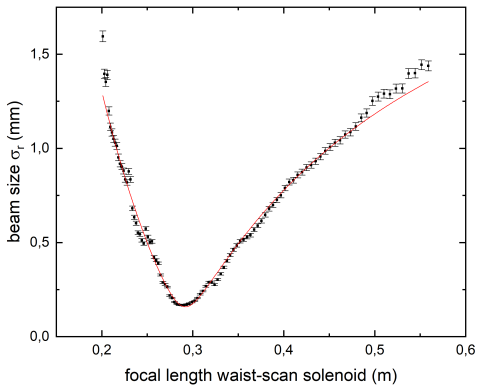

(d) Gun solenoid current 10.50 A

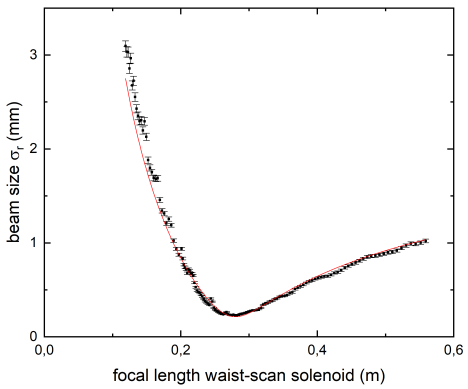

(e) Gun solenoid current 10.75 A

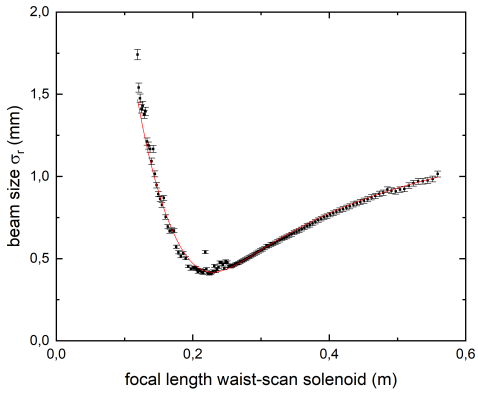

(f) Gun solenoid current 11.00 A

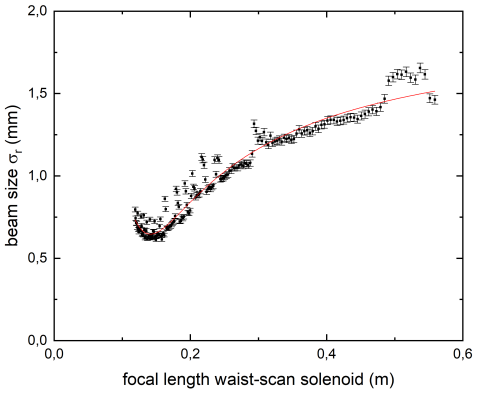

(g) Gun solenoid current 11.25 A

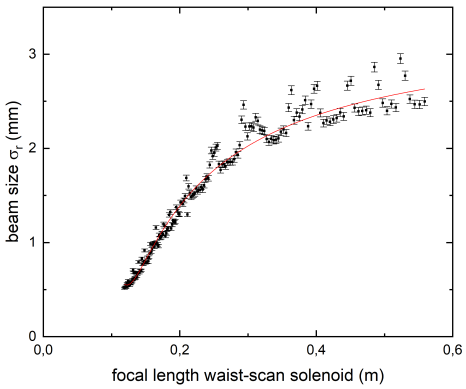

(h) Gun solenoid current 11.50 A

Figure 8.5: The data sets and corresponding fits of the individual waist scans performed on 5.4 pC ± 15% bunches and different gun solenoid currents. The beam size on the phosphor screen is plotted as a function of the focal length of the waist-scan solenoid and fitted with the waist-scan fit function. The bunches are created with a flat top UV laser beam profile on the cathode.

N Fits waist-scan series 15 pC ± 15% bunches

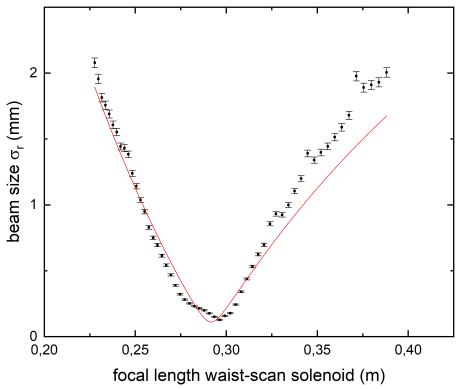

(a) Gun solenoid current 10.00 A

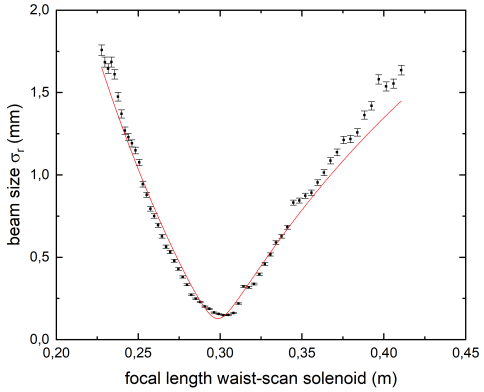

(b) Gun solenoid current 10.25 A

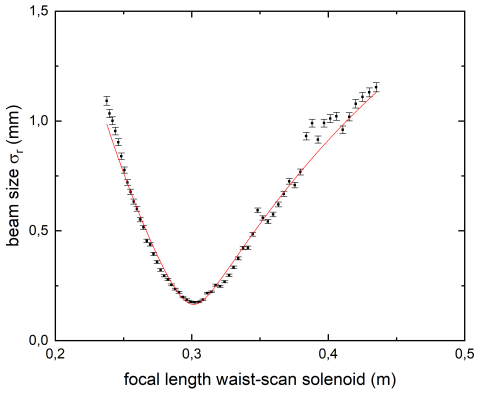

(c) Gun solenoid current 10.50 A

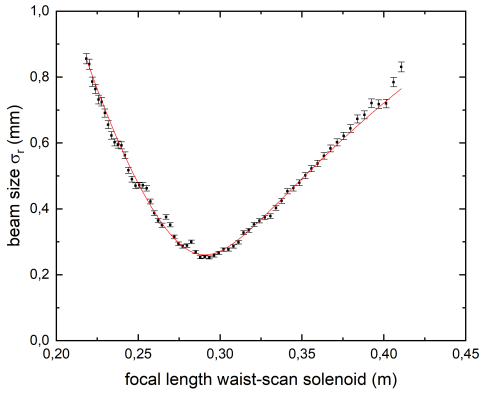

(d) Gun solenoid current 10.75 A

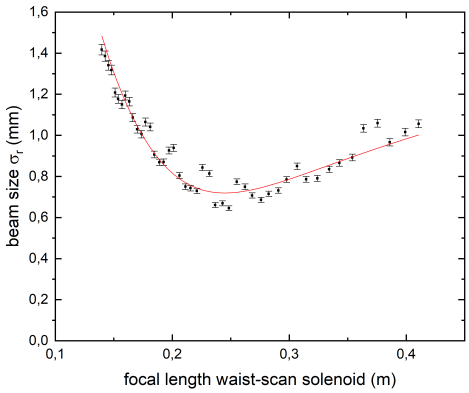

(e) Gun solenoid current 11.00 A

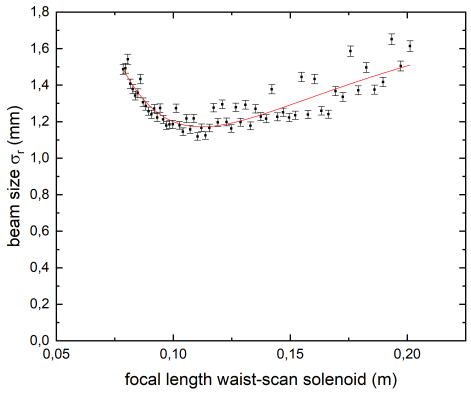

(f) Gun solenoid current 11.25 A

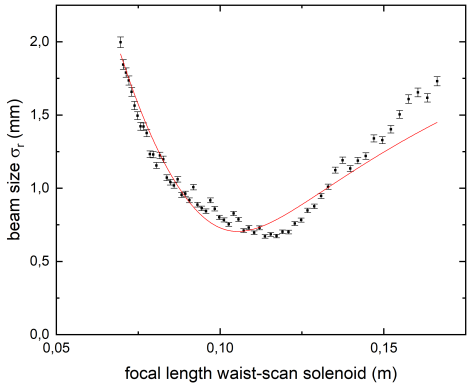

(g) Gun solenoid current 11.50 A

Figure 8.6: The data sets and corresponding fits of the individual waist scans performed on 15 pC ± 15% bunches and different gun solenoid currents. The beam size on the phosphor screen is plotted as a function of the focal length of the waist-scan solenoid and fitted with the waist-scan fit function. The bunches are created with a flat top UV laser beam profile on the cathode.

O Fits waist-scan series 30 pC ± 15% bunches

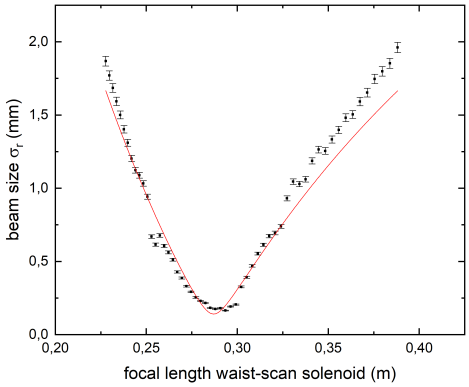

(a) Gun solenoid current 10.25 A

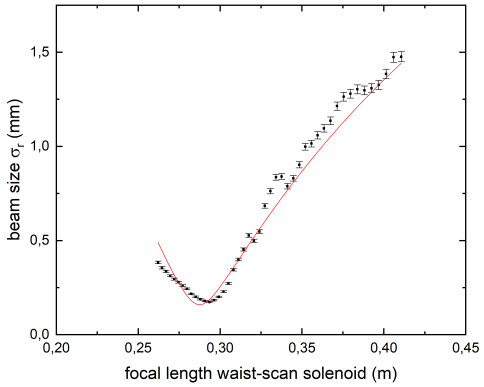

(b) Gun solenoid current 10.50 A

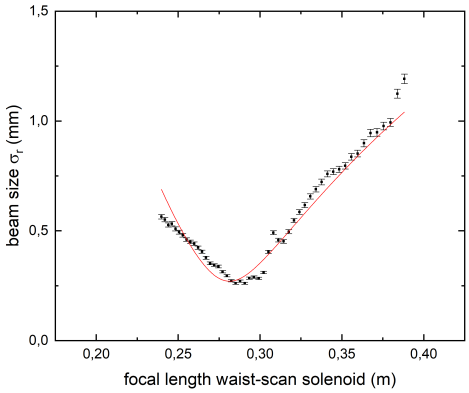

(c) Gun solenoid current 10.75 A

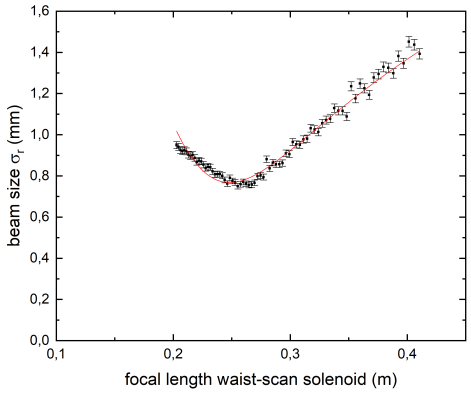

(d) Gun solenoid current 11.00 A

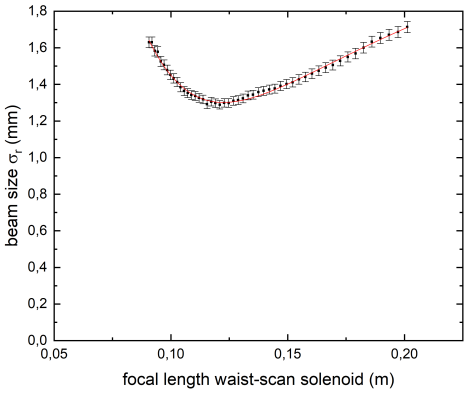

(e) Gun solenoid current 11.25 A

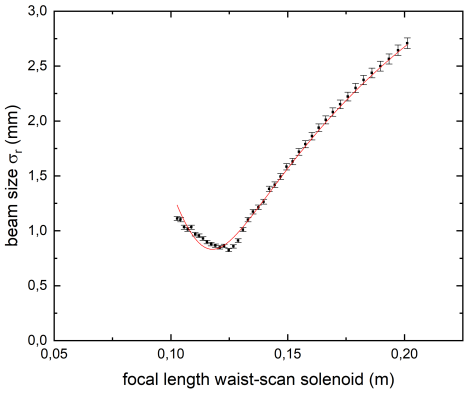

(f) Gun solenoid current 11.50 A

Figure 8.7: The data sets and corresponding fits of the individual waist scans performed on 30 pC ± 15% bunches and different gun solenoid currents. The beam size on the phosphor screen is plotted as a function of the focal length of the waist-scan solenoid and fitted with the waist-scan fit function. The bunches are created with a flat top UV laser beam profile on the cathode.

P Fits waist-scan series 47 pC ± 15% bunches

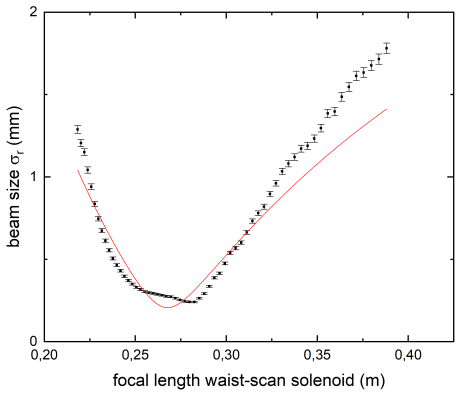

(a) Gun solenoid current 10.50 A

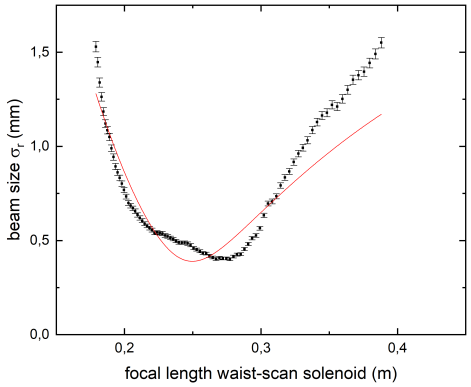

(b) Gun solenoid current 10.75 A

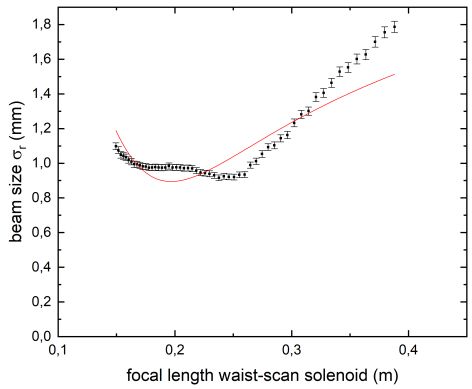

(c) Gun solenoid current 11.00 A

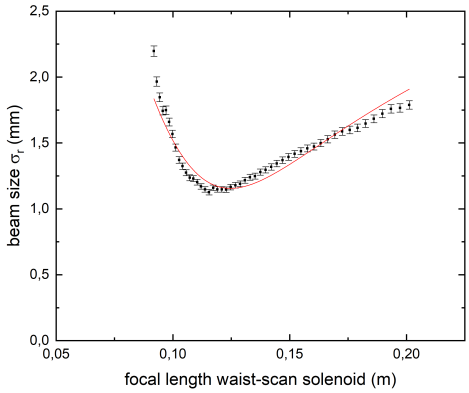

(d) Gun solenoid current 11.25 A

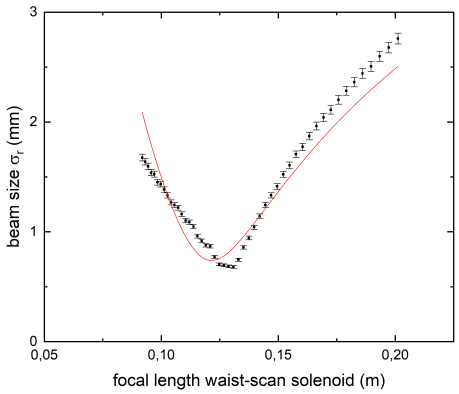

(e) Gun solenoid current 11.50 A

Figure 8.8: The data sets and corresponding fits of the individual waist scans performed on 47 pC ± 15% bunches and different gun solenoid currents. The beam size on the phosphor screen is plotted as a function of the focal length of the waist-scan solenoid and fitted with the waist-scan fit function. The bunches are created with a flat top UV laser beam profile on the cathode.